

Engineering Interfaces to Control Phase Transformations in Lithium-Based Battery Components

A Dissertation Presented to
The Academic Faculty

By

Francisco Javier Quintero Cortés

In Partial Fulfillment
of the Requirements for the Degree Doctor of Philosophy in
Materials Science and Engineering
School of Materials Science and Engineering

Georgia Institute of Technology

December, 2020

Copyright © Francisco Javier Quintero Cortés 2020

Engineering Interfaces to Control Phase Transformations in Lithium-based Battery Components

Approved by:

Dr. Matthew T. McDowell, Advisor
George W. Woodruff School of
Mechanical Engineering
School of Materials Science and
Engineering
Georgia Institute of Technology

Dr. Hamid Garmestani
School of Materials Science and
Engineering
Georgia Institute of Technology

Dr. Meilin Liu
School of Materials Science and
Engineering
Georgia Institute of Technology

Dr. Juan Pablo Correa-Baena
School of Materials Science and
Engineering
Georgia Institute of Technology

Dr. Hailong Chen
George W. Woodruff School of
Mechanical Engineering
Georgia Institute of Technology

Date Approved:
October 30th 2020

Este trabajo está dedicado a la gente de Páez, Cauca, Colombia.
La historia que nos une es lo que me trajo hasta aquí

ACKNOWLEDGMENTS

The first person I want to acknowledge is my fiancé, Pedro. Having him by my side made this journey the happiest time of my life.

More academically, I want to thank my advisor for giving me the opportunity to work with him and guide my learning throughout these years. Thanks to him I was exposed to concepts, techniques and places that were entirely new to me. I also want to acknowledge his open mind and support for all the initiatives I pursued outside the lab for the benefit of the Georgia Tech community.

I want to thank all my labmates, especially Dr. Neha Kondekar for being a mentor, a supporter, a role model, a scientifically critical voice, and a friend. Similarly, I want to highlight Dr. Matthew Boebinger for helping me navigate the world of batteries and the American culture and history, mainly thanks for introducing me to Cajun food. The work presented in this document includes extensive contributions from Jack, Jared, and Thomas, I thank them enormously for their help with experiments and discussions. Similarly, I would like to thank Dr. Diptarka Majumdar for the discussions and his insight into the bigger picture of the battery industry during the development of my last project.

Georgia Tech gave me the opportunity to have an impact outside the lab, and that was another journey on its own. I have to thank my teams: Cami, Paul and Paska for working with me at the Fulbright Student Association; Sang, Aroua and Hema for all the energy put into Grad Chats; Jo, Neha, Sonja and Dylan for the amazing work at Comm'on Tech. A big thank you to Narayan for giving me the position at the Student Government, and a huge thank you to Zifei and Jenna for all the effort put into the professional

development of our grad students. I also need to thank everyone who helped organize CRIDC 2020: Jo, Jana, Robbie, James, Zifei, Jenna. My thesis has been a lot of work, but organizing CRIDC was by far the most strenuous and memorable part of my PhD experience. Last in this list of engagements outside the lab, I want to thank Stephanie, Neha, Emily and Sang for the drive to create the yet-unnamed workshops around leadership in diversity that come to the research labs.

Connected to that experience outside the lab, I also had the chance to grow as a leader and a teacher through LEAD. I want to thank Stacey for introducing me to the world of coaching, giving me the chance to teach, and thanks for saying YES. One of those “yes” was the workshops around leadership in diversity for graduate students, so thanks for that.

More personally, thanks to my friends and family near and far for their support (in no particular order): Neha, Jo, Stephanie, Hamza, Pralav, Sang, Matthew, Cami, Natalia, Aby, Winston, Michelle, Laura, Aleja, Yami, Tats, Linita, Juan David, Thomas. Their constant support always brings me joy in the difficult days. Thanks to Uj and my mom for bringing me to where I am today and being my safety net. And dad, thanks for inspiring me, I miss you every day, but I know you are always here with me.

I want to thank the Fulbright program and Minciencias for bringing me to the US. The Fulbright experience made every interaction here deeper and more meaningful. Thanks to the Fulbright program, I met people from every continent and had the opportunity to learn from their cultures and their views of the world. Today I appreciate diversity more than ever before, and I have grown to thrive in it. I also want to thank the Colombian government for investing in people like me.

Finally, I want to thank the other institutions that provided the resources to support my PhD research: Novelis; the Advanced Photon Source, a U.S. Department of Energy (DOE) Office of Science User Facility operated for the DOE Office of Science by Argonne National Laboratory under Contract No. DE-AC02-06CH11357; the Institute of Materials

at the Georgia Institute of Technology; the National Science Foundation under Award No. DMR-1652471; the Institute for Electronics and Nanotechnology at Georgia Tech, a member of the National Nanotechnology Coordinated Infrastructure, which is supported by the National Science Foundation (grant ECCS-1542174)

TABLE OF CONTENTS

ACKNOWLEDGMENTS.....	vi
LIST OF TABLES.....	ix
LIST OF FIGURES.....	x
SUMMARY.....	xii
CHAPTER 1: INTRODUCTION.....	1
1.1: Solid Electrolytes.....	4
1.2: Alloying Anodes.....	7
1.3: Current Collectors.....	9
1.4: Layout of this Dissertation.....	10
1.5: References.....	11
CHAPTER 2: ENGINEERING THE SOLID ELECTROLYTE-LITHIUM INTERFACE.....	15
2.1: Introduction.....	15
2.2: Methods.....	17
2.3: Results and Discussion.....	21
2.4: Conclusions.....	34
2.5: References.....	35
CHAPTER 3: CURRENT CONSTRICTION AT THE SOLID ELECTROLYTE-LITHIUM INTERFACE.....	39
3.1: Introduction.....	39
3.2: Methods.....	42
3.3: Results and Discussion.....	49

3.4: Conclusions.....	60
3.5: References.....	61
CHAPTER 4: STRAIN EVOLUTION DUE TO A MOVING INTERFACE DURING	
LITHIATION OF ALLOYING ANODES.....	64
4.1: Introduction.....	64
4.2: Methods.....	66
4.3: Results and Discussion.....	70
4.4: Conclusions.....	82
4.5: References.....	84
CHAPTER 5: ENGINEERING INTERFACES OF CURRENT COLLECTORS	
5.1: Introduction.....	88
5.2: Methods.....	91
5.3: Results and Discussion.....	93
5.4: Conclusions.....	100
5.5: References.....	100
CHAPTER 6: CONCLUSIONS AND RECOMMENDATIONS.....	
APPENDIX.....	107
Python Code to Calculate Current Density Maps.....	107
VITA.....	110

LIST OF TABLES

Table 2.1. Performance benchmarks for protection layers in NASICON symmetric cells.....	22
Table 4.1. Full-width-half-maximum (FWHM) of the peaks shown in Figure 4.3.....	73

LIST OF FIGURES

Figure 1.1. Battery components and their contribution to thickness, weight and cost of the battery unit.....	2
Figure 2.1. Electrochemistry of symmetric cells with and without Cr protection layers...	21
Figure 2.2. Impedance spectra of LAGP with various deposited protection layers and Li on both sides before cycling.....	23
Figure 2.3. Comparison of the interphase morphology between bare and protected LAGP.....	25
Figure 2.4. Cr-protected LAGP cycled at 0.3 mA cm^{-2}	27
Figure 2.5. Evidence of plating and extended stability with dual-layer protection.....	28
Figure 2.6. Characterization of full cells with a LiFePO_4 cathode.....	31
Figure 2.7. Electrochemical behavior of half cells with liquid electrolytes with an LAGP composite slurry electrode as the working electrode.....	32
Figure 3.1. Schematic representation of the procedure used to segment the lithium electrodes.....	46
Figure 3.2. Schematic representation of the procedure used to segment interfacial void volume.....	47
Figure 3.3. Schematic representation of the procedure developed to create 2D contact area maps for an Li/LSPS interface.....	48
Figure 3.4. Operando X-ray imaging of symmetric cells.....	50
Figure 3.5. Relating interfacial contact area to cell electrochemistry.....	51
Figure 3.6. Validation of the current density model.....	55
Figure 3.7. Evolution of contact area and current density at the stripping interface.....	57
Figure 3.8. Current density line scans in different locations of the interface at various times.....	58
Figure 3.9. Statistical analysis of the calculated current density maps.....	59
Figure 4.1. Experimental setup.....	70
Figure 4.2. Evolution of the diffracted intensity from the (111) planes of a single Ge particle during lithiation.....	72

Figure 4.3. Diffraction peaks calculated by integrating over all separate 2D slices collected during a single rocking curve measurement.....	73
Figure 4.4. Changes in intensity and (111) planar spacing overlaid with electrochemistry.....	75
Figure 4.5. Integrated diffracted intensity and <i>d</i> -spacing from a non-reacting particle.....	77
Figure 4.6. Analytical model for stress and strain evolution within a crystalline Ge particle during electrochemical reaction.....	81
Figure 4.7. Evolution of <i>d</i> -spacing as a function of the extent of reaction for a single particle.....	82
Figure 5.1. Concentration profile measured by Neutron Depth Profiling of implanted Li on an Fe target.....	90
Figure 5.2. Performance of Fe protection layer on Al compared to Cu and bare Al.....	94
Figure 5.3. Scanning electron microscopy images of the sputtered Fe film.....	96
Figure 5.4. Flooded cell configuration and demonstration of long stability.....	98
Figure 5.5. Effect of epoxy on current density evolution.....	99

SUMMARY

Lithium-ion batteries are used in a broad range of applications from consumer electronics to electric vehicles. These applications are driving demand for increased battery capacity and improved safety. In this thesis, we investigate and engineer key battery components that can push battery performance to meet demand.

This thesis presents several strategies to increase the energy density of lithium-based batteries. The first strategy presented here is the use of lithium metal anodes. Lithium metal has the highest specific capacity of any anode material for lithium batteries, but its use in conventional batteries is associated with fire hazards due to its interaction with the liquid electrolyte. To overcome this challenge, we replace liquid electrolytes with solids. In the first part of this thesis, we use operando synchrotron X-ray imaging and analysis to study the interfacial phenomena between lithium metal and the solid electrolyte and uncover the role of protection layers, contact area and current constriction.

The second strategy presented in this thesis is the use of alloying anode materials, such as germanium or silicon, instead of lithium metal. These materials offer lower capacity but are deemed safer than lithium metal. Alloying materials, however, undergo phase transformations that induce large volume changes and fracture, limiting their stability. In the second part of this thesis, we present an operando synchrotron X-ray examination of a germanium alloying anode at the single particle level to reveal the evolution of strain and stress across a sharp interface during lithiation of the material.

Lastly, we present an engineering strategy to replace commercially-used current collectors with lighter and more cost-effective alternatives. This effort requires stabilizing the interface between new current collector materials and liquid electrolytes. Anode

current collectors in commercial batteries are made of copper and comprise around 10 % of the weight and cost of the battery while being an electrochemically inactive component. In the last part of this thesis, we develop new stabilized current collector materials resulting in improved energy density and reduced cost.

The work presented in this thesis highlights the importance of understanding and controlling interfaces in lithium-based batteries, and it also provides important insight that can guide the development of the next generation of safe, high-capacity batteries.

CHAPTER 1: INTRODUCTION

Lithium-ion batteries have enabled the widespread use of portable electronics over the past 30 years. Advances towards the next generation of lithium-based batteries will enable mass adoption of electric vehicles and lower the costs of solar energy. Leveraging these technologies is essential in meeting even the most modest goals in reduction of carbon dioxide emissions set in the Paris agreement.¹ Furthermore, affordable, high-capacity batteries can be a practical answer to provide energy autonomy to regions disconnected from the grid. In countries like Colombia, about 5 % of the population lives in remote areas with only limited access to electricity.² Robust energy storage systems can complement intermittent power sources like wind and sunlight power to enhance the quality of life in those areas.

Next-generation lithium-based batteries will have higher capacity and lower cost without sacrificing safety. These are three intertwined and sometimes conflicting attributes. For example, the highest capacity is achieved when using metallic lithium, which often leads to safety risks. Metallic lithium is extremely reactive and it can induce undesired phase transformations across the different battery components. Such transformations shorten the lifetime of batteries and are often linked to safety hazards, such as short-circuits and explosions.^{3–5} This highlights the importance of understanding and developing strategies to mitigate or control these phase transformations. These phase transformations with undesired consequences can occur practically on any battery component,^{6–9} hence the necessity to look at next-generation batteries holistically.

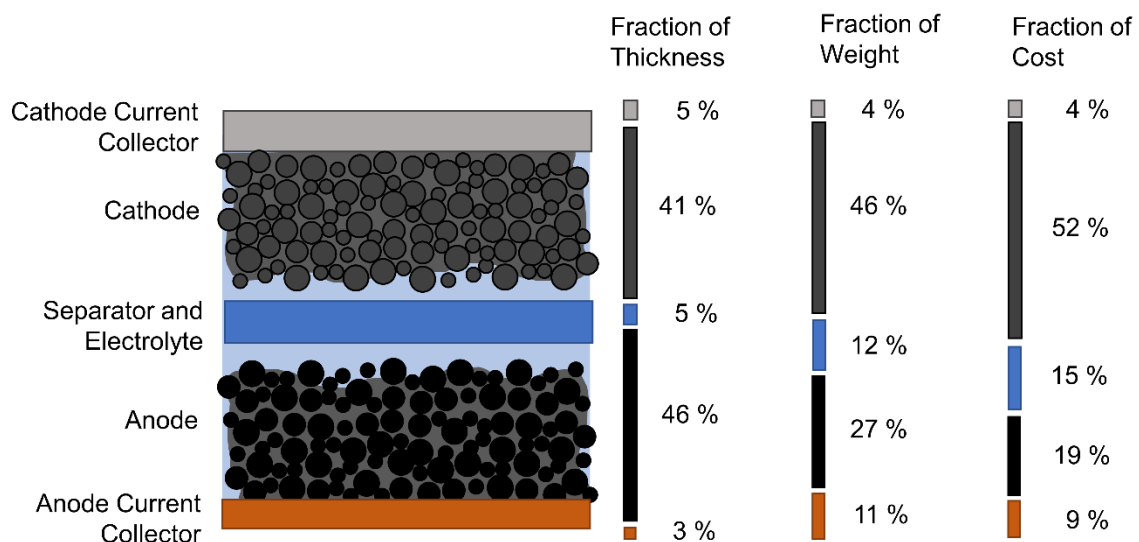


Figure 1.1. Battery components and their contribution to thickness, weight and cost of the battery unit. Typical values were used according to Nelson et al.¹¹

A typical lithium-ion battery has six components: a cathode, an anode, an electrolyte, a separator, and two current collectors. The cathode and the anode are the active components where electrons and lithium ions induce desired phase transformations. During charge, lithium ions are released from the cathode material, causing a phase transformation. At the same time, the anode incorporates those lithium ions with the accompanying phase transformation. The reverse reactions occur during discharge. Those lithium ions are transported from one electrode to the other through an electrolyte, which is embedded in a separator to prevent short-circuits. Lastly, electrons are transported from the electrodes to an external circuit using current collectors. Figure 1.1 illustrates the relative contributions of each component to thickness, weight and cost of a typical lithium-ion battery. In terms of thickness, which is directly related to volumetric energy density, the active materials make up about 90 % of the thickness of the cell, but drop to 70 % when it comes to weight and cost.^{10,11} This raw analysis suggests that engineering both active and inactive components, such as electrolytes and current collectors, can enhance battery performance.

The key to the success of lithium-ion batteries since their commercial introduction by Sony in 1991 is cycling stability. This stability is achieved by using active materials that can be reversibly lithiated and delithiated. The active materials used in batteries today are graphite on the anode side, and layered oxides on the cathode side.¹¹ The reason why they are so stable is that these materials have minimal mechanical changes during lithiation (<15 % volume change).^{12,13} Another important aspect of the stability of today's batteries is that the anode reacts with the electrolyte to form a protective, self-limiting layer at the surface of the anode particles.¹⁴ This protective film, the solid electrolyte interphase (SEI) prevents the continuous decomposition of the electrolyte.

Retaining cycling stability with higher-capacity battery materials is challenging. As a general rule, higher capacity means larger volume changes. Graphite, for example, has a capacity of 372 mAh/g. When it is lithiated, there is one lithium atom for every 6 carbon atoms, and the volume expansion is 13 %.¹⁵ On the other extreme there is lithium metal with a theoretical capacity of 3860 mAh/g and an infinite volume change upon plating/stripping. Alloying anode materials such as aluminum, germanium or silicon have intermediate theoretical capacities and volume expansions ranging from 90 % to 310 %.^{16,17} For these materials, the large volumetric changes occur along with stress and fracture, which severely hinders cycling stability.⁶ A deeper understanding and engineering of these phase transformations is necessary In order to realize stable high-capacity anodes.

Different anode materials have different engineering strategies, but also share similar challenges. Alloying anodes, such as silicon, have been widely studied. Today, important aspects of the reaction mechanisms are well understood. In the cases of crystalline silicon or germanium, these materials are known to undergo a two-phase reaction in which an expanded amorphous phase forms on the outside of a crystalline, unreacted core.^{18,19} The expansion of the outer phase causes large amounts of stress.²⁰

The strategies to mitigate the impact of that stress include controlling particle size and engineered nanostructures.^{21,22} These strategies cannot be directly translated to lithium metal. In the case of lithium metal, the main enemy is not fracture of the anode material, but dendritic plating and short-circuits.⁴ The engineering strategies on this front are engineered electrolytes (solid and liquid), and engineered current collectors.^{23–25} The challenges shared by alloying anodes as well as lithium metal anodes have to do with interfacial phase transformations. In the case of alloying anodes this is manifest in the form of stress and fracture of the active material, and in the case of lithium metal anodes, in the form of electrolyte decomposition, short-circuits, loss of contact, and fracture of the solid electrolyte.

The goals of this thesis are to understand and control interfacial phase transformations at the anode in next-generation lithium-based batteries. To understand these phase transformations, we used synchrotron X-ray techniques to probe the interfacial evolution of solid electrolytes in contact with lithium metal as well as the stress evolution in single-particle alloying anode materials. To control some of those interfacial reactions around the anode we used thin film protection layers. These protective layers were successfully implemented to extend the stability of solid electrolytes and current collectors. The work presented on this thesis advances the science and engineering of various material components of next-generation lithium-based batteries.

1.1: Solid Electrolytes

Conventional lithium-ion batteries use a liquid electrolyte composed of a lithium salt and an organic solvent to transport lithium ions from one electrode to the other. This liquid electrolyte has been engineered to be stable during battery operation and have high ionic conductivity, which in turn allows for high current densities during charge and

discharge.²⁶ The stability of the liquid electrolyte is largely due to the formation of a solid electrolyte interface (SEI) at the anode surface. This SEI is a product of the reduction of the liquid electrolyte due to the low chemical potentials at the anode. The composition and structure of the SEI is still a subject of active research and it has been shown to be a heterogeneous mixture of organic compounds and inorganic salts.¹⁴ In the case of graphite, although the SEI is highly stable, it can account for 50 % of capacity loss.¹⁴ In anode materials with more substantial volume changes upon lithiation and delithiation, the SEI is broken and regenerated at every cycle, leading to sustained capacity losses.²⁷

In the case of lithium metal anodes, liquid electrolytes present greater challenges. On the one hand, the infinite volume change due to plating and stripping of lithium can lead to more capacity losses when new lithium is exposed to the liquid electrolyte to form new SEI.²⁸ On the other hand, the properties of the SEI are also linked to the morphology of lithium plated.^{23,28} Non-uniform lithium plating/stripping leads to dead lithium (lithium deposits disconnected from the electrode) and dendrite formation.²⁹ Dendrites can grow long enough to short-circuit the battery and induce thermal runaway, which can cause fires and explosions.³⁰

Solid electrolytes are an alternative to circumvent the safety and efficiency challenges posed by liquid electrolytes and enable the use of lithium metal anodes. Solid electrolytes were thought to prevent short-circuits by mechanically blocking the passage of lithium dendrites.³¹ However, several types of solid electrolytes exhibit dendrite formation even at low current densities.^{32,33} The mechanisms for dendrite formation in solid electrolytes are still not well understood. Current density concentrations and high electrical conductivity of the solid electrolyte are common among the proposed mechanisms.^{32,34} Beyond short-circuits, solid electrolytes present other challenges related to phase transformations at the interface with the lithium metal anode.

A practical way to categorize solid electrolytes is by their (electro)chemical stability versus lithium metal. Following this classification, a solid electrolyte can: 1) be thermodynamically stable versus lithium and not form secondary phases; 2) react with lithium to form a self-limiting secondary phase; or 3) react with lithium to form a secondary phase that grows continuously.³⁵ There are no solid electrolytes that fall under the first category due to the high reactivity and low chemical potential of lithium metal. Solid electrolytes that fall under the second category have been shown to enable the growth of lithium dendrites even at moderate current densities.^{32–34} The reason why the secondary phase (or interphase) is self limiting is because it is ionically conductive and electrically insulating, blocking the flow of electrons to further reduce the solid electrolyte. This interphase is analogous to the SEI in liquid electrolytes. Solid electrolytes in the third category form an interphase that is both ionically and electronically conductive, causing the phase transformation to progress and consume the bulk of the solid electrolyte.³⁶ The interphase can have lower ionic conductivity than the solid electrolyte and increase the impedance of the cell and also induce fracture due to volume changes.³⁷

Mitigating or preventing the undesired phase transformations in unstable solid electrolytes broadens the selection of low cost solid electrolytes for lithium metal batteries. A prominent strategy is the use of artificial protection layers. These protection layers have been used to improve contact between lithium and the solid electrolyte as well as to block the reduction of the solid electrolyte.³⁸ Key attributes of common protection layers reported in the literature is that they need to be inert versus lithium, good ionic conductors and block electron transport: the same attributes of an ideal solid electrolyte.³⁸ This approach has led to moderate success in unstable solid electrolyte systems, but has not solved the problem yet, as discussed in detail in chapter 2. In that chapter, we present a substantially different approach. Instead of using an electronic insulator or an alloying material to improve lithium contact, we use an inert metal, Cr, with the goal of controlling the growth

trajectory of the interphase, instead of preventing its formation altogether. Using this mitigation strategy, we extended the cycling stability of a solid electrolyte by a factor of 8 in full cells.

Controlling these phase transformations in unstable solid electrolytes requires a deeper understanding of the dynamics of the interface between lithium and the solid electrolyte. With that goal, we used synchrotron X-ray tomography to image symmetric cells (lithium-solid electrolyte-lithium) *in operando*. Our experiments revealed the progressive growth of interphase instead of lithium plating as well as a correlation between contact area and cell voltage. Chapter 3 deals with this matter in thorough detail and also presents a semi-quantitative model that reveals the impacts of current constriction on the distribution of local current densities. Our findings indicate that when contact becomes more ‘spotty’ and the net contact area is reduced, the local current densities increase dramatically along with the observed cell voltage. Since loss of contact is common across all types of solid electrolytes, this conclusion can guide strategies to prevent failure of stable and unstable solid electrolytes.

1.2: Alloying Anodes

While lithium metal anodes have the highest theoretical capacity of any anode material for lithium batteries, alloying anodes offer high capacities and lower inherent risks. Alloying anode materials such as germanium or silicon have theoretical capacities 5 - 10 times higher than graphite electrodes.^{6,19} These alloying materials react with lithium to form lithium-rich phases such as $\text{Li}_{15}\text{Ge}_4$ or $\text{Li}_{15}\text{Si}_4$ at electrode potentials that are close to but higher than the potential for lithium plating.²⁰ This means that the difficulties associated with lithium plating and stripping are removed, and that solid electrolytes that decompose at lithium potentials could be stable against alloying anode materials.

The high capacity of germanium or silicon come at the penalty of a large volume expansion. In the case of silicon, for example, the volume change is about 310 % upon lithiation.¹⁶ Besides the large volume change, the reaction mechanism involves a two-phase reaction with an atomically sharp interface between an amorphous lithiated phase, and the pristine crystal.²⁰ The difference in properties at the interface causes additional strain to the reacting material and leads to fracture.^{7,20} When fracture occurs, the freshly exposed anode material can react with the surrounding liquid electrolyte to form SEI or get disconnected and become inactive. This occurs at every cycle, causing rapid capacity fade.²²

Many aspects of the lithiation mechanisms of alloying anode materials are well understood. The trajectory of phase changes is well documented: the pristine crystal gradually transforms into amorphous Li_xGe (or Li_xSi) and Ge and crystallizes into $\text{Li}_{15}\text{Ge}_4$ towards the end of the lithiation process.³⁹ Electron and X-ray microscopy have revealed the morphology, reaction mechanism and fracture of single particles;^{19,40} and ensemble X-ray and Raman measurements have been used to quantify average strain evolution during lithiation.^{39,41} All of these elements are necessary in order to engineer electrode architectures that can mitigate the negative impacts of the large volume expansion of alloying anodes. An important piece that was missing was the strain evolution at the single particle level. In chapter 4 of this thesis, we present a synchrotron X-ray investigation on single-particle germanium anodes. The technique used was *operando* Bragg coherent diffraction, which enabled us to track the crystalline unreacted core of individual germanium particles in reciprocal space and measure small changes in lattice spacing during reaction. These observations provide a fundamental understanding of a moving two-phase interface that sweeps across a particle during electrochemical reaction, and will facilitate the engineering of electro-chemo-mechanically robust alloying anodes.

1.3: Current Collectors

The technological relevance of using high capacity anodes such as lithium metal or alloying materials is that they can bring significant improvements in energy density. The volumetric energy density gain from combining solid electrolytes and lithium metal can be as high as 58 % and 30 % for silicon-based alloying anodes.¹⁰ However, other inactive components of the battery can also be optimized to obtain higher energy density. As shown in Figure 1.1, inactive components such as the current collectors can be as much as 15 % of the weight and cost of a battery, and about two thirds of this weight and cost come from the anode current collector alone. This suggests that engineering the anode current collector can significantly impact the overall energy density of next-generation batteries.

Anode current collectors are made of copper owing to its electrochemical stability, electrical conductivity and cost. Other materials that are electrochemically stable at the low potentials of lithiated anodes include iron, stainless steel, nickel and chromium.^{42,43} A common characteristic shared across these materials is that they do not react with lithium at room temperature to form alloys, which makes them thermodynamically stable at low electrochemical potentials. This is in contrast to lighter metals such as aluminum, which is used as the cathode current collector, that readily alloy with lithium.^{8,17} Replacing copper with lighter and less costly metals would improve the energy density and cost of commercial lithium-ion batteries as well as next-generation lithium batteries. However, the choice of anode current collector materials is limited by their electrochemical stability at low potentials.

The challenge of extending the stability of materials in the vicinity of the anode is at the core of this thesis. The previous experience using interfacial protection layers for solid electrolytes suggests that it is possible to increase the stability of materials in contact

with lithium. In chapter 4, we use an interfacial protection layer to extend the stability of aluminum anode current collectors. In contrast to the case of solid electrolytes, where ionic conduction was necessary, the interlayer to protect the current collector needs to block lithium conduction and only allow electrons to flow. We found that a sub-micron protective film is sufficient to prevent the electrochemical reaction of aluminum at very low potentials for hundreds of hours. Implementing this strategy, it will be possible to increase the overall gravimetric energy density of commercial Li-ion batteries by up to 6 % from the current collector alone.

1.4: Layout of this Dissertation

The body of this document is split into 4 chapters, the first two focused on solid electrolytes, the next one on alloying anodes and the last one on current collectors. The logic behind this arrangement is to first introduce the work on the most sought-after battery technology, lithium metal anodes, then go in decreasing order of projected gains in energy density. At the same time, chapter by chapter, we present different aspects of battery technologies that are closer and closer to real-life implementation. Chapter 2 deals with a strategy to extend the interfacial stability of a solid electrolyte that is electrochemically unstable in contact with metallic lithium. In Chapter 3, we dive deeper into the understanding of interfacial phenomena at the boundary between lithium and solid electrolytes using synchrotron X-ray tomography. After this, alloying anodes are presented as an alternative to lithium metal anodes which is closer to widespread use. In Chapter 4, we use synchrotron X-ray diffraction to probe the strain evolution in an alloying anode at the single particle level. The last chapter before the conclusions and recommendations presents the technology developed in this thesis that is closest to commercial implementation in lithium-based batteries. Chapter 5 presents a protective layer that

enables the use of aluminum current collectors as a cheaper and lighter alternative to the incumbent technology.

1.5: References

1. Teske, S. *Achieving the Paris Climate Agreement Goals: Global and Regional 100% Renewable Energy Scenarios with Non-energy GHG Pathways for +1.5°C and +2°C*. (Springer, 2019).
2. Superintendencia Delegada para Energía y Gas Combustible. *Zonas No Interconectadas -ZNI Diagnóstico de la prestación del servicio de energía eléctrica 2017*.
<https://www.superservicios.gov.co/sites/default/archivos/SSPD%20Publicaciones/Publicaciones/2018/Sep/diagnosticozni-superservicios-oct-2017.pdf> (2017).
3. Wang, S., Rafiz, K., Liu, J., Jin, Y. & Lin, J. Y. S. Effects of lithium dendrites on thermal runaway and gassing of LiFePO₄ batteries. *Sustainable Energy & Fuels* vol. 4 2342–2351 (2020).
4. Cheng, X.-B., Zhang, R., Zhao, C.-Z. & Zhang, Q. Toward Safe Lithium Metal Anode in Rechargeable Batteries: A Review. *Chemical Reviews* vol. 117 10403–10473 (2017).
5. Chung, H. & Kang, B. Mechanical and Thermal Failure Induced by Contact between a Li 1.5 Al 0.5 Ge 1.5 (PO₄)₃ Solid Electrolyte and Li Metal in an All Solid-State Li Cell. (2017) doi:10.1021/acs.chemmater.7b02301.
6. Li, H. *et al.* Circumventing huge volume strain in alloy anodes of lithium batteries. *Nat. Commun.* **11**, 1584 (2020).
7. Zuo, X., Zhu, J., Müller-Buschbaum, P. & Cheng, Y.-J. Silicon based lithium-ion battery anodes: A chronicle perspective review. *Nano Energy* vol. 31 113–143 (2017).
8. Ma, T. *et al.* Revisiting the Corrosion of the Aluminum Current Collector in Lithium-Ion Batteries. *J. Phys. Chem. Lett.* **8**, 1072–1077 (2017).
9. Wenzel, S. *et al.* Direct Observation of the Interfacial Instability of the Fast Ionic Conductor Li₁₀GeP₂S₁₂ at the Lithium Metal Anode. *Chemistry of Materials* vol. 28 2400–2407 (2016).
10. Placke, T., Kloeppsch, R., Dühnen, S. & Winter, M. Lithium ion, lithium metal, and alternative rechargeable battery technologies: the odyssey for high energy density. *Journal of Solid State Electrochemistry* vol. 21 1939–1964 (2017).
11. Nelson, P. A., Ahmed, S., Gallagher, K. G. & Dees, D. W. Modeling the Performance and Cost of Lithium-Ion Batteries for Electric-Drive Vehicles, Third Edition. (2019) doi:10.2172/1503280.
12. Asenbauer, J. *et al.* The success story of graphite as a lithium-ion anode material –

- fundamentals, remaining challenges, and recent developments including silicon (oxide) composites. *Sustainable Energy & Fuels* (2020) doi:10.1039/d0se00175a.
13. Wang, X., Xiao, R., Li, H. & Chen, L. Quantitative structure-property relationship study of cathode volume changes in lithium ion batteries using ab-initio and partial least squares analysis. *Journal of Materiomics* **3**, 178–183 (2017).
 14. Wang, A., Kadam, S., Li, H., Shi, S. & Qi, Y. Review on modeling of the anode solid electrolyte interphase (SEI) for lithium-ion batteries. *npj Computational Materials* vol. 4 (2018).
 15. Schweidler, S. *et al.* Volume Changes of Graphite Anodes Revisited: A Combined Operando X-ray Diffraction and In Situ Pressure Analysis Study. (2018) doi:10.1021/acs.jpcc.8b01873.
 16. Beaulieu, L. Y., Eberman, K. W., Turner, R. L., Krause, L. J. & Dahn, J. R. Colossal Reversible Volume Changes in Lithium Alloys. *Electrochemical and Solid-State Letters* vol. 4 A137 (2001).
 17. Qin, B. *et al.* Revisiting the Electrochemical Lithiation Mechanism of Aluminum and the Role of Li-rich Phases (Li Al) on Capacity Fading. *ChemSusChem* **12**, 2609–2619 (2019).
 18. Liu, X. H. *et al.* In situ atomic-scale imaging of electrochemical lithiation in silicon. *Nat. Nanotechnol.* **7**, 749–756 (2012).
 19. Liu, X. H. *et al.* Reversible nanopore formation in Ge nanowires during lithiation-delithiation cycling: an in situ transmission electron microscopy study. *Nano Lett.* **11**, 3991–3997 (2011).
 20. McDowell, M. T. *et al.* Studying the kinetics of crystalline silicon nanoparticle lithiation with in situ transmission electron microscopy. *Adv. Mater.* **24**, 6034–6041 (2012).
 21. Xia, X., Di Leo, C. V., Gu, X. W. & Greer, J. R. In Situ Lithiation–Delithiation of Mechanically Robust Cu–Si Core–Shell Nanolattices in a Scanning Electron Microscope. (2016) doi:10.1021/acsenergylett.6b00256.
 22. Wang, H. *et al.* A binder-free high silicon content flexible anode for Li-ion batteries. *Energy & Environmental Science* vol. 13 848–858 (2020).
 23. Thenuwara, A. C. *et al.* Efficient Low-Temperature Cycling of Lithium Metal Anodes by Tailoring the Solid-Electrolyte Interphase. *ACS Energy Letters* vol. 5 2411–2420 (2020).
 24. Lee, Y.-G. *et al.* High-energy long-cycling all-solid-state lithium metal batteries enabled by silver–carbon composite anodes. *Nature Energy* vol. 5 299–308 (2020).
 25. Fan, H., Dong, Q., Gao, C., Hong, B. & Lai, Y. Powder-sintering derived 3D porous current collector for stable lithium metal anode. *Mater. Lett.* **234**, 69–73 (2019).
 26. Xu, K. Nonaqueous liquid electrolytes for lithium-based rechargeable batteries. *Chem. Rev.* **104**, 4303–4417 (2004).
 27. Michan, A. L. *et al.* Solid Electrolyte Interphase Growth and Capacity Loss in Silicon

- Electrodes. *J. Am. Chem. Soc.* **138**, 7918–7931 (2016).
28. Bieker, G., Winter, M. & Bieker, P. Electrochemical in situ investigations of SEI and dendrite formation on the lithium metal anode. *Phys. Chem. Chem. Phys.* **17**, 8670–8679 (2015).
 29. Chen, K.-H. *et al.* Dead lithium: mass transport effects on voltage, capacity, and failure of lithium metal anodes. *Journal of Materials Chemistry A* vol. 5 11671–11681 (2017).
 30. Li, Y. *et al.* Thermal Runaway Triggered by Plated Lithium on the Anode after Fast Charging. *ACS Appl. Mater. Interfaces* **11**, 46839–46850 (2019).
 31. Monroe, C. & Newman, J. The Impact of Elastic Deformation on Deposition Kinetics at Lithium/Polymer Interfaces. *J. Electrochem. Soc.* **152**, A396 (2005).
 32. Kasemchainan, J. *et al.* Critical stripping current leads to dendrite formation on plating in lithium anode solid electrolyte cells. *Nat. Mater.* **18**, 1105–1111 (2019).
 33. Ren, Y., Shen, Y., Lin, Y. & Nan, C.-W. Direct observation of lithium dendrites inside garnet-type lithium-ion solid electrolyte. *Electrochem. commun.* **57**, 27–30 (2015).
 34. Han, F. *et al.* High electronic conductivity as the origin of lithium dendrite formation within solid electrolytes. *Nature Energy* vol. 4 187–196 (2019).
 35. Wenzel, S., Leichtweiss, T., Krüger, D., Sann, J. & Janek, J. Interphase formation on lithium solid electrolytes—An in situ approach to study interfacial reactions by photoelectron spectroscopy. *Solid State Ionics* **278**, 98–105 (2015).
 36. Zhu, Y., He, X. & Mo, Y. Origin of Outstanding Stability in the Lithium Solid Electrolyte Materials: Insights from Thermodynamic Analyses Based on First-Principles Calculations. *ACS Appl. Mater. Interfaces* **7**, 23685–23693 (2015).
 37. Lewis, J. A. *et al.* Interphase Morphology between a Solid-State Electrolyte and Lithium Controls Cell Failure. *ACS Energy Letters* vol. 4 591–599 (2019).
 38. Sun, C. *et al.* Recent advances in anodic interface engineering for solid-state lithium-metal batteries. *Mater. Horiz.* **7**, 1667–1696 (2020).
 39. Pharr, M., Choi, Y. S., Lee, D., Oh, K. H. & Vlassak, J. J. Measurements of stress and fracture in germanium electrodes of lithium-ion batteries during electrochemical lithiation and delithiation. *J. Power Sources* **304**, 164–169 (2016).
 40. Lee, S. W., Ryu, I., Nix, W. D. & Cui, Y. Fracture of crystalline germanium during electrochemical lithium insertion. *Extreme Mechanics Letters* **2**, 15–19 (2015).
 41. Zeng, Z. *et al.* In situ measurement of lithiation-induced stress in silicon nanoparticles using micro-Raman spectroscopy. *Nano Energy* **22**, 105–110 (2016).
 42. Myung, S.-T., Sasaki, Y., Sakurada, S., Sun, Y.-K. & Yashiro, H. Electrochemical behavior of current collectors for lithium batteries in non-aqueous alkyl carbonate solution and surface analysis by ToF-SIMS. *Electrochim. Acta* **55**, 288–297 (2009).

43. Iwakura, C. *et al.* Electrochemical characterization of various metal foils as a current collector of positive electrode for rechargeable lithium batteries. *J. Power Sources* **68**, 301–303 (1997).

CHAPTER 2: ENGINEERING THE SOLID ELECTROLYTE-LITHIUM INTERFACE*

2.1: Introduction

Solid state batteries (SSBs) are a promising alternative to conventional liquid-electrolyte-based cells for enabling high-capacity Li metal anodes, which have long carried safety risks when used in liquid electrolytes.^{1,2} Replacing liquids with solid-state electrolytes (SSEs) reduces the risk of thermal runaway and may inhibit Li filamentary growth³, which could enable the use of Li metal anodes. Significant progress has been made in developing SSE materials with ionic conductivity $>0.1 \text{ mS cm}^{-1}$,⁴⁻⁹ which is comparable to liquid electrolytes. However, most SSEs are thermodynamically unstable in contact with lithium metal, and they react to form new phases (an interphase) when in contact with Li.¹⁰⁻¹² In some cases, the growth of the interphase is kinetically limited and thus passivates the interface, which can result in relatively stable cycling.¹³⁻¹⁵ In many SSEs with high ionic conductivity, such as some sodium super-ionic conductors (NASICON) and various sulfide Li-SSEs, the interphase is instead a mixed ionic-electronic conductor (MIEC).^{16,17} MIEC interphases can grow continuously during cycling since both electrons and ions can be transported to react with the underlying SSE. The growth of

* © The Electrochemical Society, Inc. 2019. All rights reserved. Except as provided under U.S. copyright law, this work may not be reproduced, resold, distributed, or modified without the express permission of The Electrochemical Society (ECS). The archival version of this work was published as Francisco Javier Quintero Cortes, John A. Lewis, Jared Tippens, Thomas S. Marchese and Matthew T. McDowell. "How Metallic Protection Layers Extend the Lifetime of NASICON-Based Solid-State Lithium Batteries". Journal of The Electrochemical Society, Volume 167, Number 5. <https://doi.org/10.1149/2.0032005JES>

such interphases can cause fracture of the SSE, severely limiting operational current densities and cycle life for batteries with this type of SSE.^{18–20}

NASICONs are attractive materials for SSBs despite the challenges they present. In contrast to sulfides and garnets, NASICONs such as $\text{Li}_{1+x}\text{Al}_x\text{Ge}_{2-x}(\text{PO}_4)_3$ (LAGP) and $\text{Li}_{1+x}\text{Al}_x\text{Ti}_{2-x}(\text{PO}_4)_3$ (LATP) are stable in ambient air and even in water.^{21,22} As a consequence, processing is significantly simpler and more battery chemistries are enabled, such as Li-air batteries.²³ However, the interfacial reaction between some NASICON SSEs and Li generates a large volume expansion which causes mechanical degradation.^{18,24} In the case of LAGP, it has been shown that the pristine material is continuously reduced, forming an amorphous interphase¹⁸ containing metallic germanium.¹⁶ The morphology of the interphase has been observed to play a key role in chemo-mechanical degradation and cell failure. At higher current densities ($>\sim 0.5 \text{ mA cm}^{-2}$), the interphase tends to grow with a filamentary morphology instead of the planar morphology found at lower current densities ($\sim 0.1 \text{ mA cm}^{-2}$), and fracture and failure are accelerated.¹⁸ Using in situ x-ray tomography, we have shown that it is the mechanical degradation of LAGP that is responsible for cell failure due to increased impedance, rather than the impedance of the growing interphase itself.¹⁹ With these recent findings in mind, it is clear that preventing or controlling the reaction process at the Li/SSE interface is critical for further development of these materials for Li metal SSBs.

The guiding principle to extend cycle life of unstable SSEs, including NASICON materials, is to prevent direct contact between Li and the SSE. This principle has led to the investigation of thin protection layers on SSEs,^{25–31} layering of different SSEs,^{32–34} and embedding the SSE into polymeric matrices.^{35,36} These approaches have resulted in varying degrees of improvement in stability. In principle, the protective layer between Li metal and the SSE should enable ion transport but prevent electron transport to impede the electrochemical reduction of the SSE.^{37,38} Surprisingly, electronically-conducting

protective layer materials, such as Ge²⁹ and Al,³⁰ have recently been shown to significantly increase cycle life at moderate current densities (0.1 - 0.3 mA cm⁻²) at room temperature. Despite this improved performance, there has been no comprehensive investigation of the underlying mechanisms by which these electronically-conducting protection layers improve stability.

Here, we demonstrate that thin Cr protection layers between Li and LAGP extend stable cycling times by more than an order of magnitude (from ~30 h to >1000 h), and we also show that this improved stability is due to altered morphological growth trajectories of the interphase instead of complete prevention of interphase growth. We attribute the observed uniform growth of the interphase region and improved chemo-mechanical stability of the interphase region to the ability of the vapor-deposited Cr films to mitigate non-uniformities in ion transport near the interface, which can cause irregular growth and cell failure. A variety of electrochemical techniques, in conjunction with x-ray photoelectron spectroscopy (XPS) and scanning electron microscopy (SEM), support these conclusions. Beyond demonstrating unprecedented electrochemical stability for the Li/LAGP interface, these results indicate that stable performance may be attained through interface engineering specifically designed to control interphase formation in a variety of unstable materials.

2.2: Methods

Synthesis: LAGP was synthesized following a procedure similar to that in our previously reported work.¹⁸ 0.8 M germanium ethoxide (Alfa Aesar, 99.995 %) and 0.2 M citric acid (Sigma-Aldrich, 99.5 %) were mixed in deionized water at 80 °C. After 20 h of stirring, stoichiometric amounts of lithium nitrate (Alfa Aesar, 99 %), aluminum nitrate nonahydrate (Alfa Aesar, 98 %) and ammonium phosphate (Sigma-Aldrich, 98 %) were

added to the solution. After 30 min, ethylene glycol (Sigma-Aldrich, 99 %) was added to the solution in a 1:1 molar ratio with citric acid (Sigma-Aldrich, 99 %). Then, the temperature was sequentially raised to 120 °C and 150 °C and held for 30 min at each temperature. The mixture was then held at 170 °C until dry. After drying, the powder was calcined and annealed in a tube furnace in ambient air at 500 °C for 4 h and then 800 °C for 5 h. The annealed powder was ball-milled and re-heated to 500 °C for 4 h in order to burn off residue from the ball milling. The burnt-off powder was then ground using a mortar and pestle and uniaxially pressed into pellets. The pellets were sintered in air at 900 °C for 6 h with a heating rate of 2 °C min⁻¹. The pellets were polished using hexylene glycol (Allied) as a lubricant and diamond paper (Thorlabs) with grit sizes of 30 µm, 6 µm, 3 µm and 1 µm. After polishing, the pellets were heat treated at 675 °C for 3 h with a heating rate of 2 °C min⁻¹.

Protection layers: Thin films of Cr were sputtered using a Unifilm Sputtering system. DC magnetron sputtering was performed under argon at a current of 0.045 A and a voltage of 98 V (approximate power of 4.41 W) using a 3-in Cr target (Kurt Lesker, 99.95 %). The base pressure was below 8x10⁻⁶ Torr and the process pressure was 5x10⁻³ Torr. The deposition rate was fixed at 0.1 nm min⁻¹ and the final thickness was typically 30 nm, although 5 nm and 60 nm were also used.

A custom-built ALD system was used to deposit thin films of Al₂O₃. Trimethyl aluminum (Sigma-Aldrich, 97 %) and DI water were used as precursors, and nitrogen was used as the carrier gas. The process temperature was 150 °C, the process pressure was 0.33 Torr, and the base pressure was below 0.06 Torr. The carrier gas flow rate was 20 sccm and the open and closed valve times for both precursors were 20 ms and 25 s, respectively. These conditions ensured a deposition rate of 1 Å per cycle. All depositions studied were run for 60 cycles.

Symmetric cells: Bare and Cr-protected Li/LAGP/Li symmetric cells were fabricated using pellets that had been polished on both sides. In an argon-filled glove box, lithium disks (Sigma-Aldrich, 99.9 %) with area of 0.486 cm^2 were cleaned and pressed on either side of the pellets. 2032 coin cells were assembled following this stack sequence: conducting foam, steel spacer, pellet with pressed lithium on both sides, steel spacer. The coin cells were pressed at 500 psi using a crimper. All symmetric cells were conditioned by cycling at 0.1 mA cm^{-2} for 5 min in each direction over 16 h. Electrochemical impedance spectra were collected in the range from 3 MHz to 2 Hz before and at different times during cycling using a Bio-Logic SP-200 potentiostat. Galvanostatic cycling (and conditioning) was completed using a Bio-Logic VMP3 potentiostat at room temperature.

Open-top cells: Open-top cells were fabricated as shown in Figure 4.4a. Pellets polished on both sides and coated with 30 nm Cr or 30 nm Cr on 6 nm Al_2O_3 were used for open-top cells. Only one side of the pellet was initially in contact with a lithium disk of 0.486 cm^2 area, and the other side was open to the argon atmosphere in the glove box. A discharge current density of 0.1 mA cm^{-2} was applied for 50 min using a Bio-Logic VMP3 potentiostat at room temperature.

Full cells: Bare and Cr-protected Li/LAGP/LFP full cells were fabricated using pellets that had been polished on one side. The solid-state LiFePO_4 (LFP, MTI Corp.) cathode was made from an acetonitrile (Sigma-Aldrich, 99.8 %) slurry containing LFP, polyethylene oxide (PEO, 5 million M.W., Sigma-Aldrich), LiTFSI (Sigma-Aldrich, 99.95 %), and Super P carbon powder (MTI). PEO and LiTFSI were dissolved in acetonitrile in an 8:1 molar ratio before mixing with the other components. The composition of the slurry was 20 wt.% PEO-LiTFSI, 10 wt.% Super P carbon powder, and 70 wt.% LFP. The slurry was drop-cast onto the unpolished side of the LAGP pellet in the glove box, and a lithium disk was pressed onto the polished (bare or protected) side of the pellet. The full cells

were galvanostatically cycled at a temperature of 60 °C with voltage limits of 2.5 V and 4.0 V.

LAGP as electrode: Half-cells with LAGP as the working electrode containing a liquid electrolyte were fabricated to study the electrochemistry of LAGP. LAGP slurries were made by mixing unsintered LAGP (70 wt. %), Super P carbon powder (20 wt. %), and PVDF-HFP (Kynar Flex) (10 wt.%) in N-Methyl-2-Pyrrolidone (Sigma-Aldrich, 99.5 %). The slurries were drop-cast on a copper foil and evenly spread using a doctor blade. Half-cells were made in 2032 coin cells using metallic lithium as the counter/reference electrode and 1.0 M LiPF₆ in 1:1 ethylene carbonate:diethyl carbonate (Sigma-Aldrich, battery grade) as the electrolyte. The cells were pressed and sealed inside an argon-filled glove box. Cyclic voltammetry (CV) and galvanostatic cycling were performed on these cells using a Bio-Logic VMP3 potentiostat at room temperature.

Characterization: Symmetric and full cells were studied ex situ using scanning electron microscopy (SEM). Cross-sectional SEM images were obtained by breaking the LAGP pellet after cycling (whenever Cr was used) or by using the pieces from fractured pellets if fracture occurred during electrochemical cycling (this was common for bare LAGP). The samples were exposed to air for less than 20 s to transfer them into the SEM. Given the significant changes in morphology due to interphase growth (on the order of tens of microns), we do not expect the short air exposure to affect the interpretation of the SEM data. The instrument used was a Zeiss Ultra60 FE-SEM with an accelerating voltage of 5 or 10 kV.

The open-top cells were analyzed using X-ray photoelectron spectroscopy (XPS) to determine the presence of lithium on the surface of the pellets. XPS was performed using a Thermo Scientific K-Alpha system with a monochromatic Al K α source. The spot size was 400 μ m in diameter and the X-ray gun power was 15 W. The analyzer was set with a dwell time of 100 ms and a pass energy of 50 eV with a resolution of 0.05 eV. The

surface of the sample was flooded with slow electrons and Ar^+ ions using the flood gun to compensate for surface charging. The base pressure was 4.5×10^{-8} Torr, and it never exceeded 1.8×10^{-7} Torr during analysis. All the samples were transferred from the glove box to the XPS chamber using a vacuum transfer holder that kept the sample sealed without exposure to air during the transfer.

2.3: Results and Discussion

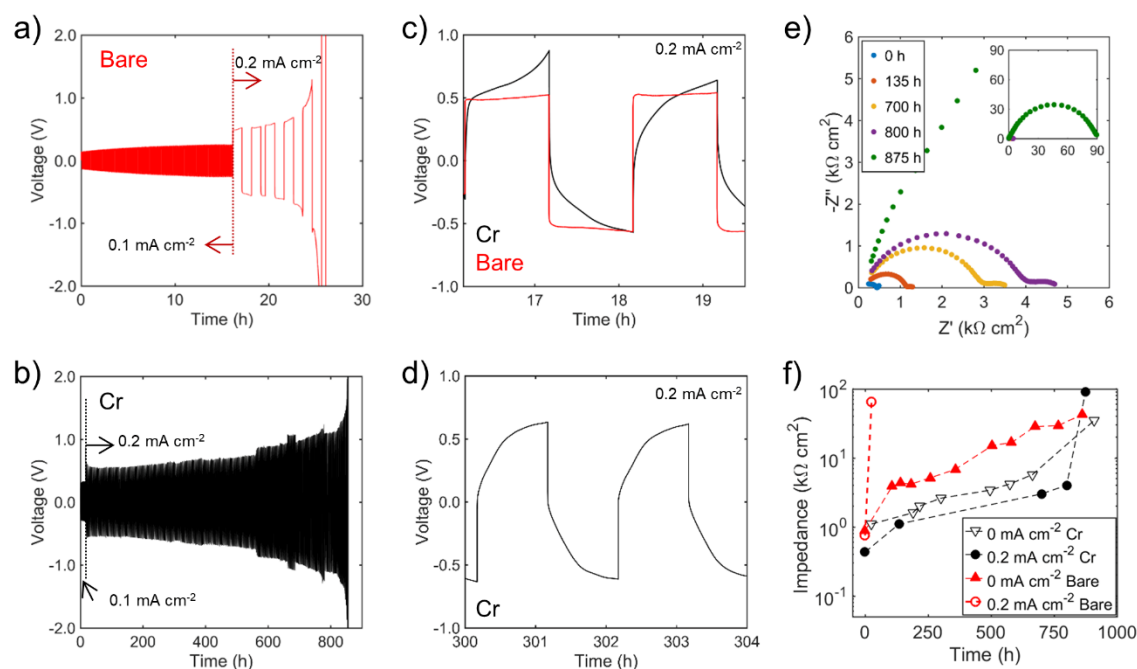


Figure 2.1. Electrochemistry of symmetric cells with and without Cr protection layers. **a)** Galvanostatic cycling of a symmetric Li/LAGP/Li cell with bare interfaces at 0.2 mA cm^{-2} . **b)** Galvanostatic cycling of a symmetric Li/LAGP/Li cell with 30 nm of Cr at both interfaces at 0.2 mA cm^{-2} . **c, d)** Magnified view of cycling of the two cells at different times, with (c) showing curves from both cells and (d) showing only the protected cell at longer times. **e)** Electrochemical impedance spectra of the cell presented in b collected at various times throughout cycling. **f)** Comparison of the evolution of total cell impedance over time among various cells, with the impedance plotted on a logarithmic scale. This plot shows the cell in panel (b) with 30 nm Cr interface layers cycled at 0.2 mA cm^{-2} (black circles), an identical cell through which no current was applied (empty triangles), a cell without any protection or current applied (red triangles), and an unprotected cell at 0.2 mA cm^{-2} (empty red circles).

As shown in Figure 2.1, the use of Cr as a protection layer significantly extends the cycling duration of symmetric Li/LAGP/Li cells. Without the Cr layer, the symmetric cell with bare LAGP cycled for a total of 25 h before reaching the voltage limit of 2 V (Figure 2.1a). In contrast, the symmetric cell with Cr on both sides of the LAGP cycled for 850 h at the same current density and similar overpotentials (Figure 2.1b). Our previous report on cycling of bare LAGP within symmetric cells also showed lifetimes of ~30 h at current densities of 0.2 mA cm^{-2} .¹⁸ Other protection layers, such as Al and Ge, have also shown improved cycling up to 200 h at current densities between 0.1 and 0.3 mA cm^{-2} .^{29,30} We note that Cr is not expected to react with Li to form an alloy at room temperature,³⁹ as opposed to Al or Ge.^{40–43} For this reason, we expect that Cr will remain as a thin film at the interface without reacting, and it will not diffuse into the Li metal electrode. The results in Figure 2.1b are among the longest cycling reported for LAGP in symmetric Li/Li cells at these moderate current densities, as seen in Table 2.1. Figure 2.1c, d show magnified views of the galvanostatic curves from cycling at shorter times (Figure 2.1c) and longer times (Figure 2.1d). The shape of the curves with and without Cr are distinct in Figure 2.1c, with the Cr-free cell featuring flatter curves. The shape of the curves from the cell with Cr are relatively stable over time (Figure 2.1d).

Table 2.1. Performance benchmarks for protection layers in NASICON symmetric cells.

Solid Electrolyte	Protection Layer	Current Density (mA cm^{-2})	Temperature ($^{\circ}\text{C}$)	Symmetric Cell Cycling Duration (h)	Reference
LAGP	Cr	0.2	RT	850	This work
LAGP	Cr on Al_2O_3	0.2	RT	1200	This work
LAGP	Ge	0.3	RT	200	29
LATP	BN + PEO* + PEGDE**	0.3	60	500	26

Table 2.1. continue

Solid Electrolyte	Protection Layer	Current Density (mA cm ⁻²)	Temperature (°C)	Symmetric Cell Cycling Duration (h)	Reference
LATP	Modified Li SEI + Li ₃ PO ₄ + liquid electrolyte	0.05	RT	200	27
LATP	Al ₂ O ₃	0.01	RT	500	28
LATP	ZnO	0.2	RT	1000	44
LAGP	Amorphized LAGP	0.1 1	60 80	200 40	34
LAGP	LiPON	0.1 1	60 80	200 40	34
LAGP	Al	0.1	50	150	30

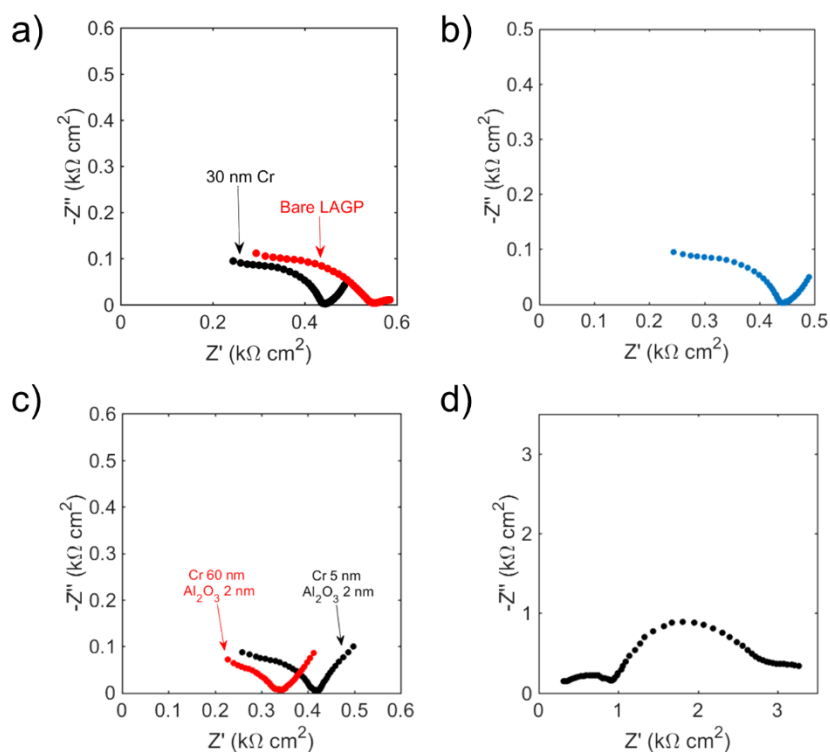


Figure 2.2. Impedance spectra of LAGP with various deposited protection layers and Li on both sides before cycling. **a)** Bare LAGP compared to LAGP with 30 nm of Cr. **b)** 30 nm of Cr 6 nm of Al₂O₃. **c)** 5 or 60 nm of Cr deposited onto 2 nm of Al₂O₃. **d)** 5 nm of Cr deposited on 12 nm Al₂O₃. The thickness of Cr did not affect the initial impedance, but the

thicker Al_2O_3 leads to increased impedance. Notice the differences in the spectra shown in (a) - (c) are minor and are within sample-to-sample variation.

Figure 2.1e shows electrochemical impedance spectra collected at different times during cycling of the Cr-protected cell in Figure 2.1b. The initial impedance spectra of bare and Cr-protected LAGP are very similar (Figure 2.2). Both exhibit one semicircle in the frequency space surveyed, which is typical for LAGP.^{18,19} Total impedance is thus reported here since this metric defines the performance of the cells. The cell impedance remained relatively low during cycling and slowly increasing over time, but the impedance suddenly increased to $\sim 90 \text{ k}\Omega \text{ cm}^2$ over the last 75 h of cycling. This is likely due to mechanical fracture of the LAGP driven by the continuous formation of the interphase, as previously shown in unprotected cells.^{18,19} Figure 2.1f shows the cell impedance over time for this Cr-protected cell and another Cr-protected cell with no current applied. This plot also shows impedance data from two different symmetric cells with bare interfaces; one was operated at 0.2 mA cm^{-2} and the other had no current applied. Interestingly, Figure 2.1f shows that the increase of impedance over time for the Cr-protected cell cycled at 0.2 mA cm^{-2} followed a trajectory similar to that of the identical cell without any current applied. In both cases, the impedance of these Cr-protected cells increases at roughly the same rate during the first $\sim 650 \text{ h}$, resulting in a much higher impedance at the end of the experiments. The magnitude of the impedance of the Cr-protected cell at zero current is slightly higher than the cell at 0.2 mA cm^{-2} during the first $\sim 650 \text{ h}$, but this is due to sample-to-sample variation. We note that interphase formation can still occur without applied current through direct chemical reaction, and bare LAGP has shown substantially improved chemo-mechanical stability under such conditions compared to when current is applied.¹⁸ After $\sim 850 \text{ h}$, the impedance of both cells without current and the Cr-protected cell under applied current were all of similar magnitude. These results are significant since

they suggest that Cr-protected interfaces behave similarly both with and without an applied current, which differs from the unprotected case (bare cells with an applied current failed after 30 h, as shown in Figure 2.1f).

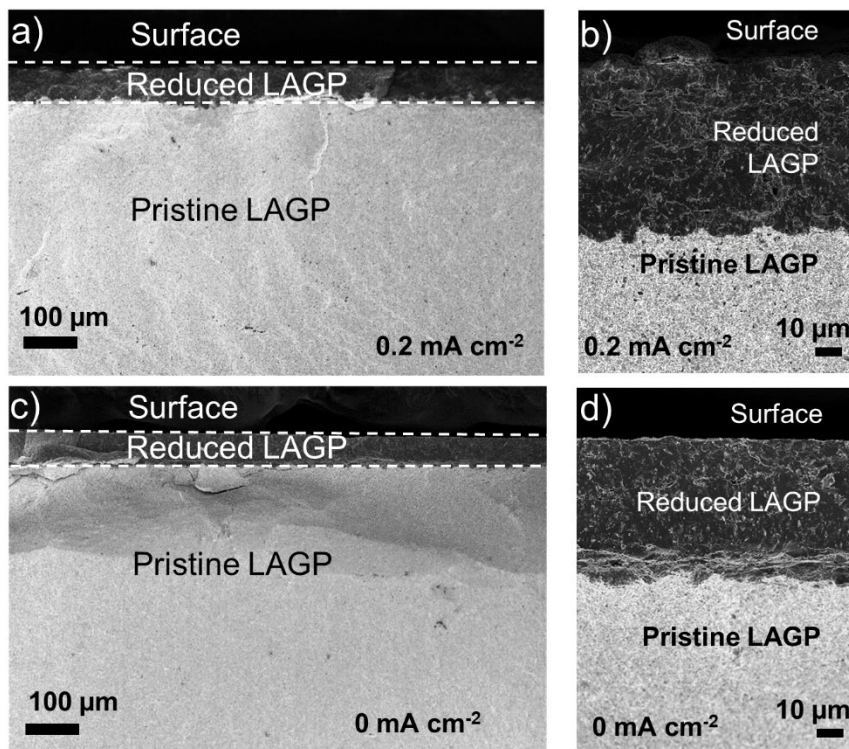


Figure 2.3. Comparison of the interphase morphology between bare and protected LAGP. **a, b)** Cross-sectional SEM images of Cr-protected LAGP from a symmetric Li/LAGP/Li cell cycled at 0.2 mA cm^{-2} for 570 h at low magnification (a) and at high magnification (b). **c, d)** Cross-sectional SEM images of Cr-protected LAGP from an identical cell held for 660 h at open circuit.

Additional investigation showed that the significantly increased stability is not due to the total prevention of reacted interphase formation by the Cr layers. Two identical symmetric cells with Cr-protected LAGP were constructed and tested under different conditions. One cell was cycled at 0.2 mA cm^{-2} for 570 h, and the other cell was held at open circuit without any applied current for 660 h. Figure 2.3 shows SEM images of the interphase region formed electrochemically (Figure 2.3a, b) and chemically (Figure 2.3c,

d). The darker contrast of the interphase in the SEM images arises because of the higher electronic conductivity of the interphase and the incorporation of a significant amount of Li, which has a lower atomic number. The thickness and morphology of the interphase for both cells is very similar, which is consistent with the impedance evolution discussed in Figure 2.1f. In both cases, the interphase is uniform and planar, with a sharp reaction front separating it from the pristine LAGP. This information is important for two reasons. First, it is clear that the Cr layer does not prevent the chemical reaction even when no current is applied, which indicates that Li atoms can diffuse through the Cr interlayer and react with the underlying LAGP. Second, the uniform morphology of the interphase in Figure 2.3a is significantly different than the non-uniform interphase that forms under identical electrochemical conditions with unprotected LAGP.¹⁸ Currents of 0.2 mA cm^{-2} in unprotected cells cause filamentary interphase morphologies, which results in mechanical stress concentrations that significantly accelerate chemo-mechanical degradation.¹⁸ Uniform and planar interphases avoid these stress concentrations and can be stable for much longer times. We thus conclude that the Cr layer causes the interphase to grow much more uniformly than in unprotected cells under the same current conditions, and that this planar interphase morphology is responsible for the significantly improved electro-chemo-mechanical stability.

Despite this improved performance, Cr-protected symmetric cells cycled at higher currents were observed to exhibit shorter cycle life. Post-mortem cross-sectional SEM of Cr protected cells cycled at 0.3 mA cm^{-2} for over 120 h revealed filament-like interphase growth as well as interphase formation deep into the bulk of the pellet, which results in chemo-mechanical degradation and fracture (Figure 2.4). This indicates the existence of a current density limit above which the Cr layer no longer enables a uniform and planar reaction front to grow. The filament-like growth and the presence of interphase within the

bulk of the pellet resembles the growth of Li filaments reported in garnets,^{45,46} and the recent measurements of Li metal formation within the bulk of $\text{Li}_7\text{La}_3\text{Zr}_2\text{O}_{12}$ and $\text{Li}_2\text{S-P}_2\text{S}_5$.⁴⁷

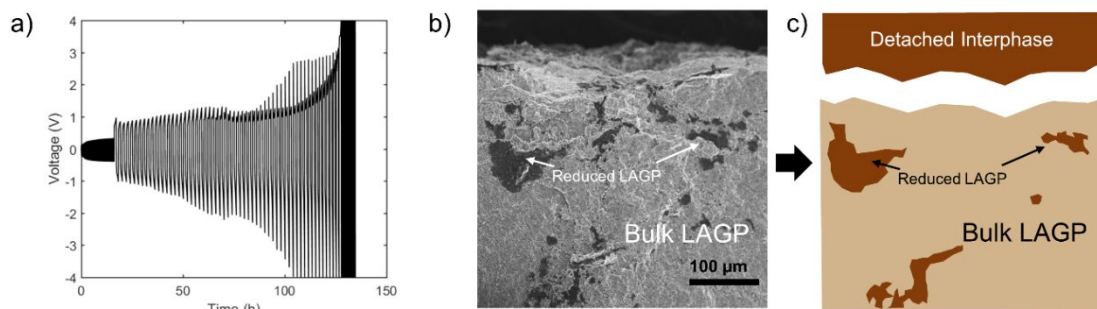


Figure 2.4. Cr-protected LAGP cycled at 0.3 mA cm^{-2} . **a)** Galvanostatic cycling until failure. **b)** Cross-sectional SEM of the cell in (a) where the interphase had been detached from the pellet; the interphase covered the top portion of the pellet. **c)** Schematic representation of (b) to illustrate the detachment of the interphase.

The interphase formation observed in the electrochemically-cycled sample in Figure 2.3 gives rise to an important question: is Li being plated/stripped, or is all the current being used for the electrochemical reaction of the SSE? It is difficult to determine the amount of Li plating/stripping solely from the electrochemical response in galvanostatic cycling of symmetric cells,⁴⁸ and the extended galvanostatic cycling thus does not directly translate into extended Li plating/stripping. To address this question, we designed an open-top cell, as depicted in the inset of Figure 2.5a. This cell was operated by applying current in one direction to cause reduction at the deposited Cr layer on the top side of the cell, which was exposed to the argon environment of a glove box. Both sides of the LAGP pellet were coated with the Cr layer, but only one side of the pellet was initially in contact with Li. With this cell, we can detect reaction products on the “open-top” side of the pellet without the presence of a thick Li foil electrode that obscures the solid-state interface. The Cr layer on the top of the pellet behaves as the electrical contact, and a thicker Cu ring is used as an electrical connection.

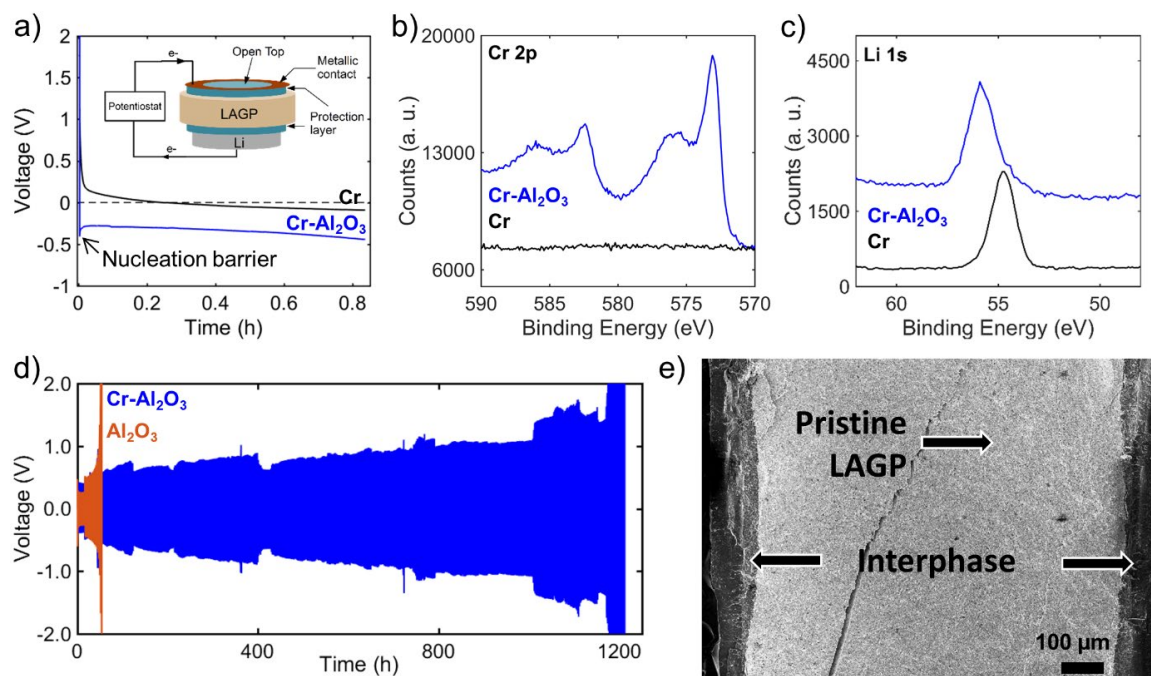


Figure 2.5. Evidence of plating and extended stability with dual-layer protection. **a)** Schematic and data from the open-top cell experiments. The two curves show galvanostatic discharge of open-top cells at 0.1 mA cm^{-2} with 30 nm Cr (black) and 30 nm Cr on 6 nm Al₂O₃ (blue). **b)** Chromium 2p and **c)** lithium 1s XPS spectra of the open top surface after galvanostatic discharge of both samples. Deviations in peak positions of Li 1s are attributed to sample-to-sample variation, but the presence of Li species is verified with these results. **d)** Galvanostatic cycling from symmetric cells with the LAGP coated with either dual-layer Cr-Al₂O₃ (blue) or Al₂O₃ alone (orange). The Al₂O₃ was 6 nm in both cases, and the Cr was 30 nm. **e)** *Post-mortem* cross-sectional SEM of the Cr-Al₂O₃ protected cell after failure showing uniform interphase growth on both sides of the pellet.

The electrochemical signatures from galvanostatic experiments with two different open-top cells are presented in Figure 2.5a. The black trace in Figure 2.5a is from an open-top cell with only a 30 nm Cr layer on top, while the blue trace is from an open-top cell with a bilayer of 30 nm Cr on top of 6 nm Al₂O₃ deposited by atomic layer deposition (ALD). For the cell with only Cr, the cell voltage remained above 0 V during the initial stages of the discharge and gradually fell below 0 V after 0.2 h. The XPS data shown in Figure 4.4b, c indicate that Li entirely covered the Cr layer, since the Cr 2p peaks are no longer visible after discharge. These data suggest that while there is some electrochemical reaction of the LAGP at higher potentials, there is also some Li metal deposition to cover

the Cr layer. The cell with the Cr-Al₂O₃ bilayer was also constructed and tested to examine the effects of the electronically-insulating Al₂O₃ layer (which likely converts to a Li⁺-conducting LiAlO_x phase in contact with Li^{49–52}). For this bilayer cell, the cell voltage immediately became negative under applied current in Figure 2.5a, and the voltage showed an initial dip typically associated with a nucleation overpotential.^{53–55} This behavior suggests that this sample features direct electrochemical deposition of Li metal without significant reaction of the LAGP to form an interphase. However, the XPS data shown in Figure 2.5b, c show that Cr 2p peaks are detected after plating Li within this bilayer cell, which likely means that Li did not plate uniformly when the Al₂O₃ layer was added between Cr and LAGP. These results indicate that the initial electrochemical behavior of the interface can be directed through judicious choice of interfacial layers.

Although the Cr-Al₂O₃ bilayer enabled preferential lithium deposition without interphase formation in the early times of this experiment, long-term cycling still resulted in the reaction of LAGP and the formation of a uniform interphase. However, the dual layer also enabled a significant extension in cycle life in symmetric cells at a current density of 0.2 mA cm⁻², similar to Cr alone, as shown in Figure 2.5d. A 6 nm layer of Al₂O₃ alone at the interface did not result in improved stability (Figure 2.5d), indicating that the Cr layer was again necessary. Figure 2.5e shows that the interphase formed using the Cr-Al₂O₃ dual layer during the experiment in Figure 2.5d is indistinguishable from that formed using Cr alone. We expect that the initial electron blocking effect that favors Li plating over LAGP reduction is lost over time as the Al₂O₃ transforms to a phase that is more electronically conducting, as well as because the Al₂O₃ layer can be mechanically damaged as the underlying LAGP reacts and expands to form the interphase. As the bilayer evolves to become more electronically conductive, LAGP reduction becomes more favored. In sum, a Cr-Al₂O₃ protection layer is not practically different from a Cr protection layer. We note

that thicker Al_2O_3 layers were also tested within the bilayer, which significantly increased impedance (Figure 2.4).

Finally, we examined the effects of the Cr interfacial layer on the electrochemistry of full cells. The cathode in these cells consisted of LiFePO_4 (LFP) active material embedded in a poly(ethylene oxide) (PEO)-based polymer-electrolyte composite which was drop-cast on the top of the LAGP pellet (see Experimental). As shown in Figure 2.6, the Cr interfacial layer at the Li metal interface also extends stability of these full cells, and the full cells provide additional understanding of the behavior of these interfaces. Figure 2.6 shows the cycling behavior of Li/LAGP/LFP cells tested at 60 °C using a current density of 0.1 mA cm^{-2} . The data from the Cr-protected LAGP cell in Figure 2.6b, c show much greater cycling stability than the data from the bare sample in Figure 2.6a. Figure 2.6c shows the Coulombic efficiency during cycling of these two samples, with the Cr-protected LAGP cell exhibiting sustained high efficiency during cycling. The extended cyclability attained with Cr is again connected to the improved chemo-mechanical stability of the LAGP pellet. Figure 2.6d shows that a planar, uniform interphase was formed on the anode side of a similar sample with no signs of fracture after 500 cycles. We believe that failure of these protected cells occurs not due to fracture, but due to delamination of the cathode (as can be seen in Figure 2.6d).

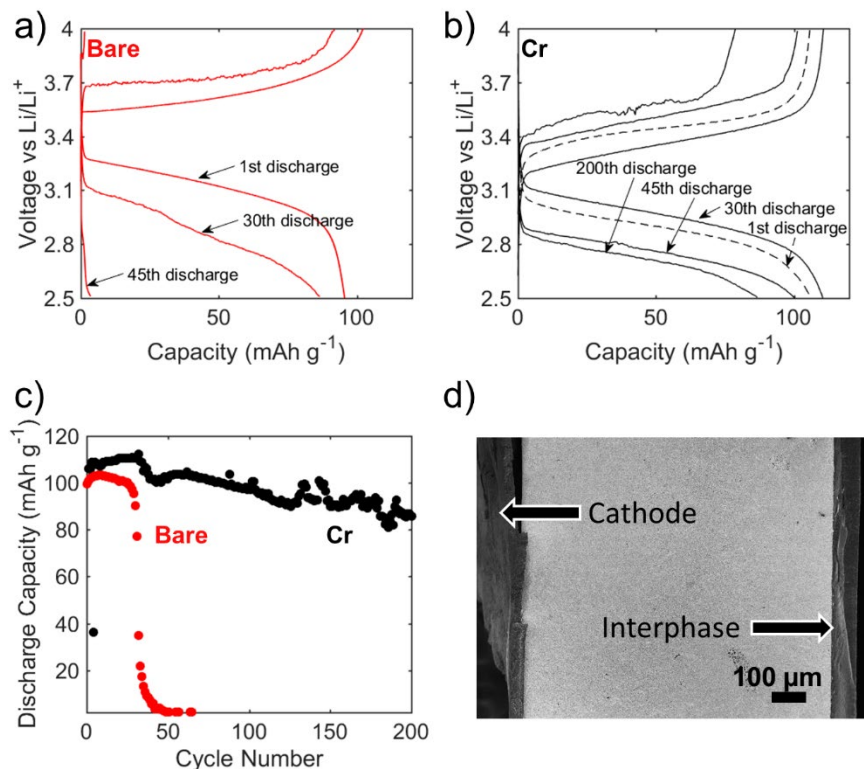


Figure 2.6. Characterization of full cells with a LiFePO_4 cathode. **a)** Galvanostatic charge/discharge curves at 0.1 mA cm^{-2} from a Li/LAGP/LFP cell with uncoated interfaces. **b)** Galvanostatic charge/discharge curves at 0.1 mA cm^{-2} from a Li/LAGP/LFP cell with the Li interface coated with 30 nm of Cr. The cells in (a) and (b) were tested at 60°C . **c)** Discharge capacity for the cells in (a) and (b). **d)** Post-mortem cross-sectional SEM image of a protected cell after cycling for 500 cycles.

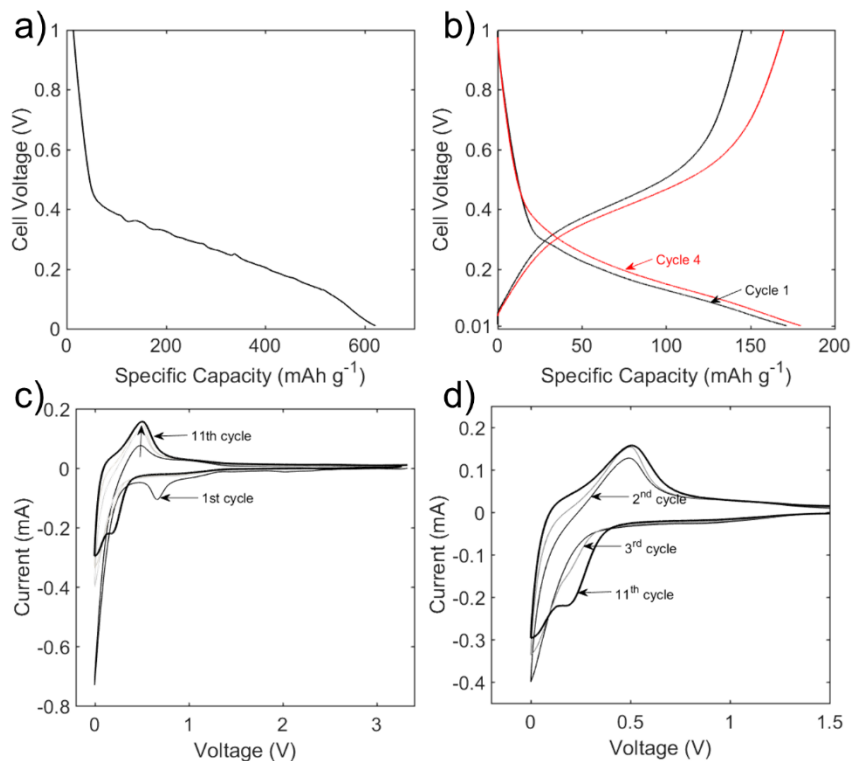


Figure 2.7. Electrochemical behavior of half cells with liquid electrolytes with an LAGP composite slurry electrode as the working electrode. a) Galvanostatic discharge at 0.004 mA cm^{-2} . b) Galvanostatic cycling at 0.016 mA cm^{-2} . c) Cyclic voltammetry at a sweep rate of 0.1 mV s^{-1} . d) Inset of (c) starting from the second cycle.

Another feature evident from Figure 2.6a and b is that the Cr interlayer alters the voltage of the full cell. As shown in Figure 2.6a and b, the galvanostatic curves of the Cr-protected LAGP cell consistently show lower charge/discharge voltages than the bare cells by about 0.3 V. The average voltage of $\sim 3.4 \text{ V}$ for the bare cell (Figure 2.6a) is consistent with the use of an LFP cathode and Li plating/stripping at the anode. The reduction in cell voltage for the Cr-coated cell is most likely due to the negative electrode reaction being reversible conversion of the LAGP instead of Li plating/stripping. To further investigate this possibility, we constructed conventional slurry-based electrodes with LAGP powder and examined their electrochemical behavior within liquid-electrolyte half cells (see Experimental Details section). Cyclic voltammetry and galvanostatic cycling of

LAGP working electrodes showed that this material undergoes redox (likely a conversion reaction) between about 0.2 and 0.4 V vs. Li/Li⁺ (Figure 2.7). These additional results provide strong evidence that the shift in voltage of the Cr-protected solid-state cell in Figure 2.6b is due to reversible conversion reaction of the LAGP at the anode. Thus, these findings suggest that without the Cr protection layer, Li/LAGP/LFP full cells operate via Li plating/stripping at the anode, but when the Cr layer is added, it promotes the direct electrochemical conversion reaction of the LAGP. In the Cr-protected LAGP cells, the Cr layer represents an additional barrier for Li transport, which could frustrate Li plating/stripping and favor electrochemical conversion. These findings are largely consistent with the open-top cell shown in Figure 2.5a, in which reduction occurred above 0.0 V vs. Li/Li⁺. However, the XPS observation of coverage of the Cr layer in Figure 2.5c suggested at least some Li deposition, which could have occurred because of the open space above Cr in this configuration or the different electrochemical nature of the cell.

As shown herein, the addition of the sputtered Cr film caused the interphase to grow in a very uniform and planar fashion at current densities up to 0.2 mA cm⁻², which is in contrast to filamentary growth in bare cells which leads to chemo-mechanical degradation and cell failure. We propose that the significantly improved stability of the cells with Cr-coated interfaces, as well as the differences in electrochemical behavior in full cells, are due to the Cr layer acting to remove electric field concentrations and other sources of ionic current “hot-spots” at the interface. The improved physical contact and coverage of the vapor-deposited Cr film compared to a pure Li electrode on the LAGP surface is one probable source of this behavior, as it removes point contacts present when using Li foils that could result in electric field/ionic current concentrations and filamentary interphase growth.⁵⁶ Sputter deposition of the Cr creates a uniform film in intimate contact with the polished polycrystalline LAGP surface. The Li electrodes, on the other hand, are bulk foils that are much rougher and exhibit non-uniform contact at the LAGP surface. This

argument also explains the success of other reported vapor-deposited protection layers, such as Ge.²⁹ Finally, it is also possible that these various metal interlayers impact charge transfer and interphase growth trajectories via altering the partial molar volume of Li, as has been predicted previously.⁵⁷

At higher current densities, filamentary growth of the interphase occurs following a mechanism similar to that reported for bare LAGP.¹⁸ Beyond 0.2 mA cm⁻², the rate of reaction is accelerated and minor irregularities due to surface roughness or grain boundaries create preferential pathways for ionic transport and interphase formation. We hypothesize that, while electron transport can be uniform due to the metallic Cr protection layer, Li⁺ transport is still restricted due to imperfect contact, which can lead to preferential localized growth of the interphase. Since the interphase is a MIEC,^{16,17} reduction of pristine LAGP is favored at the interphase protrusions, where the ion transport distance is shorter.¹⁸ It is possible that higher pressures⁵⁸ or other strategies to improve contact at the interface could improve stability at higher current densities.

2.4: Conclusions

This work shows that metallic protection layers can enable >1000 h of cycling time for NASICON-based lithium metal batteries, and it provides important insights into the mechanisms through which these metallic protection layers operate. We demonstrate that engineering the Li-SSE interface with metallic layers enables control over the evolution of the interphase, which is key for the long-term stability of LAGP. Cr interlayer films were found to significantly extend the lifetime of symmetric and full cells by promoting uniform interphase growth and delaying fracture at moderate current densities. At the same time, the Cr layers promoted reversible electrochemical conversion of the LAGP material instead of Li deposition/stripping. Experiments with electron-blocking Cr-Al₂O₃ bilayers

showed initial promotion of Li plating, but long-term stability and interphase growth was similar to Cr alone. These results are important since they demonstrate the underlying mechanisms that govern the action of metallic protection layers. In particular, the ability of the 30 nm Cr layers to allow Li^+ to be transported while also reducing ion transport non-uniformities and improving stability could be beneficial when used with a variety of SSE materials. For ultimate stability, however, true electron-blocking layers to entirely prevent interphase formation, or other layers that can significantly slow the growth of the interphase, are seemingly required. In either case, the use of metallic layers in conjunction with these future protection materials could be advantageous. Thus, we expect that the findings reported here are an important step on the way toward the development of a diverse array of solid-state battery chemistries with long-term stability and high energy.

2.5: References

1. U. von Sacken, E. Nodwell, A. Sundher, and J. R. Dahn, *J. Power Sources*, 54, 240–245 (1995).
2. R. Bhattacharyya, B. Key, H. Chen, A. S. Best, A. F. Hollenkamp, C. P. Grey, *Nat. Mater.*, 9, 504–510 (2010).
3. Y. Kato, S. Hori, T. Saito, K. Suzuki, M. Hirayama, A. Mitsui, M. Yonemura, H. Iba, R. Kanno. *Nat. Energy*, 1 (2016).
4. N. Kamaya, K. Homma, Y. Yamakawa, M. Hirayama, R. Kanno, M. Yonemura, T. Kamiyama, Y. Kato, S. Hama, K. Kawamoto, A. Mitsui, *Nat. Mater.*, 10, 682–686 (2011).
5. H. Aono, E. Sugimoto, Y. Sadaoka, N. Imanaka, and G. Adachi, *J. Electrochem. Soc.*, 137, 1023 (1990).
6. J. Wolfenstine, J. Ratchford, E. Rangasamy, J. Sakamoto, and J. L. Allen, *Mater. Chem. Phys.*, 134, 571–575 (2012).
7. R. Murugan, V. Thangadurai, and W. Weppner, *Angew. Chem. Int. Ed.*, 46, 7778–7781 (2007).
8. K. Kerman, A. Luntz, V. Viswanathan, Y. Chiang, and Z. Chen, *J. Electrochem. Soc.* 167, A1731-A1744 (2017).

9. M. Kotobuki, H. Munakata, K. Kanamura, Y. Sato, and T. Yoshida, *J. Electrochem. Soc.* 157, A1076-A1079 (2010).
10. N. Riphaut, B. Stiaszny, H. Beyer, S. Indris, H. A. Gasteiger, and S. S. J. Sedlmaier, *J. Electrochem. Soc.* 166, A975-A983 (2019).
11. Y. Zhu, X. He, and Y. Mo, *ACS Appl. Mater. Interfaces*, 7, 23685–23693 (2015).
12. V. Augustyn, M. T. McDowell, and A. Vojvodic, *Joule*, 2, 2189–2193 (2018).
13. C. Ma, Y. Cheng, K. Yin, J. Luo, A. Sharafi, J. Sakamoto, J. Li, K. L. More, N. J. Dudney, M. Chi, *Nano Lett.*, 16, 7030–7036 (2016).
14. A. Sharafi, H. M. Meyer, J. Nanda, J. Wolfenstine, and J. Sakamoto, *J. Power Sources*, 302, 135–139 (2016).
12. S. Wenzel, D. A. Weber, T. Leichtweiss, M. R. Busche, J. Sann, J. Janek, *Solid State Ionics*, 286, 24–33 (2016).
16. P. Hartmann, T. Leichtweiss, M. R. Busche, M. Schneider, M. Reich, J. Sann, P. Adelhelm, J. Janek, *J. Phys. Chem. C*, 117, 21064–21074 (2013).
17. S. Wenzel, S. Randau, T. Leichtweiß, D. A. Weber, J. Sann, W. G. Zeier, J. Janek, *Chem. Mater.*, 28, 2400–2407 (2016).
18. J. A. Lewis, F. J. Q. Cortes, M. G. Boebinger, J. Tippens, T. S. Marchese, N. Kondekar, X. Liu, M. Chi, M. T. McDowell, *ACS Energy Lett.*, 4, 591–599 (2019).
19. J. Tippens, J. C. Miers, A. Afshar, J. A. Lewis, F. J. Q. Cortes, H. Qiao, T. S. Marchese, C. V. Di Leo, C. Saldana, M. T. McDowell, *ACS Energy Lett.*, 4, 1475–1483 (2019).
20. J. A. Lewis, J. Tippens, F. J. Q. Cortes, and M. T. McDowell, *Trends Chem.*, DOI: 10.1016/j.trechm.2019.06.013 (2019).
21. K. He, C. Zu, Y. Wang, B. Han, X. Yin, H. Zhao, Y. Liu, J. Chen, *Solid State Ion.*, 254, 78–81 (2014).
22. M. Zhang, K. Takahashi, N. Imanishi, Y. Takeda, O. Yamamoto, B. Chi, J. Pu, J. Li, *J. Electrochem. Soc.*, 159, A1114–A1119 (2012).
23. H. Kitauro and H. Zhou, *Energy Environ. Sci.*, 5, 9077 (2012).
24. H. Chung and B. Kang, *Chem. Mater.*, 29, 8611–8619 (2017).
25. M. Nagao, A. Hayashi, and M. Tatsumisago, *Electrochemistry*, 80, 734–736 (2012).
26. Q. Cheng, A. Li, N. Li, S. Li, A. Zangiabadi, T.-D. Li, W. Huang, A. C. Li, T. Jin, Q. Song, W. Xu, N. Ni, H. Zhai, M. Dontigny, K. Zaghib, X. Chuan, D. Su, K. Yan, Y. Yang, *Joule*, 3, 6, 1510 (2019)
27. J. Liu, T. Liu, Y. Pu, M. Guan, Z. Tang, F. Ding, Z. Xu, Y. Li, *RSC Adv.*, 7, 46545–46552 (2017).

28. Y. Liu, Q. Sun, Y. Zhao, B. Wang, P. Kaghazchi, K. R. Adair, R. Li, C. Zhang, J. Liu, L.-Y. Kuo, Y. Hu, T.-K. Sham, L. Zhang, R. Yang, S. Lu, X. Song, X. Sun, *ACS Appl. Mater. Interfaces*, 10, 31240–31248 (2018).
29. Y. Liu, C. Li, B. Li, H. Song, Z. Cheng, M. Chen, P. He, H. Zhou, *Adv. Energy Mater.*, 8, 1702374 (2018).
30. H. Zhong, L. Sang, F. Ding, J. Song, and Y. Mai, *Electrochim. Acta*, 277, 268–275 (2018).
31. X. Han, Y. Gong, K. Fu, X. He, G. T. Hitz, J. Dai, A. Pearse, B. Liu, H. Wang, G. Rubloff, Y. Mo, V. Thangadurai, E. D. Wachsman, L. Hu. *Nat. Mater.*, 16, 572–579 (2017).
32. E. Zhao, F. Ma, Y. Guo, and Y. Jin, *RSC Adv.*, 6, 92579–92585 (2016).
33. H. S. Jadhav, R. S. Kalubarme, A. H. Jadhav, and J. G. Seo, *Electrochim. Acta*, 199, 126–132 (2016).
34. Z. Zhang, S. Chen, J. Yang, G. Liu, X. Yao, P. Cui, X. Xu, *Electrochim. Acta*, 297, 281–287 (2019).
35. C. Wang, Y. Yang, X. Liu, H. Zhong, H. Xu, Z. Xu, H. Shao, F. Ding, *ACS Appl. Mater. Interfaces*, 9, 13694–13702 (2017).
36. D. Bosubabu, J. Sivaraj, R. Sampathkumar, and K. Ramesha, *ACS Appl. Energy Mater.*, 2, 6, 4118–4125 (2019).
37. Y. Zhu, X. He, and Y. Mo, *Adv. Sci.*, 4, 1600517 (2017).
38. A. M. Nolan, Y. Zhu, X. He, Q. Bai, and Y. Mo, *Joule*, 2, 2016–2046 (2018).
39. M. Venkatraman and J. P. Neumann, *Bull. Alloy Phase Diagrams*, 5, 399–400 (1984).
40. L. F. Mondolfo, *Aluminum Alloys*, 308–311 (1976).
41. J. Sangster and A. D. Pelton, *J. Phase Equilibria*, 18, 289–294 (1997).
42. M. H. Tahmasebi, D. Kramer, R. Mönig, and S. T. Boles, *J. Electrochem. Soc.*, 166, A5001–A5007 (2019).
43. F. J. Q. Cortes, M. G. Boebinger, M. Xu, A. Ulvestad, and M. T. McDowell, *ACS Energy Lett.*, 3, 349–355 (2018).
44. X. Hao, Q. Zhao, S. Su, S. Zhang, J. Ma, L. Shen, Q. Yu, L. Zhao, Y. Liu, F. Kang, Y. He, *Adv. Energy Mater.*, 9, 1901604 (2019).
45. Y. Ren, Y. Shen, Y. Lin, and C.-W. Nan, *Electrochem. Commun.*, 57, 27–30 (2015).
46. L. Porz, T. Swamy, B. W. Sheldon, D. Rettenwander, T. Frömling, H. L. Thaman, S. Berendts, R. Uecker, W. Craig Carter, Y.-M. Chiang, *Adv. Energy Mater.*, 7, 1701003 (2017).

47. F. Han, A. S. Westover, J. Yue, X. Fan, F. Wang, M. Chi, D. N. Leonard, N. J. Dudney, H. Wang, C. Wang, *Nat. Energy*, 4, 187–196 (2019).
48. K.-H. Chen, K. N. Wood, E. Kazyak, W. S. LePage, A. L. Davis, A. J. Sanchez, N. P. Dasgupta, *J. Mater. Chem. A*, 5, 11671–11681 (2017).
49. S. C. Jung and Y.-K. Han, *J. Phys. Chem. Lett.*, 4, 2681–2685 (2013).
50. S.-T. Myung, K. Izumi, S. Komaba, Y.-K. Sun, H. Yashiro, N. Kumagai, *Chem. Mater.*, 17, 3695–3704 (2005).
51. V. Mäikkulainen, O. Nilsen, H. Li, S. W. King, M. Laitinen, T. Sajavaara, H. Fjellvåg, *J. Vac. Sci. Technol. A*, 33, 01A101 (2015).
52. E. Kazyak, K. N. Wood, and N. P. Dasgupta, *Chem. Mater.*, 27, 6457–6462 (2015).
53. K. Yan, Z. Lu, H.-W. Lee, F. Xiong, P.-C. Hsu, Y. Li, J. Zhao, S. Chu, Y. Cui, *Nat. Energy*, 1, 16010 (2016),
54. K. N. Wood, E. Kazyak, A. F. Chadwick, K.-H. Chen, J.-G. Zhang, K. Thornton, N. P. Dasgupta, *ACS Cent. Sci.*, 2, 790–801 (2016).
55. T. Krauskopf, R. Dippel, H. Hartmann, K. Peppler, B. Mogwitz, F. Richter, W. G. Zeier, J. Janek, *Joule*, 3, 1 (2019).
56. T. Krauskopf, H. Hartmann, W. G. Zeier, J. Janek, *ACS Appl. Mater. Interfaces*, 11, 14463–14477 (2019).
57. Z. Ahmad and V. Viswanathan, *Phys. Rev. Lett.*, 119, 056003 (2017).
58. M. J. Wang, R. Choudhury, J. Sakamoto, *Joule*, DOI: 10.1016/j.joule.2019.06.017 (2019).

CHAPTER 3: CURRENT CONSTRICTION AT THE SOLID ELECTROLYTE-LITHIUM INTERFACE*

3.1: Introduction

Our previous discussion in Chapter 2 showed that it is possible to extend the stability of solid electrolytes by engineering the interface between the solid electrolyte and lithium. A common thread among publications that reveal extended cyclability of both stable and unstable solid electrolytes is that improving interfacial contact is key.^{1,2} In Chapter 2, we showed that using a non-alloying metallic contact at the interface also extended the cyclability of a solid electrolyte, which suggests that not only the mechanical contact but also the uniformity of the electric field might play a role. Studying the interfacial contact between lithium and the solid electrolyte is challenging due to the fact that it is a buried interface, and only a few techniques allow for direct probing. In this chapter, we present *operando* X-ray tomography examinations of the Li-SSE interface and reveal the role and evolution of contact.

The challenge of interfacial contact between lithium metal and solid electrolytes has been addressed in various ways before. Different approaches to enhance the 'lithiophilicity' of the surface of the solid electrolyte as well as efforts to understand the role of pressure demonstrate the fundamental role of interfacial contact.^{1,3-5} In the case of

* A significant fraction of the work presented here has been submitted for publication as: John A. Lewis, Francisco Javier Quintero Cortes, Yuhgene Liu, John C. Miers, Ankit Verma, Bairav S. Vishnugopi, Jared Tippens, Dhruv Prakash, Thomas S. Marchese, Sang Yun Han, Chanhee Lee, Pralav P. Shetty, Hyun-Wook Lee, Pavel Shevchenko, Francesco De Carlo, Christopher Saldana, Partha P. Mukherjee, Matthew T. McDowell. "*Linking Void and Interphase Evolution to Electrochemistry in Solid-State Batteries Using Operando X-Ray Tomography*"

$\text{Li}_7\text{La}_3\text{Zr}_2\text{O}_{12}$ (LLZO), for example, a broad range of surface treatments have been used to increase its critical current density.⁶ At the critical current density, lithium dendrites grow through stable solid electrolytes, such as LLZO, and short circuit the cell.¹ From polishing in inert atmosphere⁷ to protection layers including alloying metals⁸, oxides⁶ and silicates⁹, exhibit some degree of success at increasing the critical current density of the solid electrolyte. Similar strategies have been used in less stable solid electrolytes such as LAGP, as discussed in Chapter 2. Another strategy used to increase the critical current density in stable solid electrolytes, such as LLZO and $\text{Li}_6\text{PS}_5\text{Cl}$ (LPSC), is to control the stack pressure.^{1,10,11} Generally, it has been found that increasing the stack pressure leads to lower overpotentials and higher critical current densities.³ At the same time, it has been shown through 3-electrode cell configurations that it is the stripping interface that controls cell failure.¹ Various models to explain these phenomena propose that voids are formed during lithium stripping.^{1,10,12} Interfacial voids reduce the effective contact area and create current density hot-spots, or current constrictions, which lead to dendrite growth and cell failure.¹⁰ However, only limited evidence of those voids is available and measurements of effective contact area are needed.

Current constriction between metallic contacts is a phenomenon that has been well described and modeled since the mid 1900s.^{13,14} Briefly, when the effective contact area between two conductors is smaller than the area of either contact, the lines of current flow converge towards the smaller effective contact area.¹⁵ This phenomenon has typically been described as a constriction resistance. This approximation helps simplify the unknown shape and area of real contacts, and has been used to formulate predictive models based on average distributions and dimensions of contact spots.^{15,16} For theoretical or ideal contacts where the exact area and distribution of the contact spots is known, it is possible to predict the amount of current that flows through each of the contact spots. In those cases, it has been observed that the current density through each spot

tends to be higher when the spots are smaller and when they are further away from the center.¹⁶ The concept of current constriction in metallic contacts translates well into the problem of solid state electrochemical systems. Current flows from one side of the contact to the other, except it takes the forms of ions on one side and electrons on the other. One example of use of this concept is the modeling of solid state fuel cells.^{17,18} The growing interest in understanding the role of interfacial contact in solid state batteries is an opportunity to apply the well-established models for constriction current in this electrochemical system.

In order to make any approximation to modeling the interfacial constriction current, it is necessary to have a detailed characterization of the contacting interface. Due to the buried nature of this interface, X-ray tomography is a natural choice of technique for direct imaging of the evolution of contact at the lithium-solid electrolyte interface. X-ray tomography has been used in battery systems to study the impact of structure, porosity and mechanical properties of materials on cell performance.^{1,19–22} An important challenge that comes with X-ray tomography is that contrast depends on the density and atomic number of the materials being probed, making it difficult to differentiate lithium from voids in many cases.²² One way to improve the contrast between lithium and voids is to use lower X-ray energies. At the same time, lower X-ray energies make it more difficult to image high-density solid electrolytes such as LLZO or LAGP.^{19,22} On the other hand, void formation has been demonstrated using X-ray tomography of LPSC, which suggests that sulfide solid electrolytes are more suitable for this type of study.^{1,20} In this work, we use $\text{Li}_{10}\text{SnP}_2\text{S}_{12}$ (LSPS), which is an unstable solid electrolyte,²³ similar to LAGP (discussed in Chapter 2), in which a continuously growing interphase is formed. Compared to LAGP, this sulfide solid electrolyte has an ionic conductivity two orders of magnitude higher and cells can be fabricated through cold pressing.²³

In this chapter, we model the evolution of constriction current at the interface between lithium metal and a solid electrolyte. We used *operando* X-ray tomography to image the evolution of lithium contact at the interface with the solid electrolyte. The tomographic data were segmented and transformed into contact maps that served as the input to a simple model directly derived from Greenwood¹⁶. The results from this model reveal a broad distribution of current densities across the surface of the solid electrolyte, with values orders of magnitude higher than the nominal current density applied. The approach presented here can be further refined and used in other electrochemical systems to predict voltage evolution and cell failure.

3.2: Methods

Cell Assembly: $\text{Li}_{10}\text{SnP}_2\text{S}_{12}$ (LSPS) was purchased from NEI Corporation. A custom X-ray tomography cell was built for the *operando* synchrotron X-ray tomography experiments. The cell body was constructed out of PEEK to minimize X-ray attenuation and prevent short circuiting between the electrodes. The inner diameter was designed to be 2 mm to minimize the sample size, ensuring sufficient transmission to image the cell. Symmetric Li/LSPS/Li cells were assembled inside of an Ar-filled glovebox. 7 mg of LSPS was loaded into the cell and pressed at a pressure of 225 MPa to form a pellet approximately 1 mm thick. Lithium metal foils were punched out and attached to steel rods, which were then inserted into each side of the cell. To establish the pressure necessary to cycle these cells at high current densities, screws were used to compress the rods against the faces of the pellet. O-rings attached to the screw heads were simultaneously compressed to form a seal when the screw was inserted. The torque applied to the screws was 0.25 N-m (estimated to be greater than 10 MPa) for each experiment unless otherwise specified. Graphite foils were placed between the steel rods

and screws to prevent the rods from rotating and damaging the Li/SSE interface. All operando electrochemical measurements were performed using a Bio-Logic SP-150 potentiostat.

Synchrotron X-Ray Computed Microtomography Experiments: Operando X-ray computed microtomography experiments were conducted at the Advanced Photon Source's 2-BM beamline. Monochromatic X-rays with an energy of 28 keV were chosen to maximize transmission in our samples based on attenuation length calculations (Fig. S3). 1500 projections were taken with an exposure time of 210 ms while rotating the sample 180°. An Oryx 5.0 MP Mono 10GigE detector and a 2 magnification lens were used for the optics in this setup. The sample-to-detector distance for all experiments was 100 mm. We were able to achieve a voxel size of 1.7 μm while fitting the entire sample within the field of view of $\sim 4.2 \times 1.4 \text{ mm}^2$. The time required to complete a scan under these conditions was approximately 7 min. The raw data were reconstructed with TomoPy using the Gridrec method⁶².

Segmentation Analysis: *Lithium segmentation.* The reconstructed images were segmented using MATLAB to identify the lithium volumes across the entire 3D dataset. A dynamic cropping procedure was applied to select the appropriate regions of interest. Schematic representations of the MATLAB procedures used to segment the regions of interest for different phases are shown in Figure 3.1 - 3.3. To identify lithium metal (Figure 3.1), the cropped reconstructed images were analyzed by traversing columns of pixels from the top to the bottom of the image. The sharp difference in intensity between the steel rod and lithium electrode was used to define the upper boundary of the lithium. Traversing downward from the upper boundary, the algorithm continued to recognize pixels as lithium as long as their intensity was below the specified intensity cutoff typical for lithium (Figure

3.1). The identification of lithium in a single pixel column stopped when the average intensity of the next 5 pixels was above a threshold value typical of the interphase. This process repeated for every column until the entire 2D image was segmented; the algorithm was then used to segment each 2D image within the 3D tomographic dataset to identify the entire volume of the lithium electrodes. Analysis using subvolumes was performed by selecting specific regions within these segmented electrodes. 3D renderings of the subvolumes were created using the Dragonfly software platform.

Void segmentation. Void segmentation was performed using a separate algorithm in MATLAB. The segmentation process is schematically illustrated in Figure 3.2. The algorithm traversed pixel columns in 2D image slices from the bulk of the LSPS pellet toward the lithium electrode while identifying pixels with intensities below an intensity cutoff typical for voids. Once such a pixel was found, the algorithm continued identifying the neighboring pixels in the column with intensities below the void cutoff to determine the height of the void. After continued traversal, the algorithm would reach the lithium metal; once the average intensity of five adjacent pixels was representative of lithium metal (i.e., typical of lithium intensity and below the LSPS threshold), all of the identified void pixels were segmented as an interfacial void. If the average intensity of the pixels above the void was higher than the LSPS threshold (i.e., representing LSPS instead of lithium), then the identified void was recognized as a pore in LSPS and was ignored. The algorithm would then continue until an interfacial void was identified or the end of the column was reached. This process was repeated for every column in each 2D image, and subsequently for every image along the interface in the 3D tomographic dataset. 3D renderings of the subvolumes were created using the Dragonfly software platform.

Contact area mapping. The contact area was segmented using a modified version of the lithium volume segmentation algorithm in MATLAB (Figure 3.3). After identifying lithium in every pixel column of a 2D reconstructed image (Figure 3.1), the contact area

algorithm evaluated the five pixels in each column at the edge of the lithium electrode in search of values below the lithium intensity and typical void intensity. If any of these five pixels had intensity below the lithium intensity threshold (i.e., a void is present at the interface), that pixel column was marked as exhibiting no contact at the interface. Otherwise, the pixel column was marked as contacting at the interface. The image slice was then regenerated containing only columns that were marked as having contact. This procedure was performed on every 2D slice of the entire 3D Li/LSPS interface. The modified slices were then projected onto a 2D plane perpendicular to the image slices, yielding a 2D map of the contact area for the entire interface, which are the contact area maps shown in Figure 3.7. In these images, white pixels represent regions where lithium contacts LSPS, while black pixels represent regions with either interfacial voids or no lithium present. The contact area for an interface was calculated by measuring the number of white pixels and using the voxel dimensions to convert this value to physical area.

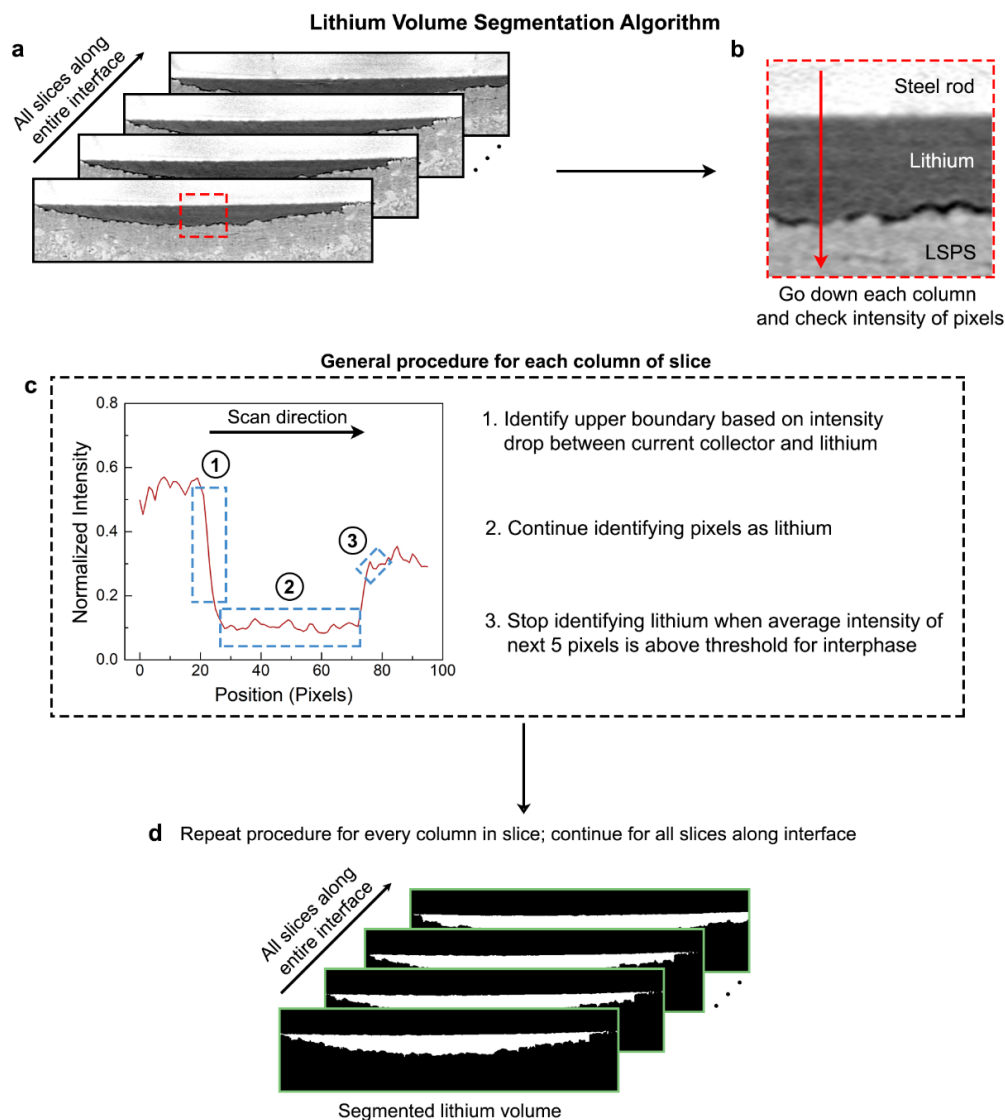


Figure 3.1. Schematic representation of the procedure used to segment the lithium electrodes. **a)** This segmentation procedure is applied to the entire electrode. **b)** The algorithm starts by sequentially traversing each pixel column in a reconstructed 2D image slice. **c)** The intensity profile of the pixels along each column is used to identify the location of lithium metal, which exhibits an intensity below LSPS and the steel rods. First, the upper boundary is defined based on the reduction in intensity at the interface between the steel current collector and lithium electrode (see blue dashed box labeled 1 in (c)). Second, the algorithm continues to recognize pixels along the column as lithium if their intensity is below the specified intensity cutoff typical for lithium (see blue dashed box labeled 2 of the intensity profile). Third, the lower boundary of lithium is identified when the average value of five adjacent pixels in the column is above a threshold value typical of the interphase. **d)** This procedure is repeated for every column in the image slice, and then extended to every image slice along the Li/LSPS interface of the 3D electrode. The final result is the segmented lithium electrode volume consisting of many segmented 2D slices, as shown in (d).

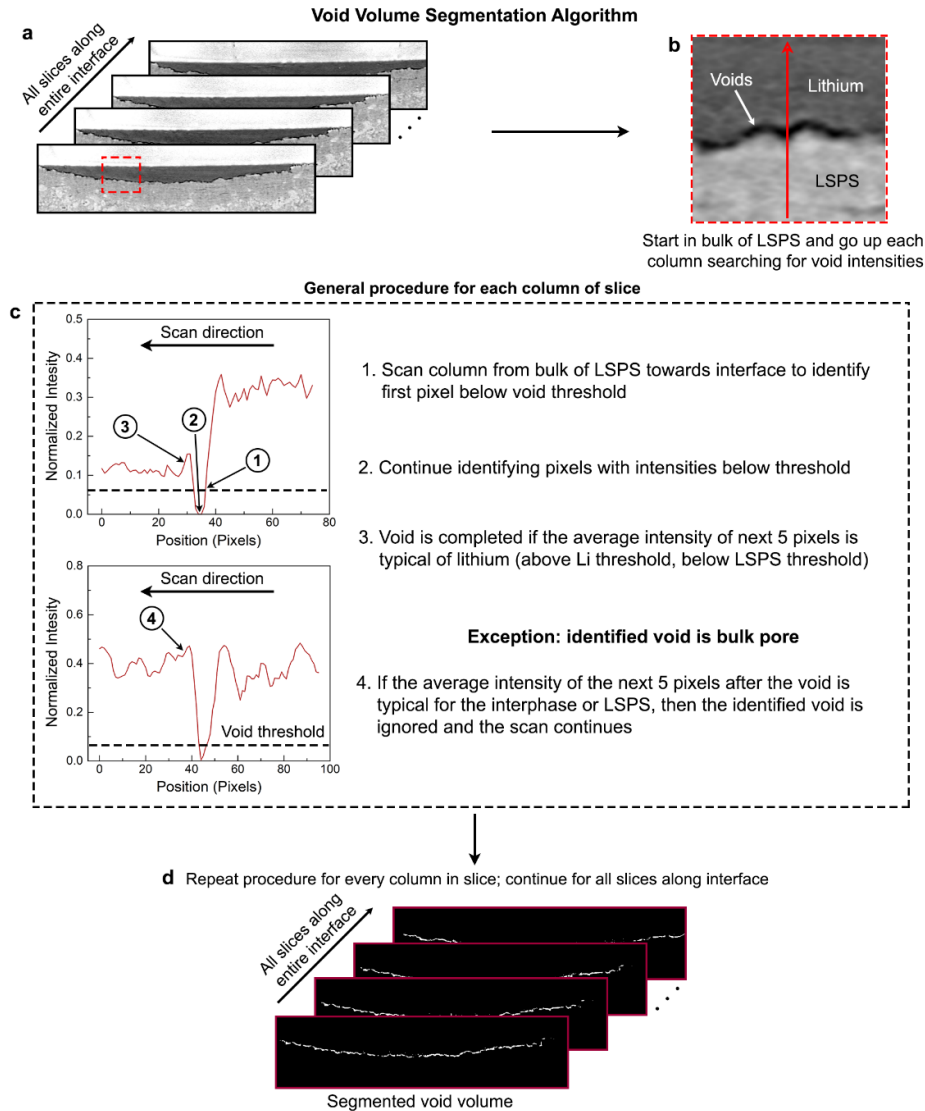


Figure 3.2. Schematic representation of the procedure used to segment interfacial void volume. **a)** Like lithium segmentation, the entire interface is segmented during this process. **b)** The algorithm starts by sequentially traversing each pixel column in a reconstructed 2D image slice. **c)** As the pixel column is scanned from the LSPS to the lithium (upwards in this case), a general procedure is applied. First, the algorithm searches for the first pixel below an intensity cutoff typical for voids (indicated by black dashed line in intensity plot in (c)). The algorithm then moves to adjacent pixels in the column and continues to identify pixels with intensities below this cutoff. If the average intensity of the next five pixels corresponds to lithium (i.e., typical of lithium intensity and below the LSPS threshold), then the void segmentation for this pixel column is completed. However, the identified region could also be a pore in the bulk of LSPS. If the average value of five pixels adjacent to the void is higher than the LSPS threshold, then this void is ignored in the analysis and the scan continues. **d)** This process is repeated for every column in the 2D image slice and then for every image slice, generating the void volume across the entire interface.

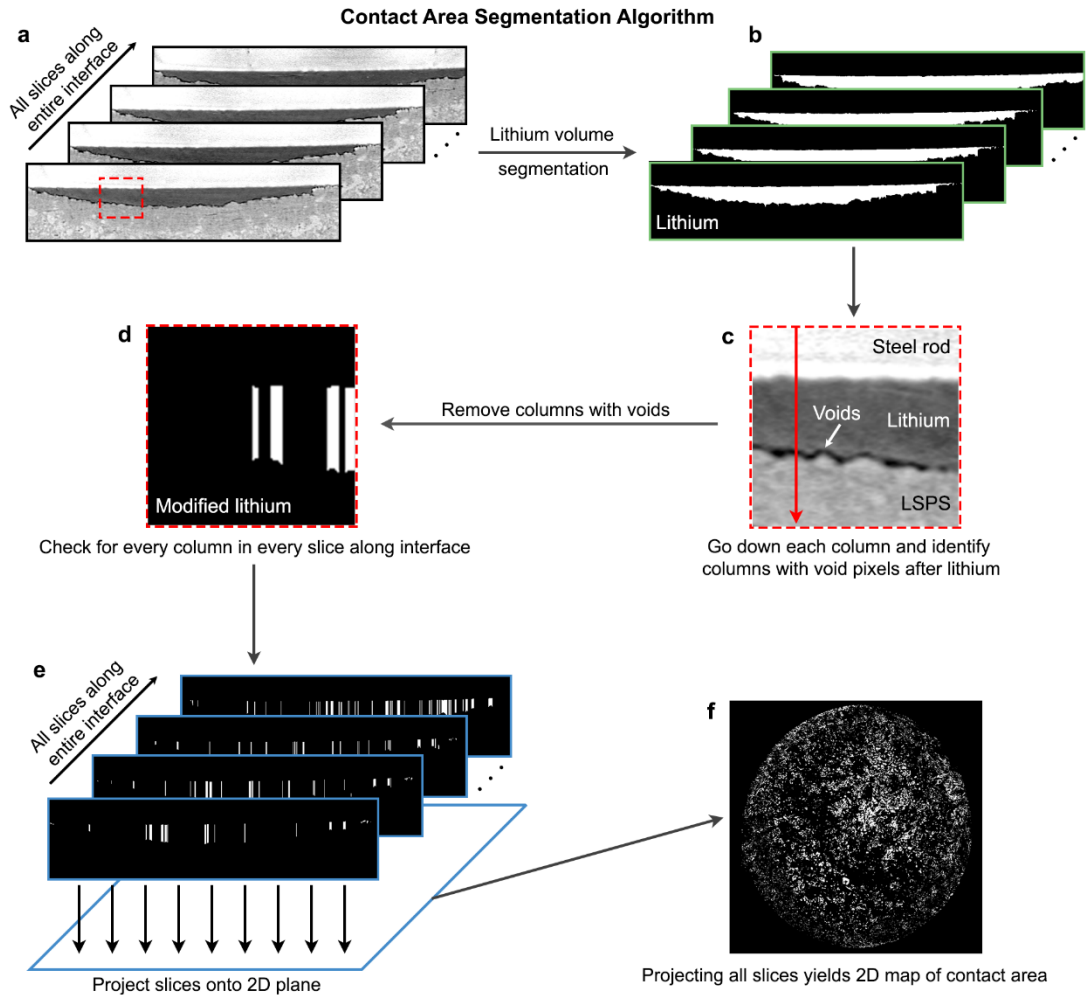


Figure 3.3. Schematic representation of the procedure developed to create 2D contact area maps for an Li/LSPS interface. **a)** This segmentation was performed on the entire interface of interest. **b)** First, the lithium volume was segmented using the same algorithm detailed in Figure 3.1. **c)** After identifying lithium, the original reconstructed image slices (shown in (a)) were scanned for interfacial voids. This was performed by traversing each pixel column (as shown in (c)) and identifying any pixels after the lithium electrode with intensity below the lithium intensity and typical void intensity. **d)** If an interfacial void was identified in a column, that column was marked as exhibiting “no contact” at that location. If no void was found, that pixel column was marked as “contacting.” The image slice was then regenerated with only the contacting pixel columns displayed. **e)** This procedure was repeated for every column in an image slice, and then applied to every slice along the Li/LSPS interface, yielding the vertical white contacting pixel columns in each slice shown. **f)** All of these modified image slices were then projected onto a 2D plane (shown in (e)) to yield the final contact area map. White pixels in (f) are pixels that lithium contacts the LSPS/interphase directly, while black pixels are pixels with no contact between lithium and LSPS.

Current density maps: The current density maps were calculated by solving equations 3.1 and 3.2 to find the current at each spot. The inputs for this calculation are the contact area maps with the location of each white pixel representing the location of individual circular contacts. The radius of each circular contact was calculated as the radius of a circle of the same area as an individual pixel. The contact area maps had to be resized and thresholded to minimize the number of equations and maximize the resemblance to the contact area maps. The contact area maps were processed and the equations solved using a python script developed by the author and available on the appendix.

3.3: Results and discussion

Figure 3.4 shows the cell design, electrochemistry and the reconstruction of a cross section of the cell at different times of the experiment. The main aspect of the cell design presented in Figure 3.4a is the selection of materials and dimensions to minimize X-ray attenuation. Figure 3.4b shows the voltage evolution over time at a nominal current density of 1 mA cm^{-2} . It can be seen that the overpotential grows very large towards the end of the second half cycle, while it barely increases during the first half cycle. In this symmetric cell configuration, the first half of the cycle corresponds to lithium stripping from the top, and the second half to stripping from the bottom interface. The reconstructions shown in 3.4 c-f correspond to the same slice in the cell, and reveal interphase growth and void formation. In those reconstructions, attenuation is proportional to brightness: voids are the darkest and pristine LSPS is the brightest. In this chapter, we will focus on the role of voids at the interface as they provide a direct observation of loss of contact area.

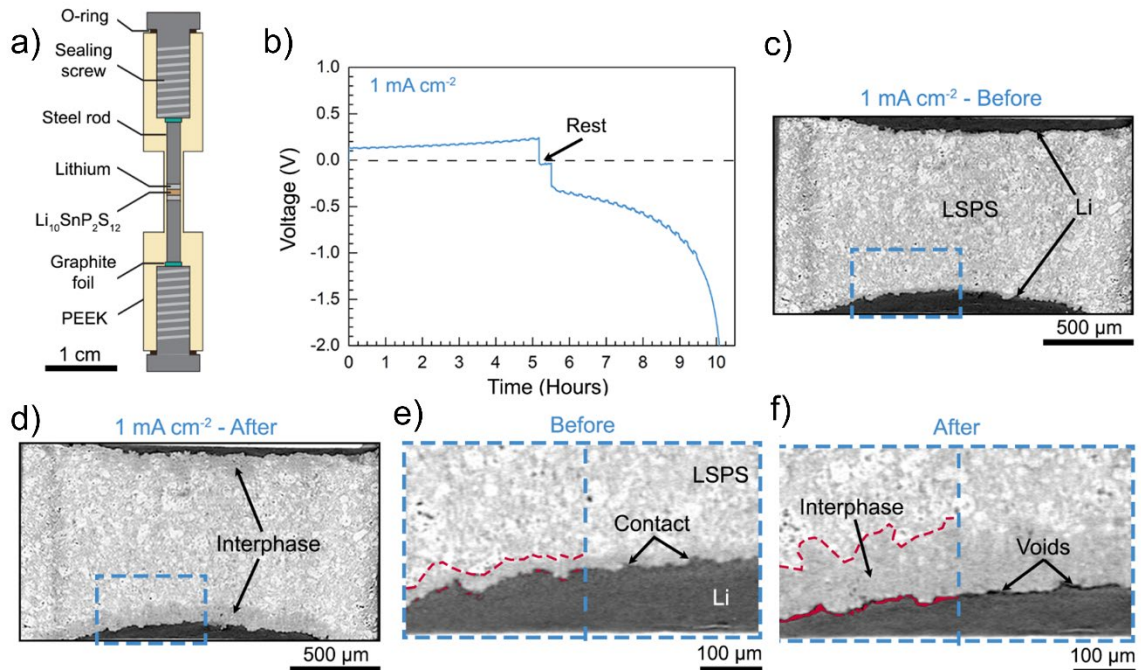


Figure 3.4. Operando X-ray imaging of symmetric cells. **a)** Schematic of the custom X-ray tomography cell used to cycle Li/LSPS/Li cells during operando experiments. **b)** Galvanostatic voltage curves measured during operando experiment at a nominal current density of 1 mA cm^{-2} , respectively. **c)** Reconstructed cross-sectional images before cycling at 1 mA cm^{-2} ; these images are extracted from the 3D tomographic datasets. The regions with dark contrast are the lithium electrodes, while the grey phase is the LSPS electrolyte. **d)** Cross-sectional image from the same location as those shown in (c) after the electrochemical cycling procedure shown in (b). **e)** Magnified cross-section of the Li/LSPS interface before cycling at 1 mA cm^{-2} , taken from the blue-boxed region in (c). Voids in the left half of the image are overlaid with red for easier visualization, and the red dashed line on the left side demarcates the interphase boundary. The right half of the image is unmarked. The formation of a darker grey interphase can be seen at the interfaces, along with morphological changes in the lithium electrodes. **f)** Magnified cross-section of the same interface as shown in (d) after one full cycle at 1 mA cm^{-2} . The volume of voids at the interface has increased significantly (overlaid with red on the left half of the image), along with growth of the interphase (demarcated by the red dashed line in the left half of the image).

In contrast to other unstable solid electrolytes, such as LAGP, failure was not associated with crack formation. Figure 3.4 shows the irregular formation of an interphase several tens of microns in thickness and no clear indication of fracture. Additionally, we observed a continuous growth of the interphase, much like in the case of LAGP, which suggests that the properties of the interphase are not directly causing the cell to fail. A comparison between Figures 3.4 e and f reveals that, besides the growth of the

interphase, there is a larger void area at the interface after lithium stripping. This suggests that loss of contact at the stripping interface might be related to cell failure rather than cracks. This phenomenon is common across all types of solid electrolytes: voids form when lithium is depleted at a faster rate than it can be replenished,⁵ which reduces the effective contact area between the lithium electrode and the solid electrolyte. In the case of unstable solid electrolytes, void formation should be exacerbated by the continuous consumption of lithium through the chemical decomposition of the solid electrolyte.

Using the segmentation algorithms described in Figures 3.1-3.3, we quantified the changes in effective contact area at the Li/LSPS interface throughout the experiment. Figure 3.5a shows the evolution of effective contact area at the top and bottom interfaces of the solid electrolyte. It can be seen that the changes in contact area at the top interface are minimal throughout the cycle. The bottom interface, in contrast, exhibits more dramatic changes in effective contact area. Interestingly, the sudden increase in overpotential during the second half of the cycle matches well with a sudden decrease in contact area at the bottom interface, the interface from which lithium was being stripped. Figure 3.5b shows an example of a contact area map constructed using the segmentation procedure described in Figure 3.3.

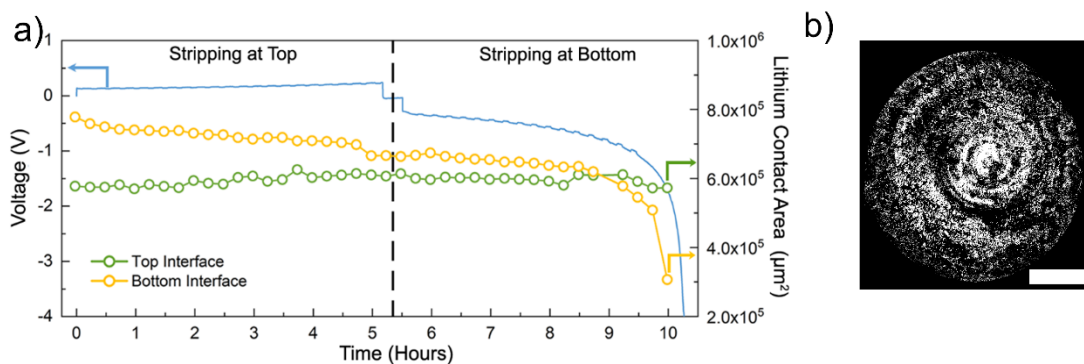


Figure 3.5. Relating interfacial contact area to cell electrochemistry. **a)** Plot of the voltage curve measured during cycling at 1 mA cm⁻² (blue line) and the corresponding lithium contact area of the top (green) and bottom (yellow) Li/LSPS interfaces in this cell. **b)** Exemplary contact area map obtained through the segmentation process where white pixels represent contact. The scale bar represents 0.5 mm.

Although the decreasing contact area is correlated to increasing current densities, any current density calculated from the total effective contact area is only an ensemble average. Implicitly, this approximation assumes that the current is homogeneously distributed across all the contact spots, i.e. the current density is the same everywhere. However, dendrites are not expected to grow everywhere. On the contrary, according to several models, current density hot-spots are precursors for dendrite growth and cell failure.^{1,2,5,10,11,24} For this reason, it is important to map the current density in each of the contact spots in order to better understand and predict cell failure.

A simple approach to map the current density is to use a well established model for constriction resistance developed by Greenwood.¹⁶ Their model calculates the potential at each contact based on the interaction of the charge passing through each contact with the charge passing through all of the other contacts. Then, since the contacts are good conductors, the condition that all the potentials must be equal is used to find the current and resistance of each contact. The method is analogous to assuming each contact as a charged circle interacting with other charged circles, each circle being a contact. The reader is encouraged to read the original paper and its appendix for a detailed derivation. With this model, the potential at the i -th contact is calculated as:

$$\Phi_i = \frac{\rho}{4} \left(\frac{I_i}{a_i} + \frac{2}{\pi} \sum_{i \neq j} \frac{I_j}{s_{ij}} \right) \quad \text{Equation 3.1}$$

Where Φ is the potential at the i -th contact, ρ is the resistivity of the high resistance member of the contact, I is the current passing through the contact, a is the spot radius, and s_{ij} is the distance between contacts i and j .

This provides a self-contained system of equations that can be solved to find the current at each spot if the potential is known. However, in the case of contact at the lithium-solid electrolyte interface, it is difficult to know that potential with precision. This is easily

overcome when the cells are operated in galvanostatic mode: the total applied current must be the summation of the current passing through each contact spot.

$$I_{Total} = \sum_i I_i \quad \text{Equation 3.2}$$

Now the current passing through each contact spot can be found solving equations 3.1 and 3.2 simultaneously.

This model was developed for the contact between two conductors, but it can be applied to the case of a lithium anode and a solid electrolyte. The first underlying assumption of the model is that current flows from one side of the contact to the other. For metals, that current flows in the form of electrons on both sides of the contact. In the case of solid state batteries, charge is transferred as electrons on the lithium side of the contact, and as lithium ions on the solid electrolyte end of the contact, hence the underlying assumption of current flow is fulfilled. The second assumption is that the electric potential will be the same for all the contacts, which is true in the case of batteries since the lithium anode is a metallic conductor, and hence the potential should be the equal at all points of its surface. Now, choosing the value of resistance to use this model in the context of unstable solid electrolytes is complex. In general, the high resistance member of the contact should be the solid electrolyte, since its ionic conductivity is orders of magnitude lower than the electrical conductivity of lithium. In the particular case of unstable solid electrolytes, this ionic conductivity should be the conductivity of the interphase, which is unknown. An unsuspected advantage of equations 3.1 and 3.2 is that the resistance term is a constant factor multiplying all the coefficients in equation 3.1, so, at a fixed total current, the currents of each spot can be calculated independently from the resistance. What will change as a function of the resistance, given a total current, is the potential. One way to think about this physically, instead of mathematically, is the following: imagine a wire of a single material and a fixed diameter and length through which a current is passed.

Now, imagine that we replace one half of the length of the wire with a material of a different resistivity but with exactly the same diameter, matching perfectly the cross sectional area of the other half of the wire. In both cases, it would be possible to apply the same current, but the voltage drop across the length of the wire will be different as a function of the resistance. With this logic, it is possible to calculate the current at each spot even without knowing the resistance of the solid electrolyte.

In the 1960s, when this model was developed, it was too expensive to solve this system of equations for a real areal contact with hundreds of contact spots. For that reason, the model was used to calculate a total contact resistance making assumptions about the average size and distribution of the contact spots.^{16,25} It is much easier to solve these equations for real systems today. The approach we take on this chapter is to treat each pixel where lithium touches the solid electrolyte as an independent circular contact spot. This is computationally simpler than modeling the charge interactions between sparse contacts of arbitrary shapes and sizes. One point of concern with this approach of assuming each pixel as an independent contact spot is that it might misrepresent what happens in contacts made of multiple continuous pixels. This concern was addressed by Greenwood on the same paper, and showed that the current passing through a closely packed cluster of circular spots arranged in a circle, is essentially the same current that would pass through a single circle of the dimensions of the cluster.¹⁶ Generalizations of Greenwood's model to other contact shapes, such as squares have also been developed and demonstrated to represent the case of arbitrary shapes modeled as sets of squared contacts.²⁶ To further validate the applicability of the model in continuous contacts, we used our model to estimate the current density distributions of electrochemical systems and geometries previously reported in the literature, as shown in Figure 3.6.

The current density maps developed with the model presented here are qualitatively and quantitatively very similar to the maps presented by Park *et al*.²⁷ The

electrodes studied by Park *et al.* are microelectrodes for neurostimulation. Geometrically, they are on a chip, on the same plane as the counter and reference electrodes.²⁷ The first aspect to note is that in all cases, the highest current densities are located at the edges of the contacts, maximizing the distance between the charges. More quantitatively, the order of magnitude of the current densities is very similar when comparing the reference from the literature and the model presented here. There are some discrepancies in the average and maximum current densities, generally overestimated by the model presented here. The origin of the discrepancies is spatial resolution. While the circle in the model has smooth edges, the one used to test the model presented here has a much smaller number of pixels and therefore serrated edges. The same is true for the fractal and the serpentine structures. These additional spikes on the serrated edges concentrate more current compared to the smooth edges.

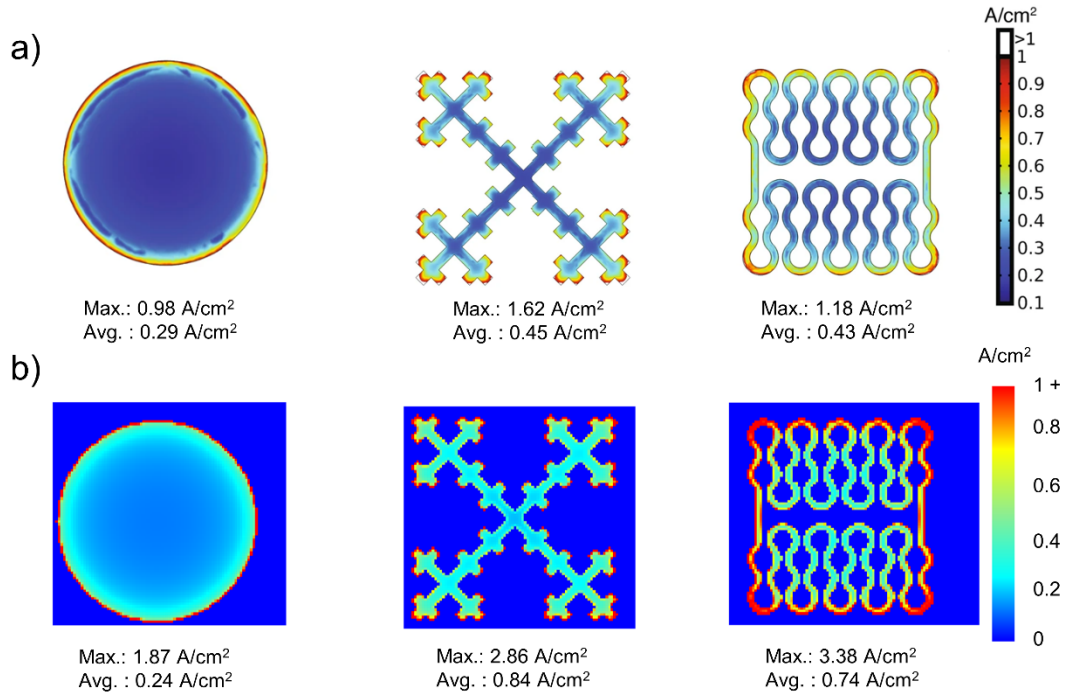


Figure 3.6. Validation of the current density model. **a)** Current density maps for various electrode contact shapes calculated using COMSOL, reproduced without modification from ²⁷. **b)** Current density maps of the same electrode contact shapes calculated with equations 3.1 and 3.2. To calculate the maps in (b), the images from (a) were binarized and scaled appropriately to reflect the same electrode dimensions. The images in (a) are

reproduced under the Creative Commons Attribution 4.0 International License: <http://creativecommons.org/licenses/by/4.0/>.

There are important differences in the way the current density maps in Figure 3.6a were constructed compared to Figure 3.6b. The maps in Figure 3.6a were obtained using finite element analysis with COMSOL to simulate non-Faradaic reactions at the interface between the electrodes of various shapes and brain tissue. In their model, they solved the charge conservation equation, and used an electrode potential and resistivity that represented experimental conditions. To construct the maps in Figure 3.6b, we used the same shapes and dimensions to build binary images where the electrode shape was represented by white pixels, and the background was represented by black pixels. Then we solved equations 3.1 and 3.2 to find the current at each white pixel using the total current calculated by the COMSOL model. To calculate the current density at each pixel, we simply divided the current at that location by the area of the pixel. For the maps in Figure 3.6b, each pixel represented approximately $1.25\text{ }\mu\text{m}$, so the circle, for example, which was $100\text{ }\mu\text{m}$ in diameter, was 80 pixels in diameter for our model. This means that the number of contact spots to solve using equations 3.1 and 3.2 was approximately 5026 to represent the area of the circle. The same number of spots would be present in the other shapes as the area is the same for all of them²⁷. Naturally, higher resolution would require more equations to be solved simultaneously, and hence more computing power.

Figure 3.7 shows the contact area maps and current density maps of the bottom interface at various times while stripping lithium from that interface (see Figures 3.4a and 3.5a). Figure 3.7a shows how the contacts become smaller over time, with a sudden reduction in size and effective contact area in the last 0.25 h of the stripping process, which is the time at which the cell fails and the experiment ends in Fig. 3.5. The modeled current density maps in Figure 3.7b reveal the non-uniform distribution of current density. In general, the highest current densities are concentrated on the smaller satellite spots

and on the edges of the larger spots. Interestingly, we observe that the edges of the larger spots recede during lithium stripping, indicating that lithium is not depleted at the same rate across the surface of the contacts. This is consistent with the higher current densities at the edges of the larger spots. The extreme case of current density concentrated on the edges of large spots and the recession of those edges is manifest in the last large spot after stripping for 10 h being situated near the center of the map.

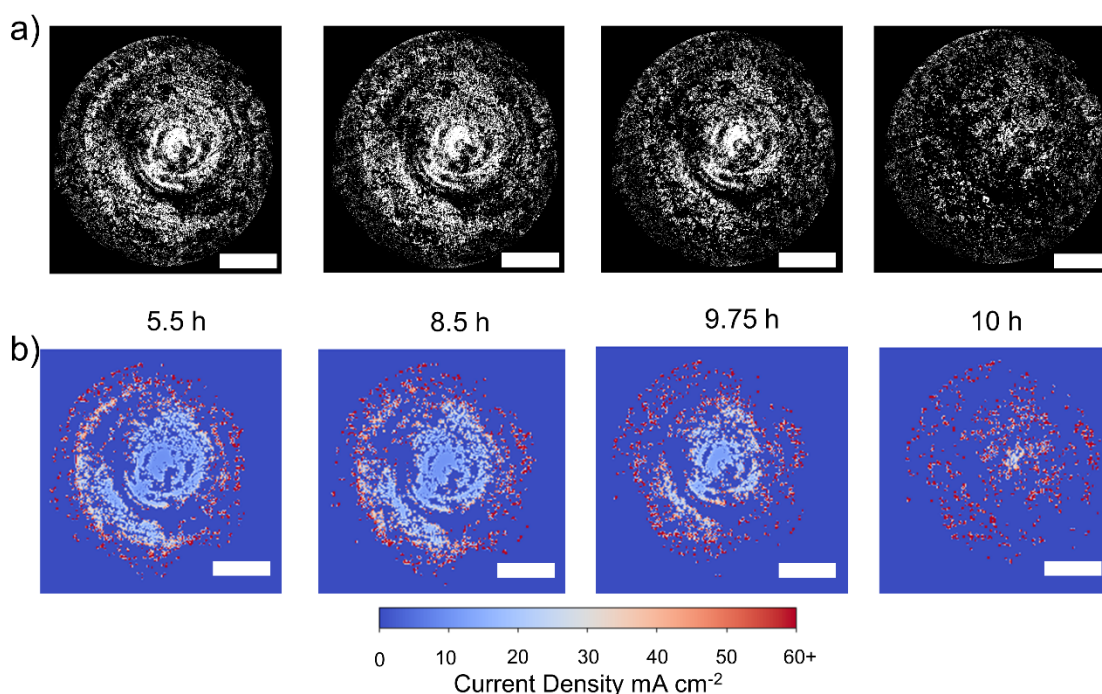


Figure 3.7. Evolution of contact area and current density at the stripping interface. **a)** Contact area maps of the bottom interface at various times of the experiment obtained through the segmentation described in figure 3.3. Each white pixel represents a point where lithium was in contact with the solid electrolyte, black pixels represent no contact. Each pixel in (a) corresponds to $1.7 \mu\text{m}$. **b)** Current density maps obtained by solving equations 3.1 and 3.2 based on the contact area maps from a. Each pixel in (b) corresponds to $8.5 \mu\text{m}$. The difference in spatial resolution arises from compressing the images in a. This compression was necessary to minimize the number of equations that needed to be solved simultaneously. The scale bars represent 0.5 mm .

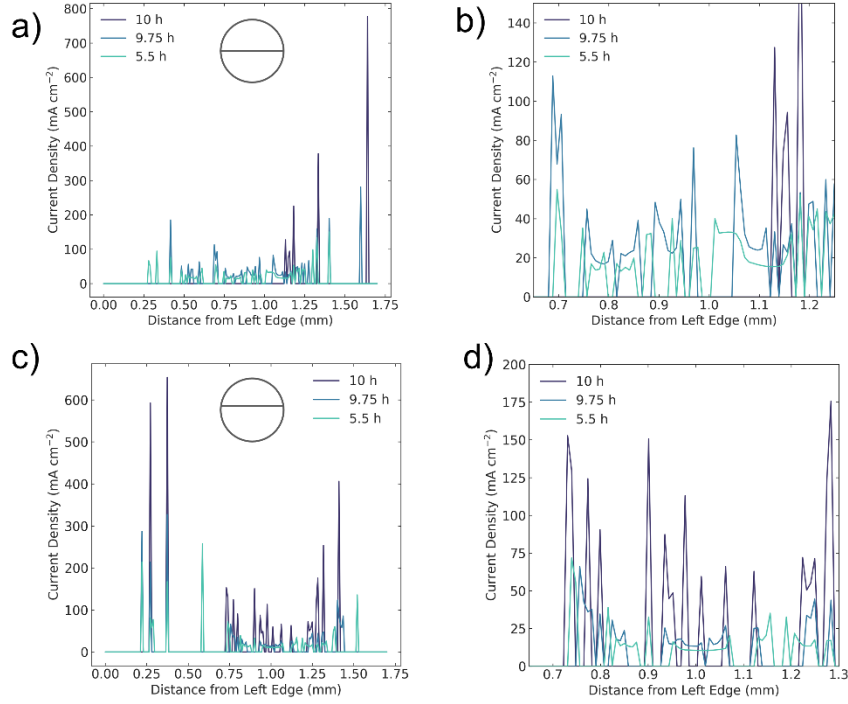


Figure 3.8. Current density line scans in different locations of the interface at various times. **a)** Current density as a function of location across the equator of the current density maps from Figure 3.7b. **b)** Inset of (a). **c)** Current density as a function of location across a different parallel on the current density maps from Figure 3.7b. **d)** Inset of (c). The lines in the circles at the top of (a) and (c) represent approximate locations of the parallels in the current density maps.

The current density line profiles in Figure 3.8 show the magnitude of current constriction. The changes in the magnitude and spatial distribution of the current density are small between 5.5 h and 9.75 h, and then the biggest change occurs between 9.75 h and 10 h. As the lateral size of the spots becomes smaller, and the spots spread out, the current density becomes higher. Notice how the magnitude of the current density reaches values higher than 800 mA cm^{-2} , which is 800 times higher than the nominal current density. Besides showing the differences in current density between different spots, the line plots in figure 3.8 highlight the differences in current density within the same spot: current density is always higher on the edges of the contact.

Figure 3.9a shows the statistical distribution of spot current density at various times. It can be seen that the changes in the shape of the distribution are small up to 9.75 h. From 5.5 h to 9.75 h, the distributions are unimodal and right-skewed, with most of the

current density values below 100 mA cm^{-2} . The distribution of the 10 h dataset is much more spread out, with a minor peak between 300 and 400 mA cm^{-2} . The area under the curves in Figure 3.9a represent the total current, since this total current is the same throughout the experiment, this is a direct comparison of how much of the total current passed at each current density at different times through the experiment. The flatter distribution at the end of the experiment indicates that a larger fraction of the current was passing at higher current densities. From this statistical information, it is also possible to extract values to represent the distribution. Figure 3.9b shows the comparison of the evolution of the median and the mean current densities over time. Not surprisingly, the overall current density, calculated as the applied current divided by the measured total effective contact area, falls between the mean and the median current densities calculated from the model. An important aspect to underline is that both the median and the mean current density calculated from the model are at least twice as high as the overall current density at 10 h. This discrepancy is explained by the fact that the model takes into account the current constriction instead of assuming a uniform distribution of the current.

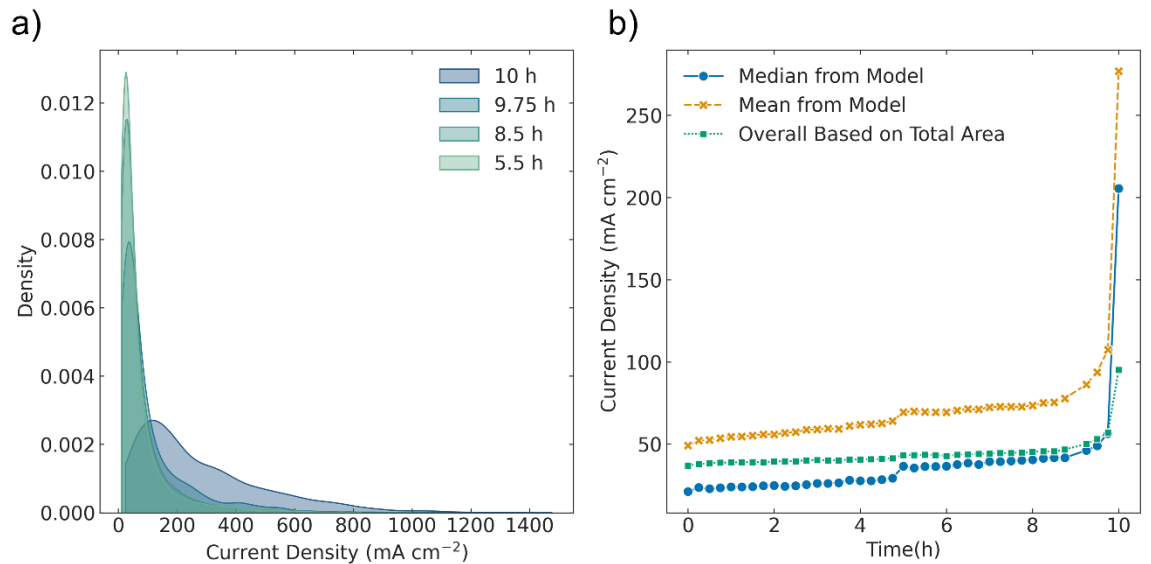


Figure 3.9. Statistical analysis of the calculated current density maps. **a)** Kernel density estimation of spot current density at various times of the experiment. The distribution is truncated at the minimum value of current density calculated. **b)** Comparison of median (blue circles) and mean (yellow crosses) current densities obtained from a throughout the

entire experiment. The green squares represent the current density calculated as the applied current divided by the effective contact area.

This study provides quantitative evidence of a broad distribution of current densities across the lithium-solid electrolyte interface. From figure 3.9, it becomes clear that it would be difficult to choose one statistical value to uniquely represent the current flow at the interface. Instead, the spatial information of current density across the interface can help identify hotspots and predict locations where dendrites are more likely to form in the case of stable solid electrolytes, for example. Additionally, it would be possible to use the current density maps to feed a more robust electrochemical model with predictive power.

3.4: Conclusions

This work reveals the dynamic evolution of contact at the lithium-solid electrolyte interface, and presents a simple model to estimate the current density at every point of the interface. We used *operando* X-ray tomography to probe the buried interface of lithium-LSPS-lithium cells. Using this technique, it was possible to directly image the evolution of interfacial voids and precisely map the contact between lithium and the solid electrolyte. We used this information to estimate the distribution of current density across the interface using a simple model for current constriction. Although the model was developed to predict the constriction resistance at the contact between electrical conductors, we demonstrate here its applicability in electrochemical systems, such as batteries, in which one side of the contact is an electrical conductor and the other side is an ionic conductor. In this simple model, each contact spot is treated analogously to a charged circle interacting with the charges of all the other contact spots. The potential at each circle is defined by its own charge and its interactions with all the other contact spots. Since the real contact spots

measured through X-ray tomography are not circles, but have arbitrary shapes, we treated each pixel from the contact area maps as an individual circular spot. The calculated current density maps reveal a broad distribution of current densities. Our model predicts higher current densities in smaller contact spots and towards the edges of larger contacts. This is in line with the general observation that the edges of larger contact spots recede as the lithium stripping proceeds, suggesting that there is a higher rate of lithium consumption at the edges of the contact spots. This strategy to estimate the current density distribution at the interface between anodes and solid electrolytes can be extended to other electrochemical systems and reveal localized phenomena such as dendrite formation in stable solid electrolytes.

3.5: References

1. Kasemchainan, J. *et al.* Critical stripping current leads to dendrite formation on plating in lithium anode solid electrolyte cells. *Nat. Mater.* **18**, 1105–1111 (2019).
2. Sun, C. *et al.* Recent advances in anodic interface engineering for solid-state lithium-metal batteries. *Mater. Horiz.* **7**, 1667–1696 (2020).
3. Wang, M. J., Choudhury, R. & Sakamoto, J. Characterizing the Li-Solid-Electrolyte Interface Dynamics as a Function of Stack Pressure and Current Density. *Joule* vol. 3 2165–2178 (2019).
4. Koshikawa, H. *et al.* Dynamic changes in charge-transfer resistance at Li metal/Li₇La₃Zr₂O₁₂ interfaces during electrochemical Li dissolution/deposition cycles. *J. Power Sources* **376**, 147–151 (2018).
5. Krauskopf, T., Hartmann, H., Zeier, W. G. & Janek, J. Toward a Fundamental Understanding of the Lithium Metal Anode in Solid-State Batteries-An Electrochemo-Mechanical Study on the Garnet-Type Solid Electrolyte LiAlLaZrO. *ACS Appl. Mater. Interfaces* **11**, 14463–14477 (2019).
6. Han, X. *et al.* Negating interfacial impedance in garnet-based solid-state Li metal batteries. *Nat. Mater.* **16**, 572–579 (2017).
7. Sharafi, A. *et al.* Surface Chemistry Mechanism of Ultra-Low Interfacial Resistance in the Solid-State Electrolyte Li₇La₃Zr₂O₁₂. *Chemistry of Materials* vol. 29 7961–7968 (2017).
8. Luo, W. *et al.* Reducing Interfacial Resistance between Garnet-Structured Solid-State

- Electrolyte and Li-Metal Anode by a Germanium Layer. *Adv. Mater.* **29**, (2017).
9. Rosero-Navarro, N. C. *et al.* Significant Reduction in the Interfacial Resistance of Garnet-Type Solid Electrolyte and Lithium Metal by a Thick Amorphous Lithium Silicate Layer. *ACS Applied Energy Materials* vol. 3 5533–5541 (2020).
 10. Sakamoto, J. More pressure needed. *Nature Energy* vol. 4 827–828 (2019).
 11. Wang, Y., Liu, T. & Kumar, J. Effect of Pressure on Lithium Metal Deposition and Stripping against Sulfide-Based Solid Electrolytes. *ACS Appl. Mater. Interfaces* **12**, 34771–34776 (2020).
 12. Ke, X., Wang, Y., Dai, L. & Yuan, C. Cell failures of all-solid-state lithium metal batteries with inorganic solid electrolytes: Lithium dendrites. *Energy Storage Materials* **33**, 309–328 (2020).
 13. Smythe, W. R. *Static and Dynamic Electricity*. (1950).
 14. Holm, R. The contact resistance. General theory. *Electric Contacts* 9–11 (1967) doi:10.1007/978-3-662-06688-1_3.
 15. Holm, R. *Electric Contacts: Theory and Application*. (Springer Science & Business Media, 2013).
 16. Greenwood, J. A. Constriction resistance and the real area of contact. *British Journal of Applied Physics* vol. 17 1621–1632 (1966).
 17. Nielsen, J. & Jørgensen, P. S. Estimation of current constriction losses via 3D tomography reconstructions in electrochemical devices: a case study of a solid oxide cell electrode/electrolyte interface. *Electrochim. Acta* **252**, 387–396 (2017).
 18. Zhang, L. *et al.* Estimation of contact resistance in proton exchange membrane fuel cells. *Journal of Power Sources* vol. 162 1165–1171 (2006).
 19. Tippens, J. *et al.* Visualizing Chemomechanical Degradation of a Solid-State Battery Electrolyte. *ACS Energy Letters* vol. 4 1475–1483 (2019).
 20. Madsen, K. E. *et al.* Direct Observation of Interfacial Mechanical Failure in Thiophosphate Solid Electrolytes with Operando X-Ray Tomography. *Advanced Materials Interfaces* vol. 7 2000751 (2020).
 21. Sun, F. *et al.* Visualizing the morphological and compositional evolution of the interface of InLi-anode|thio-LISiON electrolyte in an all-solid-state Li–S cell by in operando synchrotron X-ray tomography and energy dispersive diffraction. *J. Mater. Chem. A Mater. Energy Sustain.* **6**, 22489–22496 (2018).
 22. Shen, F., Dixit, M. B., Xiao, X. & Hatzell, K. B. Effect of Pore Connectivity on Li Dendrite Propagation within LLZO Electrolytes Observed with Synchrotron X-ray Tomography. *ACS Energy Letters* vol. 3 1056–1061 (2018).
 23. Zheng, B. *et al.* Stabilizing Li₁₀SnP₂S₁₂/Li Interface via an in Situ Formed Solid Electrolyte Interphase Layer. *ACS Applied Materials & Interfaces* vol. 10 25473–25482 (2018).

24. Lewis, J. A. *et al.* Interphase Morphology between a Solid-State Electrolyte and Lithium Controls Cell Failure. *ACS Energy Letters* vol. 4 591–599 (2019).
25. Kogut, L. & Komvopoulos, K. Electrical contact resistance theory for conductive rough surfaces. *Journal of Applied Physics* vol. 94 3153–3162 (2003).
26. Boyer, L. Contact resistance calculations: generalizations of Greenwood's formula including interface films. *IEEE Transactions on Components and Packaging Technologies* vol. 24 50–58 (2001).
27. Park, H., Takmakov, P. & Lee, H. Electrochemical Evaluations of Fractal Microelectrodes for Energy Efficient Neurostimulation. *Sci. Rep.* **8**, 4375 (2018)

CHAPTER 4: STRAIN EVOLUTION DUE TO A MOVING INTERFACE DURING LITHIATION OF ALLOYING ANODES*

4.1: Introduction

Alloying anodes, such as silicon, germanium, and tin, are leading candidates for next-generation Li-ion batteries with higher energy density.¹⁻⁴ These materials feature ~3-10 times higher theoretical specific capacity than conventional graphitic anodes; for example, Si and Ge exhibit specific capacities of 3579 mAh g⁻¹ and 1383 mAh g⁻¹, respectively, compared to graphite's 372 mAh g⁻¹. However, insertion/removal of such large quantities of lithium causes substantial volumetric expansion and contraction during cycling.¹ These transformations can cause mechanical fracture and continual exposure of new surface area, which leads to electrical disconnection, accelerated solid-electrolyte interphase (SEI) growth that irreversibly consumes lithium, and subsequent capacity decay with cycling.⁵⁻⁹ Thus, understanding and controlling volumetric and structural changes is critical for continued progress towards commercialization of these materials.

A significant body of work has been focused on understanding the transformation mechanisms in alloying anode materials,¹⁰⁻¹⁶ and the fundamental nanoscale reaction processes in Ge and Si are fairly well understood.^{1, 17-19} It is known that crystalline Ge and

*Adapted with permission from Francisco Javier Quintero Cortes, Matthew G. Boebinger, Michael Xu, Andrew Ulvestad and Matthew T. McDowell. "Operando Synchrotron Measurement of Strain Evolution in Individual Alloying Anode Particles within Lithium Batteries". ACS Energy Letters **2018** 3 (2), 349-355. <https://doi.org/10.1021/acsenergylett.7b01185> Copyright 2018 American Chemical Society.

Si react via a two-phase reaction process in which an atomic-scale reaction front separates a highly-lithiated phase and the original Ge or Si; this reaction front moves into and consumes the Ge or Si during the reaction.^{16, 19} Despite recent progress in understanding these reactions, some key aspects require more attention. In particular, the large volume changes during the reaction of Ge and Si with Li induce substantial mechanical stress within active particles,^{18, 20-23} and these stresses are known to cause fracture and to slow the reaction rate in Si nanoparticles.^{6, 24} Lithiation-induced stresses have been measured in planar thin film electrodes, and these experiments have shown that the highly lithiated Li_xSi and Li_xGe phases undergo plastic flow under biaxial compressive stresses of ~ 0.75 GPa for Li_xSi and ~ 0.5 GPa for Li_xGe .²⁰ However, the stress state within particles has been predicted to be different than thin films due to the curved reaction front, with circumferential (hoop) tension at the surface causing fracture.²⁴ A recent operando Raman spectroscopy study was the first to measure stress within active material in a particulate Si electrode,²⁵ and another study has used x-ray diffraction;²⁶ these works showed that the mean stress across many crystalline Si particles in the electrode became more compressive during lithiation. However, stress and strain have not been measured in individual alloying anode particles. While operando x-ray methods have revealed morphological changes in individual particles,^{7, 10, 27} it is critical to develop methods to obtain quantitative measurements of stress or lattice strain. This will allow the evolution of stress and strain to be related to particle size and shape in individual particles, providing important information to guide the engineering of damage-tolerant active materials.

Here, we use synchrotron operando x-ray diffraction with coherent x-rays to investigate the electrochemical reaction of individual Ge microparticles with Li. Bragg coherent diffractive imaging (BCDI) has recently been applied to battery cathode materials to reveal strain evolution and defect dynamics in real time.²⁸⁻²⁹ We use the high precision

enabled by coherent beamline 34-ID-C at the Advanced Photon Source in the present study to measure strain evolution in high capacity anode materials. The experiments herein reveal the buildup of compressive strain within the crystalline core of an individual Ge particle during discharge, and they provide the ability to track the amorphization of the particle. These results are the first to reveal crystallographic strain evolution in individual alloying particles, and this knowledge is critical both for validation of prior modeling and for designing tailored electrode materials.

4.2: Methods

Diffraction Experiments: Synchrotron x-ray measurements were performed at Sector 34-ID-C at the Advanced Photon Source at Argonne National Laboratory. The experimental geometry is shown in Fig. 1 . An incident beam of coherent x-rays with an energy of 8.919 keV and 1 eV bandwidth was focused down to an area of $5 \times 20 \mu\text{m}^2$ (vertical by horizontal) and aimed to illuminate the battery coin cell. The beam passed through a kapton-covered hole in the stainless-steel case of the coin cell to minimize attenuation. The battery was oriented so that the beam went through the lithium electrode and the separator before reaching the germanium electrode. The detector (Medipix2/Timepix, 256x256 pixels, each pixel $55 \mu\text{m} \times 55 \mu\text{m}$) was placed at a distance of 2.0 m from the sample and a scattering angle of 24.3455° , corresponding to the (111) Bragg peak of crystalline Ge.

Three different types of x-ray measurement scans were performed. In the first type, the position of the detector was fixed, and the battery was translated horizontally and vertically perpendicular to the beam direction with micrometer-range steps so that the beam illuminated a total area of 2 mm^2 during all the steps. The purpose of these scans was to locate particles within the electrode that were oriented so that diffracted x-rays from

these particles were detected at the detector. These scans normally took ~6 h and generally less than 5 appropriately-oriented particles were found across the total scanned area; the position of the stage during these detection events was recorded. The second type of scan consisted of collecting rocking curves around the Bragg peak. For each rocking curve scan, the battery was rotated in 42 steps through the angle ω (see Fig. 1a). An image of the diffracted intensity was collected at each step with an exposure time of 1.0 s. This procedure provides a 3D view of the diffraction point in reciprocal space, and these scans were analyzed to determine diffracted intensity and the evolution of d-spacing during the experiments. It was observed that the particles either rotated or moved within the electrode during the reaction, so a third type of scan was used to track the particles while the battery stage and the detector were moved accordingly to ensure that the diffracted beam was aligned with the detector. These tracking scans were rocking curves with 16 steps and 0.1 s exposure times.

One particle was selected for observation within each of the batteries tested, and discharge at a rate of C/9 was initiated along with a series of tracking scans. Tracking scans were continuously collected during discharge to maintain the Bragg condition. For collection of detailed rocking curves, the current was first paused and the battery was allowed to rest for 5-10 min, and then between 3 and 6 detailed rocking curves were collected. This rest period allowed for stabilization of subtle particle movements.

Data Analysis: Calculation of d-spacing: Each rocking curve consisted of 42 image files at different values of sample rotation (ω in experimental coordinates). Each pixel in these images was summed with the corresponding pixels at the same location in all the other images, resulting in an integrated image. This image was then averaged with the data processed in the same manner from the other rocking curves at each point during discharge. An effective 2θ value was then calculated for each pixel based on its position

in reciprocal space. The resulting data were integrated over 2θ intervals which were the size of the angular resolution of the detector (0.0014°). Instrumental resolution was calculated as the difference in the angles measured at two adjacent pixels sharing an edge on the detector given the pixel size and the distance from the sample to the detector. The reported d-spacing was calculated using the 2θ interval with the highest intensity.

Calculation of integrated diffracted intensity: The reported integrated intensity corresponds to the summation of the intensity of all the pixels in each averaged image from the rocking curve scans.

Error bars in both cases are the confidence interval obtained considering between 3 and 6 rocking curve scans for each data point using a Student's t-distribution with $\alpha=0.05$. The instrumental resolution was used for d-spacing error bars whenever the instrumental resolution was larger than the calculated confidence interval.

Extent of reaction of a single particle: The evolution of d-spacing can also be analyzed as it relates to the extent of reaction of the single particle. For this purpose, we will define the extent of reaction as the volume fraction of the initial crystalline Ge that has reacted:

$$\xi(t) = \frac{v_0 - v(t)}{v_0} \quad (1)$$

Here, V_0 is the initial volume of the crystalline particle, and $V(t)$ is the volume of the remaining crystalline Ge portion. It can be seen that this parameter goes from 0 to 1 from the beginning of the reaction to the end.

Volumetric data is not immediately available from the experiments, but it can be assumed that given the size of the particles, volume is directly proportional to the integrated intensity (as discussed later). With this consideration, the extent of reaction can be expressed in the same form as Equation (1), using integrated intensity instead of volume. This analysis is presented in Figure 4.7a. The x-axis error bars in this figure were

calculated by using the spread of integrated intensity shown in Figure 4.4a. For comparison, the predicted evolution of d-spacing vs. extent of reaction according to the spherical single-particle model is presented in Figure 4.7b.

Electrochemistry: As shown in Fig. 1a, the experiments involved illuminating a battery coin cell with a coherent x-ray beam with energy of 8.919 keV and detecting the x-rays that were diffracted from a single active material particle within the working electrode. The coin cells had Kapton windows to facilitate x-ray transmission,²⁹ and the cells featured a Ge working electrode (Sigma-Aldrich, 99.999%, 100 mesh) with $\sim 2.1 \text{ mg/cm}^2$ mass loading spread on expanded copper foil mesh (Dexmet Corp.), along with a Li metal foil counter/reference electrode (Sigma-Aldrich, 99.9%). The electrolyte was a 1:1 mixture of ethylene carbonate (EC) and dimethyl carbonate (DMC) with 1.0 M LiPF_6 salt (Sigma-Aldrich). A two-dimensional photon-counting x-ray detector (Medipix 2) was positioned 2.0 m downstream from the coin cell at a position on the $\{111\}$ Debye-Scherrer ring of Ge ($Q = 1.923 \text{ \AA}^{-1}$). The incoming x-ray beam, which had a size of 4 mm by 4 mm, was then rastered across the sample until a diffracted beam from a single particle was detected at the detector location. Diffraction from single particles was assured due to their random orientations; only 3-5 particles with appropriate orientation for diffraction onto the detector were found across $\sim 2 \text{ mm}^2$ area in a typical experiment. After selecting an appropriate particle, the x-ray beam was positioned on that particle, and diffraction was continuously monitored during galvanostatic discharge of the battery cell at current rates of C/9 (corresponding to full discharge of the theoretical capacity of the working electrode in 9 hours). Figure 4.1b shows a typical discharge curve of a half cell during an operando experiment; the Ge electrodes in these experiments consistently showed near-theoretical capacity when discharged at these rates. During discharge, rotations and/or lateral translations of the particle were corrected for by rotating/translating the cell to maintain the

diffraction condition. Possible particle translations in the direction of the beam were calculated to have negligible effect on the position of the peak.

Three-dimensional diffraction intensity distributions in reciprocal space were collected by rotating the sample through a small angle (0.2° through the angle ω in Fig. 1a) and recording the 2D diffracted slice at each angle (this is known as a “rocking curve”). Two types of such scans were used: one with shorter exposure times and fewer rotation steps (~ 16) to track the reacting particle, and a longer scan with more steps (~ 42) for detailed analysis during pauses in the discharge current.

4.3: Results and Discussion

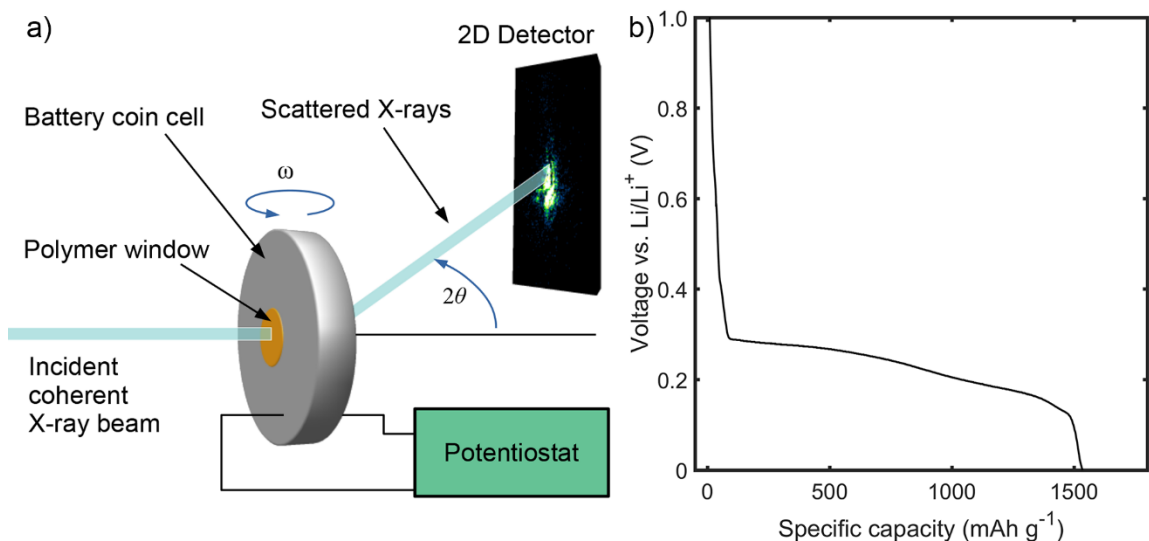


Figure 4.1. Experimental setup. **a)** The incident x-ray beam illuminates the electrode through a window inside the battery. The diffracted beam is transmitted through the remainder of the cell and collected at a 2D detector positioned at the Debye-Scherrer ring for Ge {111}. To collect the three-dimensional shape of the diffraction intensity in reciprocal space, the battery was rotated 0.2° along ω . **b)** Typical galvanostatic discharge curve for a Ge working electrode in the *operando* half cell. This cell was discharged at a rate of C/9. The measured specific capacity was slightly larger than theoretical, which is likely due to solid-electrolyte interphase growth.

Figure 4.2 displays diffraction data from an *operando* experiment. Figure 4.2a shows rocking curve data revealing the 3D shape evolution of the diffraction intensity.

The 3D diffraction data shown in Figure 4.2a were taken at different times during discharge, and it is evident that both the position and the shape of the diffraction intensity changed during discharge. Importantly, the position of the diffraction intensity moved perpendicular to the Debye-Scherrer ring (shown in gray), indicating a change in interplanar spacing. Motion along the ring corresponds to particle rotation. Furthermore, the diffraction point broadened and decreased in intensity as lithiation proceeded, corresponding to a decrease in the amount of crystalline Ge during the reaction. Figure 4.2b displays the diffraction data visualized in a different way; here, the diffracted intensity is projected onto the detector plane and shown as a line plot. The x-axis in Figure 4.2b thus represents the magnitude of the scattering vector Q . In this plot, the diffraction peaks are observed to diminish in intensity and broaden with increasing extent of lithiation. Simultaneously, the center of the peak shifts to higher scattering vector values, indicating a change in lattice spacing.

Ideally, coherent diffraction can be used to provide real-space images of Bragg electron density and strain within materials via the use of phase retrieval algorithms that rely on oversampling of the diffraction pattern produced by diffracted coherent x-rays.³⁰⁻³³ Such techniques have previously been used to image battery cathode materials,²⁹ as well as other nanoscale materials and thin films.³⁴⁻³⁵ Unfortunately, our experiments struggled to sufficiently oversample the data due to the large particle size of a few microns. Instead of using real-space reconstructions, we focus on structure and strain evolution determined from the position and intensity of diffracted x-rays; future research will focus on optimizing conditions to obtain data for which phase information can also be calculated.

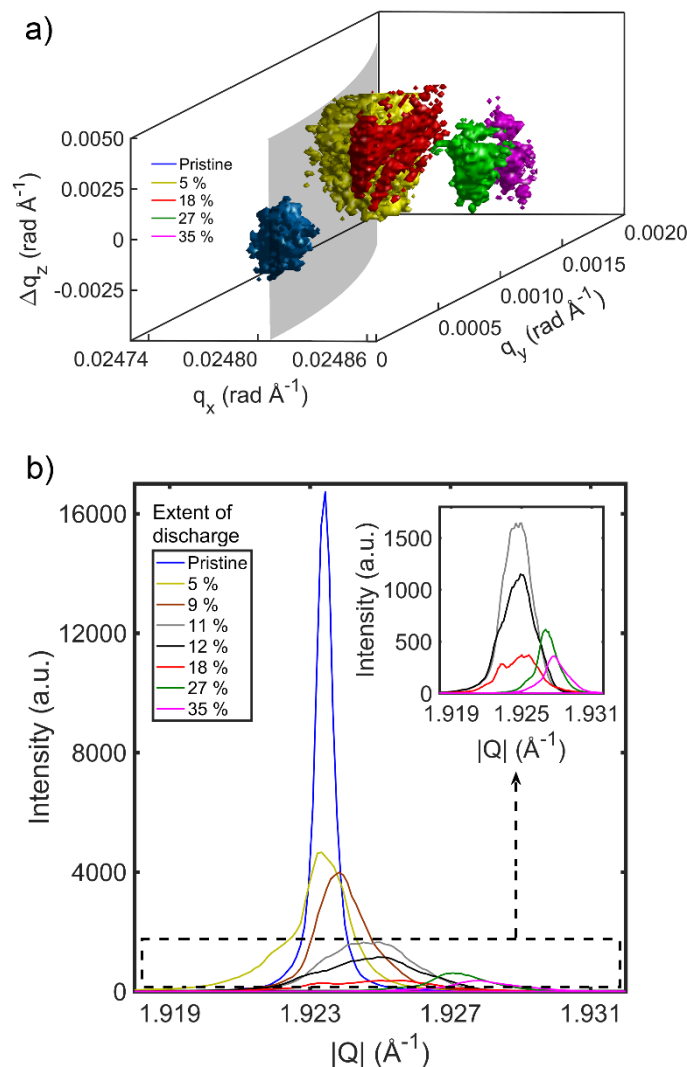


Figure 4.2 Evolution of the diffracted intensity from the (111) planes of a single Ge particle during lithiation. **a)** 3D representation of the diffraction intensity in reciprocal space at different times during lithiation. The z-axis in this figure corresponds to the experimental rotation of the particle around angle ω (see Fig. 1a). The x- and y-axes are converted from the pixels on the detector. The gray surface represents constant Q , and the legend shows the extent of discharge. **b)** This plot shows representations of the diffraction peaks calculated by integrating over all separate 2D slices collected during a single rocking curve measurement. In other words, these peaks are the diffracted intensity projected along the z-axis in (a). The inset shows magnified peaks during the later stages of lithiation for which the diffracted intensity is lower.

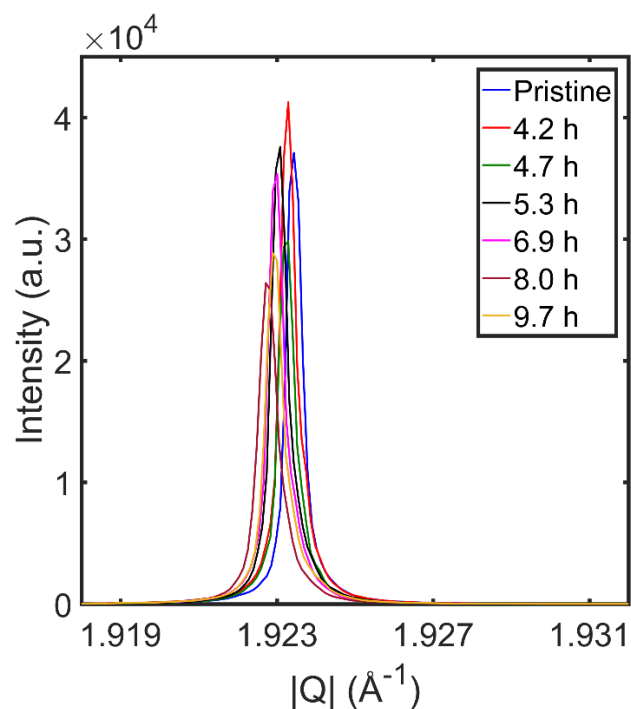


Figure 4.3. Diffraction peaks calculated by integrating over all separate 2D slices collected during a single rocking curve measurement, as in Figure 4.2b. These data are from the non-reacting particle shown in Figure 4.5, and the legend refers to the time during discharge. The magnitude of the scattering vector is presented over the same range as shown in Figure 4.2b for comparison.

Table 4.1. Full-width-half-maximum (FWHM) of the peaks shown in Figure 4.3.

Time (h)	FWHM (\AA^{-1})
0	3.48×10^{-4}
4.2	3.44×10^{-4}
4.7	3.44×10^{-4}
5.3	3.45×10^{-4}
6.9	3.47×10^{-4}
8.0	3.44×10^{-4}
9.7	3.35×10^{-4}

Figure 4.4a shows the integrated diffracted intensity (i.e., peak area) from this same particle overlaid on the galvanostatic discharge curve for this battery cell. These values were calculated by averaging the integrated intensity of several rocking curves taken sequentially after pausing the cell current. Integrated intensity is proportional to the volume of the material when attenuation is negligible, which is the case when Ge is thin ($<40\text{ }\mu\text{m}$ for $\sim 9\text{ keV}$ incident x-rays³⁶). As shown in Figure 4.4a, the integrated diffracted intensity steadily decreased during discharge until a specific capacity of $\sim 200\text{ mAh g}^{-1}$ had been reached. After this, the decrease in integrated intensity slowed until a capacity of $\sim 550\text{ mAh g}^{-1}$ had been reached, when the (111) diffraction from the particle disappeared. This indicates that the crystalline Ge (c-Ge) had been completely consumed by the electrochemical reaction. From previous work, it is known that c-Ge is first converted to an amorphous Li_xGe phase (where $x = 2.25$) via a reaction in which the two phases are separated by a sharp reaction front. Near the end of discharge, this heterogeneous amorphous phase and other amorphous Ge phases crystallize into the $\text{Li}_{15}\text{Ge}_4$ structure.^{10-11, 17, 19} This is similar to the phase evolution when crystalline Si reacts with Li.^{1, 37} Previous ensemble in situ x-ray diffraction (XRD) on Ge microparticle electrodes showed that the crystalline Ge phase disappeared after reaching $\sim 60\%$ of the maximum theoretical discharge capacity.¹¹ The crystalline Ge phase in the particle in our experiment disappeared after $\sim 40\text{-}45\%$ of the maximum theoretical capacity had been reached, which illustrates that some individual particles behave differently than the ensemble. Reaction of individual alloying anode particles at different times, and therefore different electrochemical potentials, may be expected for particles of different shapes, sizes, and extent of mechanical confinement within the electrode architecture. This is because these variations could lead to different mechanical stresses and therefore varying local electrochemical potentials, as recently demonstrated for Si electrodes.³⁸⁻³⁹

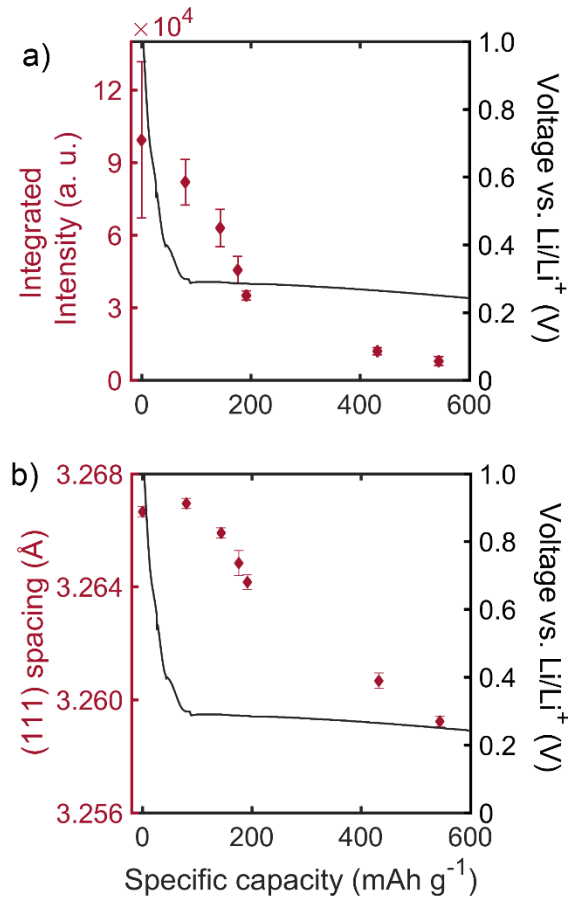


Figure 4.4. Changes in intensity and (111) planar spacing overlaid with electrochemistry. **a)** Evolution of the integrated diffracted intensity from an individual Ge particle during discharge (left axis); these data are superimposed on the galvanostatic electrochemical curve (right axis). **b)** Evolution of the (111) planar spacing during discharge for the same particle, along with the same electrochemical data. Error bars correspond to the confidence interval ($\alpha = 0.05$) from multiple sequential measurements when paused at the same specific capacity. In some cases in (b), the confidence interval was smaller than the instrument resolution (*i.e.*, the angular span of a single pixel at the detector distance), so the latter is presented instead. These error bars were chosen instead of using the full-width-half-maximum (FWHM) of the peaks as error bars in (a) since the FWHM convolves multiple factors (*e.g.*, strain gradients, particle size) that do not directly impact precision.

The two-phase alloying reaction in which the c-Ge was converted into Li_xGe did not start until the plateau at 300 mV vs. Li/Li⁺ was reached in the galvanostatic curve in Figure 4.4a. This relatively flat plateau signifies a two-phase reaction according to Gibb's phase rule, as has been shown for the c-Ge to Li_xGe transformation.^{10, 19} The discharge capacity observed before this potential was reached arose due to contributions from solid-

electrolyte interphase (SEI) formation and electrochemical reaction of GeO_x surface oxides, as commonly observed in many alloying anode materials.⁴⁰ In addition, it is possible that the intercalation of small amounts of Li^+ occurred during this pre-plateau region. This has been suggested to cause a decrease in diffracted intensity in a prior study,¹¹ but a definitive decrease in diffracted intensity before the plateau was not observed here. In addition to the diffracted intensity analysis, an estimate for the initial particle size can be obtained by applying a Fourier transform to the initial diffraction data. For the particle analyzed here, the initial size was estimated to be about 2 μm .

From the diffraction data, the planar spacing of the individual c-Ge particle can be calculated using Bragg's Law from the position of the diffraction point in reciprocal space. Figure 4.4b shows the (111) spacing for the c-Ge particle from Figure 4.4a as a function of discharge capacity. The planar spacing was fairly constant until the plateau at 300 mV vs. Li/Li^+ was reached, and then the (111) spacing steadily decreased until the crystalline phase was no longer detectable at $\sim 550\text{-}600 \text{ mAh g}^{-1}$ capacity. The planar spacing decreased from an initial value of 3.266 Å to a value of 3.259 Å at the end of lithiation. This represents a direct measure of the average strain in the crystal along the [111] crystallographic direction, and these measurements show that the crystal experiences an average of 0.21% compressive strain along this direction. For comparison, Figure 4.5 shows data from another particle from a separate experiment; this particle did not undergo electrochemical reaction during discharge, which could be because it was not well-connected to the electrode architecture. The diffracted intensity fluctuated during the experiment due to particle movement and/or rotation (Figure 4.5a), but it was virtually the same at the beginning and the end, indicating that the Ge crystal did not decrease in size. Accordingly, the measured (111) lattice spacing was also constant (Figure 4.5b). This comparison gives further evidence that the steady decrease of diffracted intensity and lattice spacing shown in Figure 4.4 are due to the electrochemical reaction.

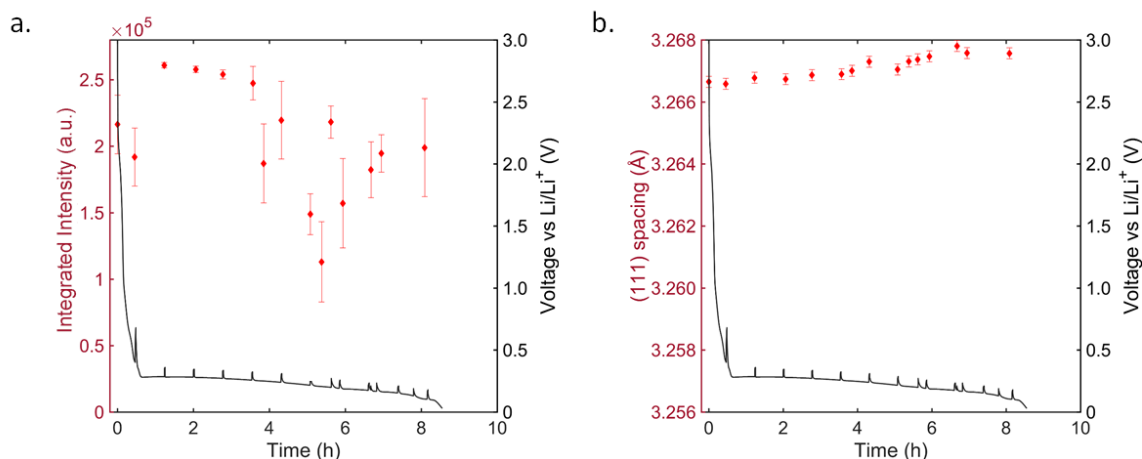


Figure 4.5. Integrated diffracted intensity and d -spacing from a non-reacting particle. **a)** The integrated intensity did not change significantly from the beginning to the end of the reaction. The intensity fluctuations during the reaction are explained by movement of the particle. **b)** d -spacing is plotted within the same range as shown in Figure 4.4b. It can be seen that the changes in d -spacing are negligible compared to the changes observed for the reacting particle displayed. The spikes in the voltage curve arise because the current was decreased to C/100 to take detailed rocking curves.

The stress state within spherical particles and other structures during this two-phase lithiation process has been modeled with analytical and computational methods in previous work.²³⁻²⁴ The large lithiation-induced volume expansion causes significant compressive stress in the lithiated shell near the two-phase interface.²⁴ Circumferential (hoop) tension exists at the surface of such particles, which is consistent with prior reports of fracture initiating at the surface of lithiated Si and Ge.^{8, 18, 41} The substantial compression within the lithiated shell has been predicted to induce compressive stress within the crystalline core; for a spherical nanoparticle with an infinitesimally thin reaction front region, such stresses have theoretically been predicted to be hydrostatic.^{6, 24}

Our experiments provide a precise measurement of the strain along the [111] direction in a Ge particle during lithiation. Since only one diffraction point from a given particle is able to be tracked during discharge in these experiments, the strain along other directions (and thus the full strain tensor) was not measured in this study. If we assume that the crystalline Ge core experiences purely hydrostatic stress, our measured strain

would correspond to a pressure of 490 MPa within the crystalline core (given a bulk modulus of 77.2 GPa for Ge⁴²). On the other hand, if we assume uniaxial strain along the [111] direction (a limiting case), the measured strain would correspond to a uniaxial stress of 220 MPa within the core (given a Young's modulus of 102.7 GPa for Ge⁴³). The stress within the crystalline core is likely not purely hydrostatic because the Ge crystals are not perfect spheres in these experiments; asymmetric lithiation and morphological changes may introduce a deviatoric component. However, the range of stresses within the Ge particle found here is similar to previous ensemble measurements of stress in Si nanoparticles using Raman spectroscopy that found maximum pressure values of 300 MPa.²⁵ Even though these particles were smaller, prior modeling has shown that the evolved stress during this two-phase large-volume-change reaction should be independent of particle size, assuming fracture does not occur and that particle size does not approach the width of the reaction front (~1-2 nm length scale). Thus, due to their similar reaction mechanisms, it is expected that both c-Ge and c-Si should exhibit similar stress states and magnitudes even when comparing nanoparticles and the larger particles studied here. This similarity, in addition to the likelihood that the particle investigated here did not fracture during lithiation (as indicated by the relative stability of the position of the diffraction point), suggests that the stress state in the crystalline Ge core of this particle was closer to hydrostatic than uniaxial.

To analyze these results in greater detail, we build on a previously developed analytical model²⁴ for stress evolution during the two-phase reaction of large-volume-change battery materials. This model was developed for lithiation of c-Si, but it should also describe the lithiation of c-Ge due to the similar two-phase mechanism involved. Figure 4.6a shows a schematic of the two-phase expansion of a spherical particle with initial radius of B . After partial reaction, the radius of the crystalline core decreases to A , while the outer radius increases to b (Figure 4.6b). The ratio of the volume of the expanded shell

to the original volume of the reacted crystalline region is given by , where W is the molar volume of the two species. As shown by K. Zhao et al.,²⁴ the outer radius b of the sphere depends on the radius A of the crystalline core in the following manner:

$$b(t) = [A(t)^3 + \beta(B^3 - A(t)^3)]^{1/3} \quad (2)$$

From this equation and the deformation of a given volumetric element at radius R within the sphere, the radial stress and hoop stress can be derived at all points in the sphere as a function of the extent of lithiation, as shown by K. Zhao et al.²⁴ This derivation neglects elastic strain and assumes that the original material is rigid and the lithiated material is rigid-plastic, which is a reasonable assumption since the lithiation-induced strains (200-300%) are much larger than elastic strains. This derivation finds that hydrostatic stress evolves within the shrinking crystalline core according to the following equation:

$$\sigma_h = -2 \sigma_y \ln (b/A) \quad (3)$$

In equation (3), σ_h is the hydrostatic stress in the core, σ_y is the yield stress of the lithiated material, and the radius ratio b/A reflects the extent of lithiation. The compressive flow stress for $\text{Li}_{2.25}\text{Ge}$ has been measured to be ~ 450 MPa.^{20, 22} Using this value for the yield stress, Equation (3) is plotted in Figure 4.6c. This simplified model predicts increasing pressure in the crystalline core as the extent of lithiation increases; at large b/A values (i.e., small crystalline core), the pressure is quite large (\sim GPa level).

This derivation predicts stress as a function of the extent of lithiation, but it does not predict the time dependence of stress evolution in galvanostatic experiments like those reported here. Thus, we extend this model to predict stress as a function of time for the lithiation of a spherical particle at a constant lithiation rate, where the rate of reduction of the volume V of the crystalline core due to reaction is given by

$$\frac{dV}{dt} = k \quad (4)$$

where k is constant. The infinitesimal change in volume due to lithiation is given by

$$dV = -4 \pi A^2 dA \quad (5)$$

Combining equations (4) and (5) gives the rate of change of the core radius A with time (dA/dt), and integration and combination with equation (2) provides the core radius A and outer radius b with time:

$$A(t) = \left[\frac{-3k}{4\pi} t + B^3 \right]^{1/3} \quad (6)$$

$$b(t) = \left[(\beta - 1) \frac{3k}{4\pi} t + B^3 \right]^{1/3} \quad (7)$$

Using appropriate values of b , k , and B , these equations for $A(t)$ and $b(t)$ can be inserted into Equation (3) to calculate the pressure within the core as a function of time given the assumption of constant lithiation rate (i.e., constant volumetric consumption). The predicted pressure in the crystalline core as a function of time is shown in Figure 4.6d for the lithiation of a spherical crystal. The rate of reaction is set so that consumption of the crystal occurs in ~5 hours, which approximately corresponds to the experimental observations herein. The volume expansion ratio b was chosen to be 3.0 based on prior experiments.¹⁸⁻¹⁹ This model shows that the hydrostatic stress within the crystalline core is expected to decrease (i.e., increased pressure) in a fairly linear manner with time over most of the lithiation process. During the last ~20% of the lithiation process, the pressure increase accelerates due to rapid shrinkage of the small remaining crystal. Figure 4.6e shows the predicted evolution of planar spacing within the Ge crystal as a function of time given these hydrostatic stresses. Our experimental data are remarkably consistent with the prediction of a close-to-linear change in d -spacing over most of the lithiation time, as shown in Figure 4.4b. The effects of the rapid pressure increase and large pressures predicted at the end of lithiation are likely difficult to detect in our experiments, because they occur when the crystalline core is < ~5-10% of its original volume, meaning that x-ray scattering from this volume would be significantly reduced. The measured strain and

calculated maximum pressure value (490 MPa) from experiment are within the range of that predicted from this model at intermediate extents of lithiation. Overall, the good agreement between our results and this model, in addition to agreement with prior experimental results on ensemble electrodes,²⁵ affirm the accuracy of these measurements. We note that when the experimentally measured and predicted d-spacing values are plotted against the extent of reaction of this single particle (as estimated from the integrated diffracted intensity), a similar trend is observed (see Figure 4.7).

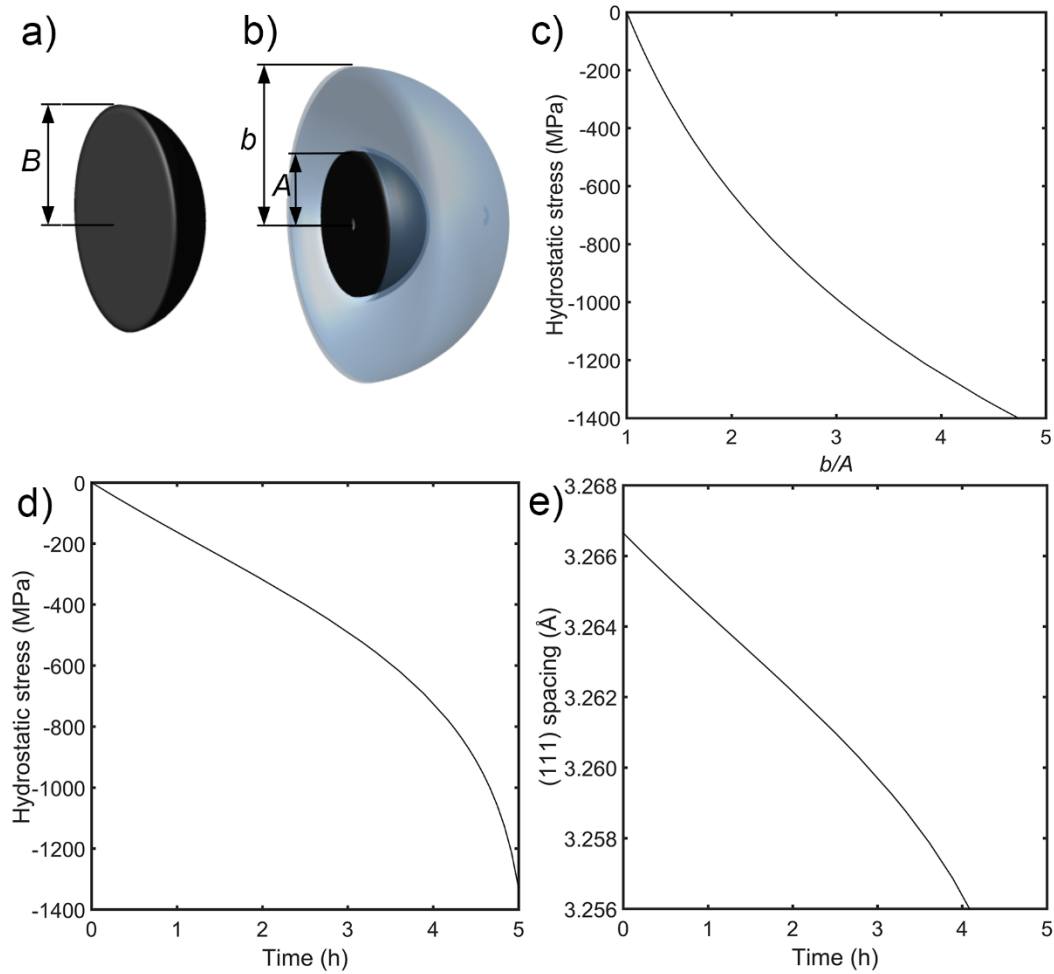


Figure 4.6. Analytical model for stress and strain evolution within a crystalline Ge particle during electrochemical reaction. **a-b)** Schematics of the evolution of a spherical particle during lithiation. The initial particle with radius B in (a) is transformed to a core-shell structure in (b) with internal Ge radius A and external radius b . **c)** Predicted evolution of hydrostatic stress within the Ge core as a function of extent of reaction (b/A). **d)** Predicted evolution of hydrostatic stress within the Ge core as a function of time. **e)**

Predicted evolution of (111) planar spacing within the crystalline Ge as a function of time based on the hydrostatic stress in (d). The calculations in (c)-(e) were performed for a 2 μm particle that was consumed in ~ 5 hours.

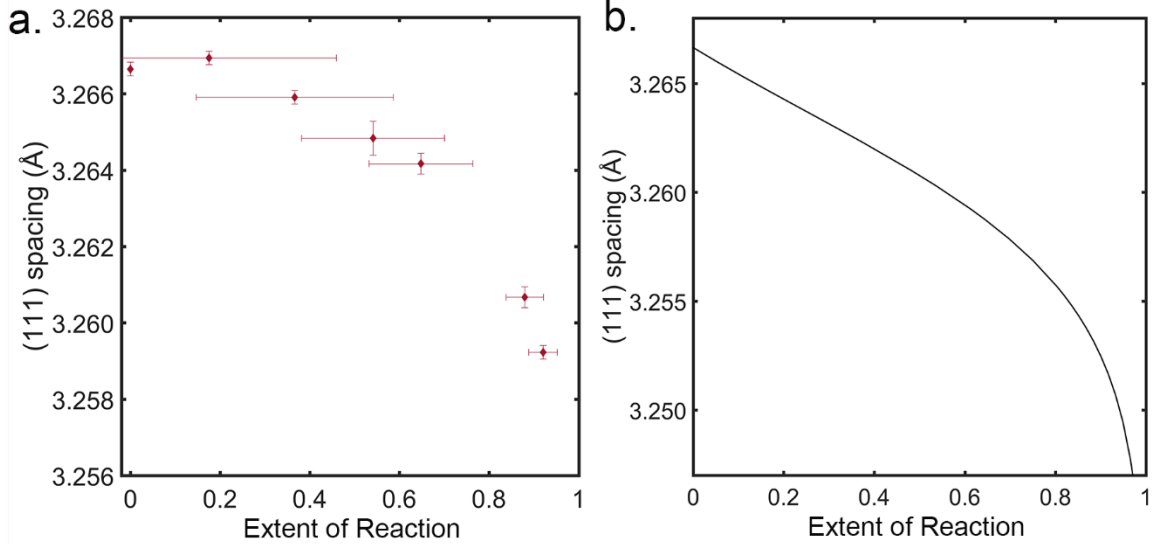


Figure 4.7. Evolution of d-spacing as a function of the extent of reaction for a single particle. The extent of reaction is represented by the fractional change in volume of the crystalline Ge particle according to Equation (1). This is a different way to display the data than in Figure 4.4, which are plotted against specific capacity of the entire cell. **a)** Experimental values for the particle discussed in the ; the integrated diffracted intensity is used to estimate the volume of the particle. **b)** Predicted values according to the model for a spherical particle discussed above. From these plots, the relationship between d-spacing and extent of reaction for this particle closely mirrors the relationship between d-spacing and electrochemical reaction of the whole electrode (Figures 4.4 and 4.6).

4.4: Conclusions

This study has revealed the evolution of structure and mechanical strain in large-volume-change alloying anodes for Li-ion batteries using operando synchrotron diffraction techniques. Diffraction from single c-Ge particles was tracked during discharge of half cells, and the diffracted intensity and crystallographic strain were examined. Since lithiation of c-Ge converts the material to an amorphous phase and then a highly lithiated crystalline $\text{Li}_{15}\text{Ge}_4$ phase, the extent of reaction can be monitored via the diffracted

intensity from the c-Ge phase. Additionally, the shift in the position of the diffraction peak provided information on crystallographic strain within the reacting particle. It was found that compressive strain was generated during lithiation (as measured along the [111] crystallographic direction in these experiments), which agrees well with previous modeling. The emergence of compressive strain within the interior of these particles is somewhat counterintuitive, as the overall volumetric transformation of these particles involves expansion. However, it is the nature of the two-phase reaction within particles that gives rise to this compression, as the expanded outer region exerts compressive forces on the crystalline interior.

These observations provide important experimental insight into the chemomechanics of large-volume-change phase transformations in alloying anodes. The enhanced knowledge of chemomechanical behavior of these materials is important for designing battery materials with optimal shape, size, and structure to withstand electrochemical transformations while avoiding fracture and mechanical degradation. Moreover, since the large mechanical stress that evolves within two-phase alloying materials has been shown to influence the driving force for reaction, it is critical to experimentally measure strain and stress in these battery materials with operando and in situ techniques. One challenge with studying such materials with coherent diffraction-based techniques is that alloying anodes generally undergo significant structural changes during Li insertion and removal, which makes investigation of further charge and discharge cycles difficult. However, as demonstrated here, these methods can be particularly useful for understanding mechanical phenomena during electrochemical reactions. Future work will be designed to link detailed morphological changes in such particles, as obtained via phase-retrieval algorithms, to mechanical strain evolution.

4.5: References

1. McDowell, M. T.; Lee, S. W.; Nix, W. D.; Cui, Y. 25th Anniversary Article: Understanding the Lithiation of Silicon and Other Alloying Anodes for Lithium-Ion Batteries. *Adv. Mater.* **2013**, *25*, 4966-4985.
2. Obrovac, M. N.; Chevrier, V. L. Alloy Negative Electrodes for Li-Ion Batteries. *Chem. Rev.* **2014**, *114*, 11444-11502.
3. Choi, S.; Kwon, T.-w.; Coskun, A.; Choi, J. W. Highly Elastic Binders Integrating Polyrotaxanes for Silicon Microparticle Anodes in Lithium Ion Batteries. *Science* **2017**, *357*, 279-283.
4. Sun, Y.; Liu, N.; Cui, Y. Promises and Challenges of Nanomaterials for Lithium-Based Rechargeable Batteries. *Nat. Energy* **2016**, *1*, 16071.
5. McDowell, M. T.; Xia, S.; Zhu, T. The Mechanics of Large-Volume-Change Transformations in High-Capacity Battery Materials. *Extreme Mech. Lett.* **2016**, *9*, 480-494.
6. McDowell, M. T.; Ryu, I.; Lee, S. W.; Wang, C.; Nix, W. D.; Cui, Y. Studying the Kinetics of Crystalline Silicon Nanoparticle Lithiation with In Situ Transmission Electron Microscopy. *Adv. Mater.* **2012**, *24*, 6034-6041.
7. Ebner, M.; Marone, F.; Stampanoni, M.; Wood, V. Visualization and Quantification of Electrochemical and Mechanical Degradation in Li Ion Batteries. *Science* **2013**, *342*, 716-720.
8. Liu, X. H.; Zhong, L.; Huang, S.; Mao, S. X.; Zhu, T.; Huang, J. Y. Size-Dependent Fracture of Silicon Nanoparticles During Lithiation. *ACS Nano* **2012**, *6*, 1522-1531.
9. Liu, N.; Lu, Z.; Zhao, J.; McDowell, M. T.; Lee, H.-W.; Zhao, W.; Cui, Y. A Pomegranate-Inspired Nanoscale Design for Large-Volume-Change Lithium Battery Anodes. *Nat. Nanotechnol.* **2014**, *9*, 187-192.
10. Weker, J. N.; Liu, N.; Misra, S.; Andrews, J. C.; Cui, Y.; Toney, M. F. In Situ Nanotomography and Operando Transmission X-Ray Microscopy of Micron-Sized Ge Particles. *Energy Environ. Sci.* **2014**, *7*, 2771-2777.
11. Lim, L. Y.; Liu, N.; Cui, Y.; Toney, M. F. Understanding Phase Transformation in Crystalline Ge Anodes for Li-Ion Batteries. *Chem. Mater.* **2014**, *26*, 3739-3746.
12. Liang, W.; Yang, H.; Fan, F.; Liu, Y.; Liu, X. H.; Huang, J. Y.; Zhu, T.; Zhang, S. Tough Germanium Nanoparticles under Electrochemical Cycling. *ACS Nano* **2013**, *7*, 3427-3433.
13. McDowell, M. T.; Lee, S. W.; Harris, J. T.; Korgel, B. A.; Wang, C.; Nix, W. D.; Cui, Y. In Situ TEM of Two-Phase Lithiation of Amorphous Silicon Nanospheres. *Nano Lett.* **2013**, *13*, 758-764.

14. Cook, J. B.; Lin, T. C.; Detsi, E.; Weker, J. N.; Tolbert, S. H. Using X-Ray Microscopy to Understand How Nanoporous Materials Can Be Used to Reduce the Large Volume Change in Alloy Anodes. *Nano Lett.* **2017**, *17*, 870-877.
15. Wang, J.; Fan, F.; Liu, Y.; Jungjohann, K. L.; Lee, S. W.; Mao, S. X.; Liu, X.; Zhu, T. Structural Evolution and Pulverization of Tin Nanoparticles During Lithiation-Delithiation Cycling. *J. Electrochem. Soc.* **2014**, *161*, F3019-F3024.
16. Liu, X. H.; Wang, J. W.; Huang, S.; Fan, F.; Huang, X.; Liu, Y.; Krylyuk, S.; Yoo, J.; Dayeh, S. A.; Davydov, A. V., *et al.* In Situ Atomic-Scale Imaging of Electrochemical Lithiation in Silicon. *Nat. Nanotechnol.* **2012**, *7*, 749-756.
17. Jung, H.; Allan, P. K.; Hu, Y.-Y.; Borkiewicz, O. J.; Wang, X.-L.; Han, W.-Q.; Du, L.-S.; Pickard, C. J.; Chupas, P. J.; Chapman, K. W., *et al.* Elucidation of the Local and Long-Range Structural Changes That Occur in Germanium Anodes in Lithium-Ion Batteries. *Chem. Mater.* **2015**, *27*, 1031-1041.
18. Lee, S. W.; Ryu, I.; Nix, W. D.; Cui, Y. Fracture of Crystalline Germanium During Electrochemical Lithium Insertion. *Extreme Mech. Lett.* **2015**, *2*, 15-19.
19. Liu, X. H.; Huang, S.; Picraux, S. T.; Li, J.; Zhu, T.; Huang, J. Y. Reversible Nanopore Formation in Ge Nanowires During Lithiation–Delithiation Cycling: An In Situ Transmission Electron Microscopy Study. *Nano Lett.* **2011**, *11*, 3991-3997.
20. Pharr, M.; Choi, Y. S.; Lee, D.; Oh, K. H.; Vlassak, J. J. Measurements of Stress and Fracture in Germanium Electrodes of Lithium-Ion Batteries During Electrochemical Lithiation and Delithiation. *J. Power Sources* **2016**, *304*, 164-169.
21. Chon, M. J.; Sethuraman, V. A.; McCormick, A.; Srinivasan, V.; Guduru, P. R. Real-Time Measurement of Stress and Damage Evolution During Initial Lithiation of Crystalline Silicon. *Phys. Rev. Lett.* **2011**, *107*, 045503.
22. Nadimpalli, S. P. V.; Tripuraneni, R.; Sethuraman, V. A. Real-Time Stress Measurements in Germanium Thin Film Electrodes During Electrochemical Lithiation/Delithiation Cycling. *J. Electrochem. Soc.* **2015**, *162*, A2840-A2846.
23. Yang, H.; Fan, F.; Liang, W.; Guo, X.; Zhu, T.; Zhang, S. A Chemo-Mechanical Model of Lithiation in Silicon. *J. Mech. Phys. Sol.* **2014**, *70*, 349-361.
24. Zhao, K.; Pharr, M.; Wan, Q.; Wang, W. L.; Kaxiras, E.; Vlassak, J. J.; Suo, Z. Concurrent Reaction and Plasticity During Initial Lithiation of Crystalline Silicon in Lithium-Ion Batteries. *J. Electrochem. Soc.* **2012**, *159*, A238-A243.
25. Zeng, Z.; Liu, N.; Zeng, Q.; Lee, S. W.; Mao, W. L.; Cui, Y. In Situ Measurement of Lithiation-Induced Stress in Silicon Nanoparticles Using Micro-Raman Spectroscopy. *Nano Energy* **2016**, *22*, 105-110.
26. Tardif, S.; Pavlenko, E.; Quazuguel, L.; Boniface, M.; Maréchal, M.; Micha, J.-S.; Gonon, L.; Mareau, V.; Gebel, G.; Bayle-Guillevaud, P., *et al.* Operando Raman Spectroscopy and Synchrotron X-Ray Diffraction of Lithiation/Delithiation in Silicon Nanoparticle Anodes. *ACS Nano* **2017**, *11*, 11306-11316.

27. Taiwo, O. O.; Paz-García, J. M.; Hall, S. A.; Heenan, T. M. M.; Finegan, D. P.; Mokso, R.; Villanueva-Pérez, P.; Patera, A.; Brett, D. J. L.; Shearing, P. R. Microstructural Degradation of Silicon Electrodes During Lithiation Observed Via Operando X-Ray Tomographic Imaging. *J. Power Sources* **2017**, *342*, 904-912.
28. Ulvestad, A.; Singer, A.; Cho, H.-M.; Clark, J. N.; Harder, R.; Maser, J.; Meng, Y. S.; Shpyrko, O. G. Single Particle Nanomechanics in Operando Batteries Via Lensless Strain Mapping. *Nano Lett.* **2014**, *14*, 5123-5127.
29. Ulvestad, A.; Singer, A.; Clark, J. N.; Cho, H. M.; Kim, J. W.; Harder, R.; Maser, J.; Meng, Y. S.; Shpyrko, O. G. Topological Defect Dynamics in Operando Battery Nanoparticles. *Science* **2015**, *348*, 1344-1347.
30. Robinson, I.; Harder, R. Coherent X-Ray Diffraction Imaging of Strain at the Nanoscale. *Nat. Mater.* **2009**, *8*, 291-298.
31. Ulvestad, A.; Welland, M. J.; Cha, W.; Liu, Y.; Kim, J. W.; Harder, R.; Maxey, E.; Clark, J. N.; Highland, M. J.; You, H., *et al.* Three-Dimensional Imaging of Dislocation Dynamics During the Hydriding Phase Transformation. *Nat. Mater.* **2017**, *16*, 565-571.
32. Newton, M. C.; Leake, S. J.; Harder, R.; Robinson, I. K. Three-Dimensional Imaging of Strain in a Single ZnO Nanorod. *Nat. Mater.* **2010**, *9*, 120-124.
33. Marchesini, S. Invited Article: A Unified Evaluation of Iterative Projection Algorithms for Phase Retrieval. *Rev. Sci. Instr.* **2007**, *78*, 011301.
34. Cherukara, M. J.; Sasikumar, K.; Cha, W.; Narayanan, B.; Leake, S. J.; Dufresne, E. M.; Peterka, T.; McNulty, I.; Wen, H.; Sankaranarayanan, S. K. R. S., *et al.* Ultrafast Three-Dimensional X-Ray Imaging of Deformation Modes in ZnO Nanocrystals. *Nano Lett.* **2017**, *17*, 1102-1108.
35. Yau, A.; Cha, W.; Kanan, M. W.; Stephenson, G. B.; Ulvestad, A. Bragg Coherent Diffractive Imaging of Single-Grain Defect Dynamics in Polycrystalline Films. *Science* **2017**, *356*, 739.
36. Hubbell, J. H.; Seltzer, S. M., *Tables of X-Ray Mass Attenuation Coefficients and Mass Energy-Absorption Coefficients* National Institute of Standards and Technology: Gaithersburg, MD, 2004.
37. Key, B.; Morcrette, M.; Tarascon, J.-M.; Grey, C. P. Pair Distribution Function Analysis and Solid State NMR Studies of Silicon Electrodes for Lithium Ion Batteries: Understanding the (De)Lithiation Mechanisms. *J. Am. Chem. Soc.* **2011**, *133*, 503-512.
38. Lee, S. W.; Lee, H.-W.; Ryu, I.; Nix, W. D.; Gao, H.; Cui, Y. Kinetics and Fracture Resistance of Lithiated Silicon Nanostructure Pairs Controlled by Their Mechanical Interaction. *Nat. Commun.* **2015**, *6*, 7533.
39. Xu, R.; Zhao, K. Mechanical Interactions Regulated Kinetics and Morphology of Composite Electrodes in Li-Ion Batteries. *Extreme Mech. Lett.* **2016**, *8*, 13-21.

40. McDowell, M. T.; Lee, S. W.; Ryu, I.; Wu, H.; Nix, W. D.; Choi, J. W.; Cui, Y. Novel Size and Surface Oxide Effects in Silicon Nanowires as Lithium Battery Anodes. *Nano Lett.* **2011**, *11*, 4018-4025.
41. Lee, S. W.; McDowell, M. T.; Berla, L. A.; Nix, W. D.; Cui, Y. Fracture of Crystalline Silicon Nanopillars During Electrochemical Lithium Insertion. *Proc. Nat. Acad. Sci.* **2012**, *109*, 4080-4085.
42. Wei, S.; Allan, D. C.; Wilkins, J. W. Elastic Constants of a Si/Ge Superlattice and of Bulk Si and Ge. *Phys. Rev. B* **1992**, *46*, 12411-12420.
43. Fine, M. E. Elasticity and Thermal Expansion of Germanium between -195 and 275°C. *J. Appl. Phys.* **1953**, *24*, 338-340.

CHAPTER 5: ENGINEERING INTERFACES OF CURRENT COLLECTORS

5.1: Introduction

Commercial Li-ion batteries were first introduced by Sony Corporation in 1991 and have become the dominant battery chemistry for consumer electronics and electric vehicles.¹ Immense progress has been made from the first commercial batteries designed in the mid 1980's in order to improve energy density, safety and cost. The energy density of Li-ion batteries increased steadily at a rate of 10 % every year between 1991 and 2005.² These improvements were obtained by engineering the anode and cathode materials and optimizing the liquid electrolyte composition. For example, anode materials have changed from hard-carbon to graphite,¹ the composition of the LiCoO₂ cathode material has been engineered by incorporating Ni, Mn and Al,³ and the liquid electrolyte composition has been modified with different salts and additives to control SEI formation.⁴ Despite all these changes in the rest of the battery components, the current collectors of the first intercalation rechargeable Li-ion battery described in Yoshida's patent in 1985⁵ are the same standard current collectors used today⁶: 10 μm Cu foil for the anode and 15 μm Al foil for the cathode. This begs the question: what advances are possible at current collectors?

The role of current collectors is to connect the active materials to the external circuit. For this reason, current collectors need to be highly conductive and mechanically robust and adhesive to support the electrode materials.⁷⁻⁹ Cu foils are used as the anode current collector due to their electrochemical stability at low potentials vs Li/Li⁺.^{10,11} Al alloys with Li below 0.2 V vs Li/Li⁺, but it is stable at high potentials, so it is used on the

cathode side.¹² Electrochemical stability aside, Cu foils cost 4 times as much as Al foils and are 3 times denser, which suggests that replacing Cu current collectors with Al could reduce the weight and cost of Li-ion batteries. The reduction in cost could be around 3 - 6 % per kWh with a respective increase in gravimetric energy density around 3 - 6 % for conventional⁶ as well as next-generation¹³ Li-based batteries, as shown in Figure 1.1.

The alternative to using Al as the anode current collector in Li-ion batteries has been explored previously. Given its electrochemical stability window, Al can be used as the anode current collector for higher voltage anode materials such as lithium titanate, which intercalates lithium at 1.5 V vs Li/Li⁺.¹⁴ Another approach has been to use Al as an active metal current collector. The Li-Al alloying reaction has a theoretical capacity of 993 mAh g⁻¹ and a volume expansion of 90 %, which limits the cyclability of Al as an anode material.¹⁵ A recent study showed extended cycling stability of Al foils that had been pretreated to increase their hardness.¹⁶ In that work, only a fraction of the thickness of the Al foil was used as the anode material, while the bulk served as the current collector. Other examples of active metal current collectors include hand-pressing Li and Al foils together,¹⁷⁻¹⁹ heating and roll-pressing LiAl alloys,²⁰ and cold-rolling Al with Sn to form an interdigitated eutectic alloy.²¹ Lastly, protection layers have been studied as alternatives to enable Al anode current collectors. For example, Liu *et al.*²² used a 500 nm Sn protection layer and observed low current densities and no measurable Li in the Al current collector at potentials as low as 0.2 V vs Li/Li⁺ for up to 6 hours.

Extending the stability of Al anode current collectors for commercially relevant periods of time using protection layers requires a different approach. This protection layer should be a low-cost material and meet the following criteria: 1) it should be electrically conductive, 2) it should not react with Li, and 3) it should block lithium diffusion. While Cu may appear to be an obvious candidate, it has been demonstrated that lithium can diffuse into this material when it is used as a current collector.^{23,24} TiN is also a promising material

that is commonly used as a diffusion blocker. TiN was used in microbatteries to prevent the reaction of Si substrates at low potentials vs Li/Li⁺.^{25,26} However, it was also found that TiN was able to incorporate moderate amounts of lithium proportionally to the thickness of the film.^{25,27}

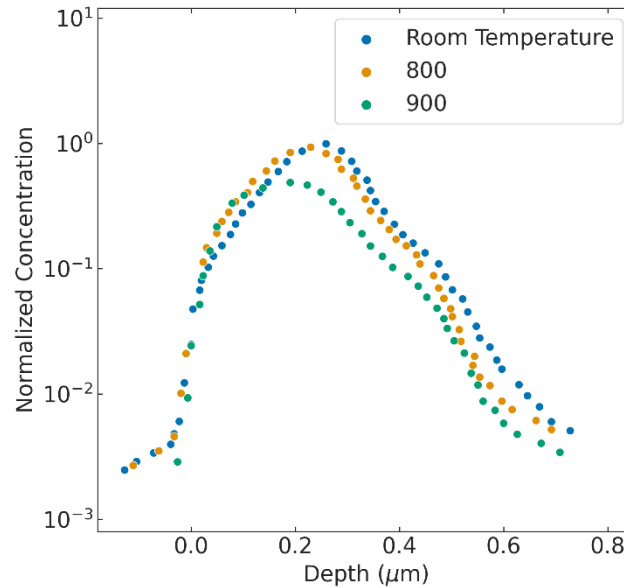


Figure 5.1. Concentration profile measured by Neutron Depth Profiling of implanted Li on an Fe target after 1 h of annealing at different temperatures: room temperature, 800 °C and 900 °C. Replotted from ²⁸

Conditions 1 and 2 point to metals that do not react with lithium, such as Mo, Nb, Ti, Ni, Cr or Fe.^{29–34} Condition 3, however, seems more elusive. Fink *et al.*²⁸ reported the diffusivity of lithium in those metals, except for Cr and Fe. Cr was the only material from this list that was not examined in that study. In the case of Fe, they found that Li diffusion is severely hindered.²⁸ Figure 5.1, replotted from²⁸, shows neutron depth profiles of Fe samples in which Li ions had been implanted at an energy of 100 keV using a heavy ion accelerator at room temperature. After implantation, the samples were annealed at room temperature, 800 °C and 900 °C for 1 h. Figure 5.1 shows that the concentration profiles are essentially identical regardless of the annealing temperature. The conclusion that

follows is that the Li ions were unable to diffuse into the Fe matrix. This is in contrast to materials such as Cu in which the concentration profiles of Li become flatter as annealing temperature increases, which is to be expected to happen in regular thermal diffusion.²⁸ Using this evidence that Fe meets all 3 criteria, we test Fe as a protection layer for Al anode current collectors.

In this chapter, we test the hypothesis that an electrically conductive thin film that does not react with lithium and blocks lithium diffusion, such as Fe, can prevent the alloying reaction between Li and Al in anode current collectors. We use potentiostatic holds at 10 mV vs Li/Li⁺ to simulate the electrochemical environment of fully charged batteries. These tests reveal that sub-micron thick Fe films extend the stability of Al anode current collectors to hundreds of hours with current densities comparable to copper anode current collectors, the incumbent technology. Implementing this new technology in commercial batteries could reduce the cost and weight of the cells by 3 - 6 %.

5.2: Methods

Sample Preparation: The Al foil substrates were 15 μm in thickness and supplied by a commercial vendor. Prior to sputtering, the foils were secured on a stainless steel or glass slide by means of adhesive tape. The Al foils used had two distinct sides, one more lustrous than the other. In all cases, the Fe films were sputtered on the more lustrous side. For building coin cells, the Al foils were secured on stainless steel spacers (1.55 cm in diameter) using double-sided conductive carbon tape. The area of the foil, tape and stainless steel spacer were approximately the same. In the case of flooded cells, strips of Al foil were taped onto glass slides using double-sided kapton tape of the same width as the Al strips. The Al strips were longer than the glass slide onto which they were taped in order to make electrical connections. After securing the foils, they were pressed firmly

against the tape with compressed nitrogen in order to ensure a flat surface. Immediately before loading the samples in the sputterer, the samples were rinsed with isopropyl alcohol and dried with nitrogen.

Sputtering: Fe films were sputtered on Al foil substrates using DC magnetron sputtering.

Cell Construction: Electrochemical cells were constructed using metallic Li as counter and reference electrode, a 1.0 M solution of lithium hexafluorophosphate in ethylene carbonate and diethyl carbonate (1:1 volume ratio, Sigma) as electrolyte, and the test foil as working electrode. Two types of cell were used: coin cells and flooded cells. CR2032 coin cells were constructed in an Ar glovebox (<0.1 ppm water, <0.3 ppm oxygen) with the following stack order inside the stainless steel case: stainless steel spring, test foil, celgard separator soaked in electrolyte, Li metal electrode. In the case of Fe-protected Al foils, the sputtered foils were stored in the same Ar glove box. The Li metal electrode was typically a disk 0.318 cm in diameter and the celgard separator was approximately 0.5 x 0.5 cm². The separator was placed away from the edges of the foil, and the Li electrode was placed in the center of the separator. In the case of Cu and Fe-protected Al foils with epoxy (Henkel Loctite EA 9460), the Li disk was 0.397 cm in diameter.

Flooded cells were constructed as depicted in Figure 5.4c. Quartz tubes 0.635 cm in diameter were adhered to the test foil using epoxy (Henkel Loctite EA 9460) and cured in ambient air at room temperature for ~12 h before a second layer was applied and cured in the same conditions. After this, the cell was brought into the glovebox. Small squares of glass fiber (0.2-0.3 cm in length) were placed inside the quartz tube to cover the exposed area of the test foil. After this, ~30 μ L of electrolyte were pipetted into the tube. The Li metal electrode was cut in ~1 x 1 cm² pieces, polished, and wrapped around the end of a Cu wire, covering its tip completely. The Cu wire was inserted into the quartz tube ensuring that the Li metal electrode was pressed against the glass fiber separator and

fully submerged in the electrolyte. The other end of the Cu wire extended past the opening of the quartz tube. The cell was finally sealed with the same epoxy inside the glovebox and cured at room temperature for at least 12 h before electrochemical testing. The area used for calculating the current density of each experiment with flooded cells was the exposed area of the test foil at the bottom of the cell.

Electrochemical Testing: All cells underwent linear sweep voltammetry followed by potentiostatic holds using a Bio-Logic VMP3 potentiostat at room temperature. The rate of the linear sweep voltammetry was 0.1 mV s^{-1} from open circuit potential to 10 mV. The voltage was subsequently held at 10 mV.

Surface Characterization: Scanning electron microscopy (SEM) was used to probe the surface of Fe-protected Al foils. The instrument used for SEM was a Zeiss Ultra60 FE-SEM with an accelerating voltage of 5 or 10 kV, and the samples were transferred in air. In the case of electrochemically tested samples, care was taken to reduce the transfer time to under 30 s.

5.3: Results and Discussion

Figure 5.2 shows the stability of Fe-protected Al foils in contrast to bare Al and Cu current collectors. In this test, 800 nm of Fe was sputtered on commercial Al foils. The foils were used as the working electrode in a coin cell with metallic lithium as the counter electrode. Prior to the potentiostatic hold at 10 mV vs Li/Li⁺ shown in the figure 5.2, the cell was brought from open circuit potential (around 3 V) through a linear sweep voltammetry at a rate of 0.1 mV/s. This protocol resembles slow battery charge and then simulates the electrochemical environment of the current collector when the anode is fully lithiated for extended periods of time.^{35–37} The comparison in Figure 5.2a shows that the evolution of current in the Fe-protected aluminum current collectors is essentially identical

to the case of standard copper current collectors. In comparison, bare aluminum evolves current densities two orders of magnitude higher than what is observed for copper current collectors. This larger current density in bare aluminum is related to large morphological changes in the foil as shown in Figure 5.2d. In this case, the bare Al foil was completely pulverized, leaving a hole in the reacted area directly underneath the Li electrode.

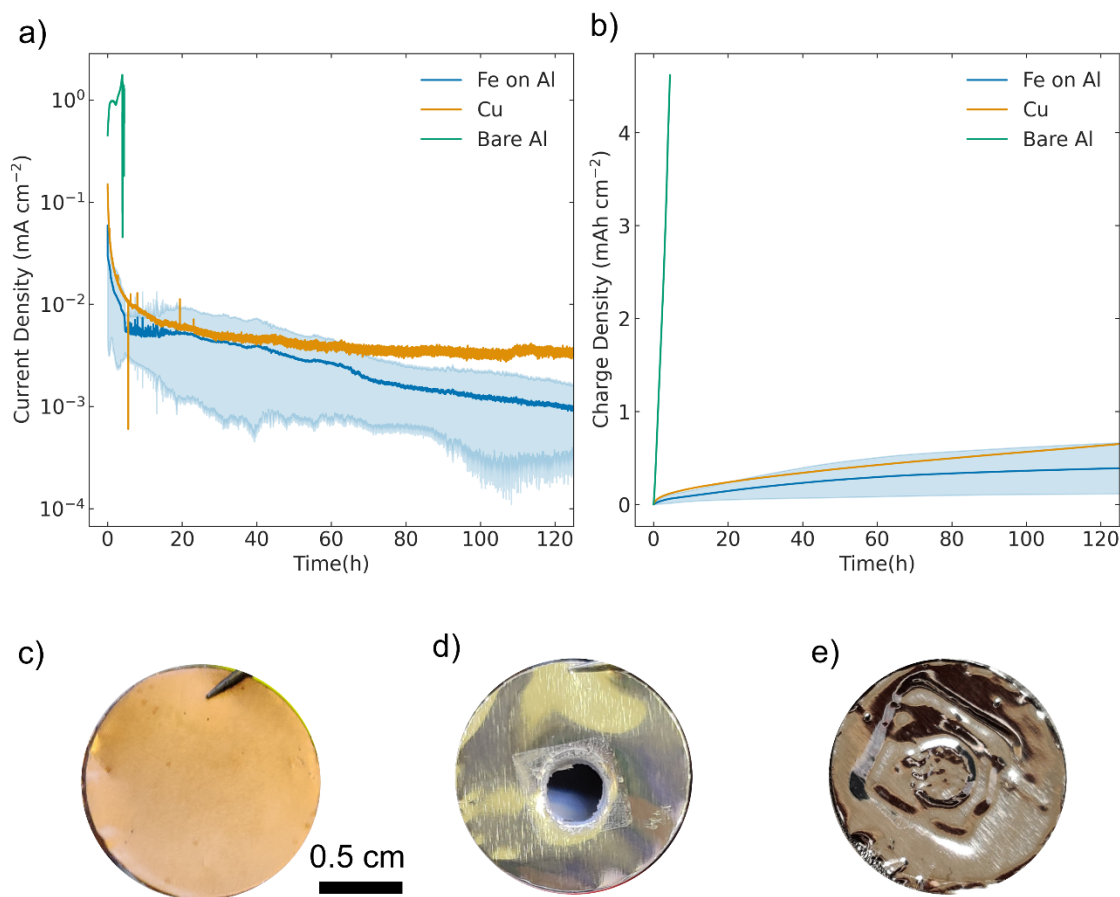


Figure 5.2. Performance of Fe protection layer on Al compared to Cu and bare Al. **a)** Evolution of current density over 120 h of potentiostatic hold at 10 mV for Cu, bare and Fe-protected Al. The darker blue line represents the average of 3 replicates of the same experimental condition, and the light blue area shows the standard deviation. **b)** Evolution of transferred charge density corresponding to the experiments in a. Photographs of **c)** Cu, **d)** bare Al, **e)** Fe-Protected Al after potentiostatic hold at 10 mV. Notice the hole in d matching the shape and location of the Li electrode. The imprint of the separator and Li electrode are only visible in e because the foil was fixed with carbon tape on a steel current collector while the other ones had no carbon tape.

In contrast, the lower current densities are correlated with no visible changes in the morphology or mechanical integrity of the foils, as shown in Figure 5.2 c, e. In the case of the Fe-protected Al foil, no pulverization occurred. Although the foil does not appear flat as compared to the Cu foil, this is not due to decomposition of the Al foil. Instead, it is due to the fact that the Al foil was supported on carbon tape onto a stainless steel spacer prior to sputtering. During the fabrication of the coin cell, the separator and Li electrode are pressed against the foil, deforming the underlying carbon tape. In the case of Cu or bare Al foil, no carbon tape was used, which is why those foils appear flat after the electrochemical testing procedure.

The observed current can come from various sources. In the case of bare Al, most of the current comes from the reaction with Li, while in the case of bare Cu it likely comes from electrolyte decomposition. Figure 5.2b shows the cumulative charge density transferred corresponding to the current density plots in Figure 5.2a. Assuming Al reacts with Li to form LiAl, with a theoretical capacity of 993 mAh cm^{-3} , the areal charge density transferred in lithiating a $15 \text{ }\mu\text{m}$ foil is $\sim 4 \text{ mAh cm}^{-2}$. It can be seen that the bare Al foil reaches that charge density within less than 5 hours, suggesting rapid lithiation of Al. This lithiation causes a volume change of 90 % and is known to induce pulverization in Al anodes,¹⁶ which is consistent with the foil destruction observed in Figure 5.2d.

The current evolution in Cu current collectors has a different origin. As shown in Figure 5.2a,b, the current density and cumulative charge density of Cu is significantly lower than that of Al, but it is non-zero. Lin *et al.*³⁸ studied this phenomenon and postulated that Cu continuously reacts with the electrolyte. They observed differences in the composition and thickness of the SEI on Cu versus Li and found that it is thinner on Cu than on Li. According to them, the decomposition of the electrolyte on Cu produces soluble products, and the thickness of the SEI is a result of a balance between SEI formation and dissolution that occurs continuously. This decomposition reaction at low potentials vs Li/Li⁺

produces a small current. This is an indication that the observed current comes from electrolyte decomposition and not lithiation of the Al foil.

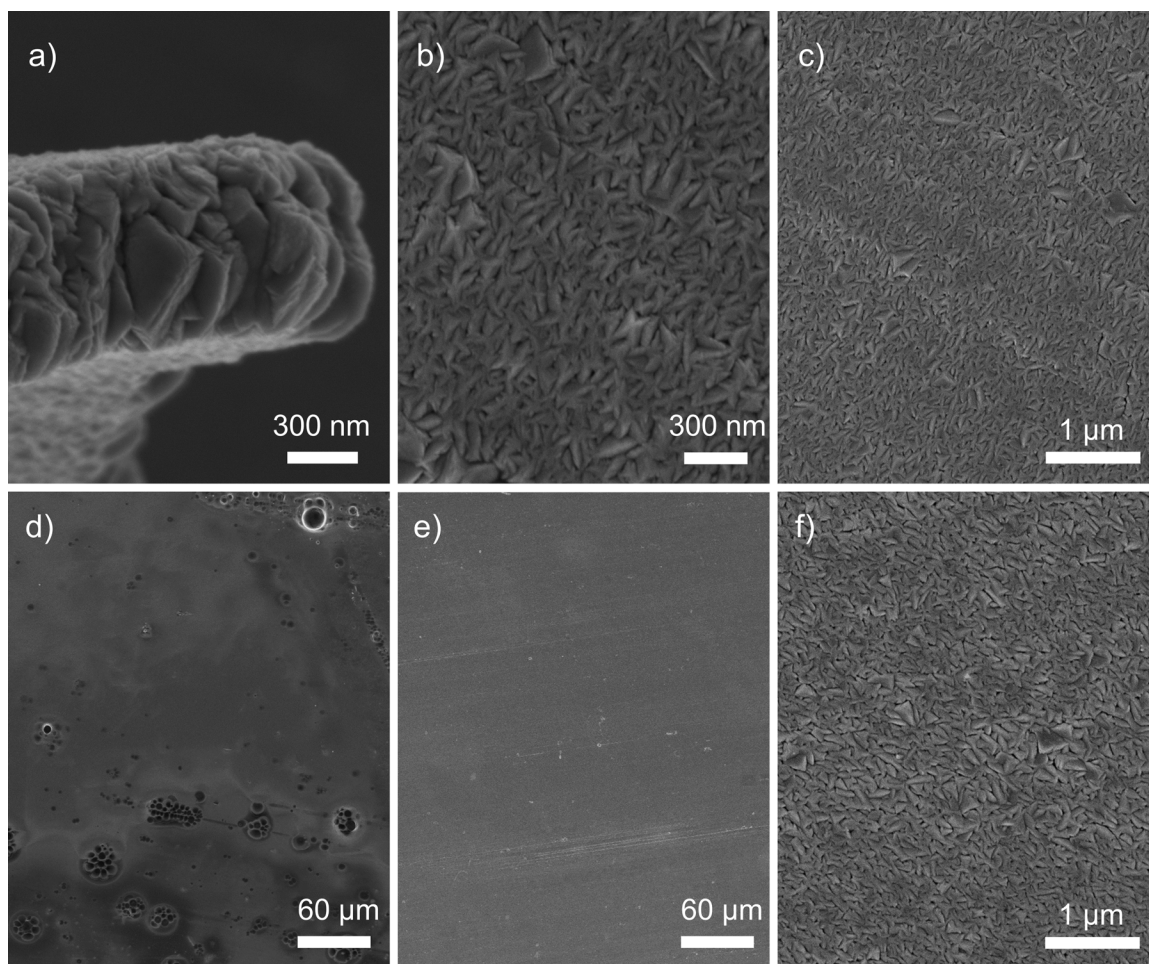


Figure 5.3. Scanning electron microscopy images of the sputtered Fe film. **a)** Cross section from a pristine sample. **b, c)** Top views of the film at different magnifications. **d)** Top view of an Fe-protected film after 120 h of potentiostatic hold at 10 mV rinsed with PC. **e)** Top view of an Fe-protected film after 120 h of potentiostatic hold at 10 mV rinsed with water and acetone (same magnification as d for comparison). **f)** Higher magnification of the sample in e (same magnification as c for comparison). Images in d-f were taken from the region that sat directly below the Li electrode.

The mechanical stability of the Fe films was further confirmed through electron microscopy. Figure 5.3a-c show the morphology of pristine Fe films on Al foils. Figure 5.3a shows an image of a flake of film lifted off the Al substrate. This type of detachment was observed in samples that had not been properly cleaned prior to sputtering or had visible scratches before sputtering. The cross section of the film revealed in Figure 5.3 shows the

polycrystalline structure of the film and the abundance of grain boundaries perpendicular to the Al substrate. Figure 5.3d-f shows top views of the film after 120 h of potentiostatic hold at 10 mV. The micrograph in Figure 5.3d was obtained after rinsing the sample with propylene carbonate. The surface of this sample did not exhibit the characteristic grain boundaries of the pristine film and was highly susceptible to beam damage. For example, some of the clusters of circles in Figure 5.3d appeared after exposure to the electron beam. This suggests that the Fe-protected Al foil was covered in SEI. The top views in Figure 5.3e,f correspond to a sample prepared in the same way as the one in Figure 5.3d except that the Fe-protected Al foil was rinsed in water and acetone to remove the SEI. The top views of this sample look very similar to what we observed in pristine Fe films (compare to Figure 5.3b,c). We found no evidence of damage in the Fe film (such as cracks or flakes) compared to the pristine samples.

One of the biggest challenges that come with testing a protection layer on a current collector is that the unprotected edges and back of the foil need to be isolated from the liquid electrolyte. In the experiments shown above, this was achieved by making the lithium counter electrode and the celgard separator much smaller than the foil inside the coin cell. In our earlier attempts, we used flooded cells such as the one depicted in Figure 5.4c,d. In those cells, abundant amounts of lithium and liquid electrolyte were confined to a small area away from the edges of the foil. This cell configuration was used to identify early signs of failure.

The electrochemical tests on flooded cells provide evidence that extended stability of Al current collectors is possible. The longest time before failure demonstrated in this cell configuration was over 1000 h, more than three orders of magnitude longer than without the protection. A comparison between Figures 5.2a and 5.4a suggests that the coin cells without epoxy could be stable for similar periods of time. This experimental evidence indicates that Fe is indeed preventing the lithiation of Al.

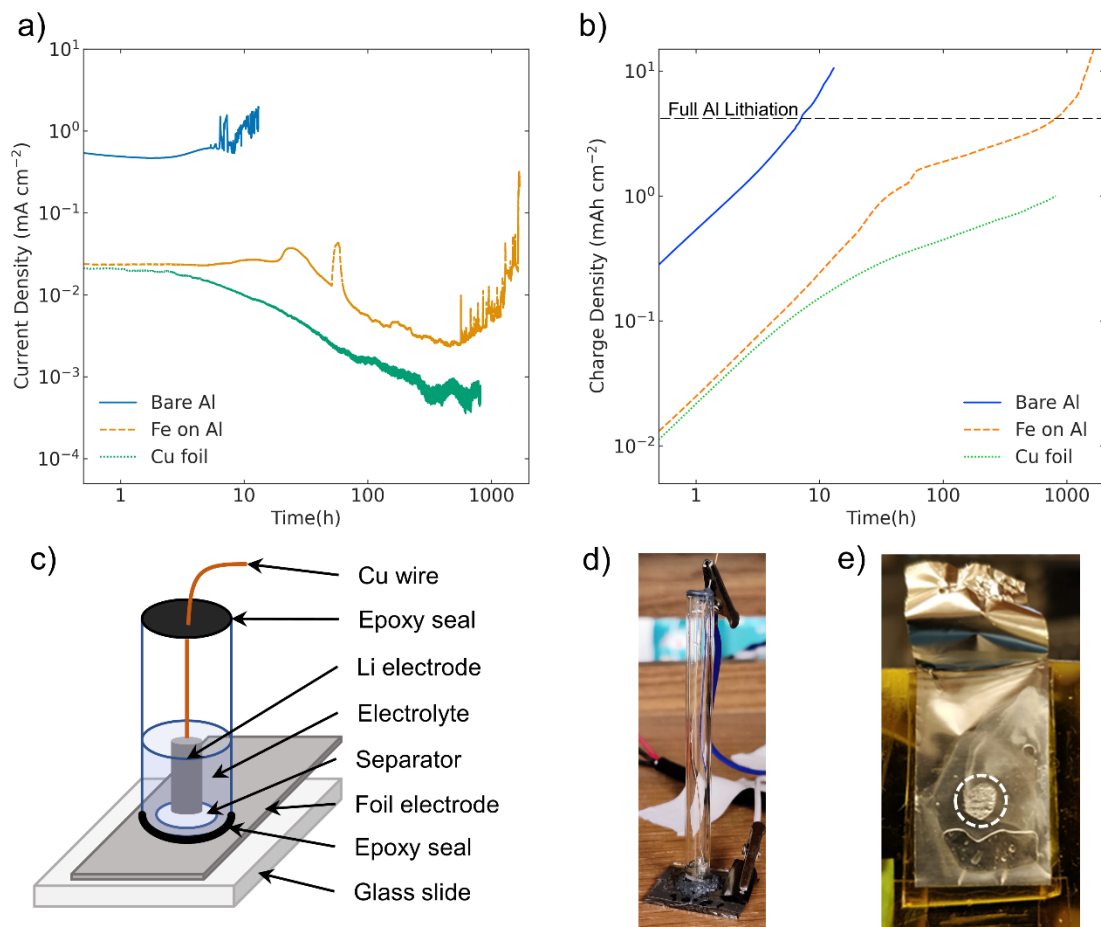


Figure 5.4. Flooded cell configuration and demonstration of long stability. **a)** Current density evolution of various foils in flooded cells during potentiostatic hold at 10 mV. **b)** Charge density evolution corresponding to the experiments in a. **c)** Schematic of the flooded cell configuration. **d)** Photograph of a flooded cell. **e)** Back-side of an Fe-protected Al foil during failure. The dotted circle marks the location of the active components of the flooded cell.

Figures 5.4a and b show the current transients of flooded cells over extended periods of time. We observe low current densities for hundreds of hours, with a dramatic increase towards the end. This increase in current density above 0.1 mA cm^{-2} is indicative of failure. Figure 5.4e shows the backside of a flooded cell after failure. The dotted circle shows an obvious change in the mechanical integrity of the foil. This suggests that rather than being a gradual process, once Li reaches Al through a defect, the reaction cascades rapidly. We propose that this occurs because of the volume expansion of Al upon lithiation.

This volume expansion would act to break the protective film and induce more defects, exposing more Al to the liquid electrolyte and the Li reservoir.

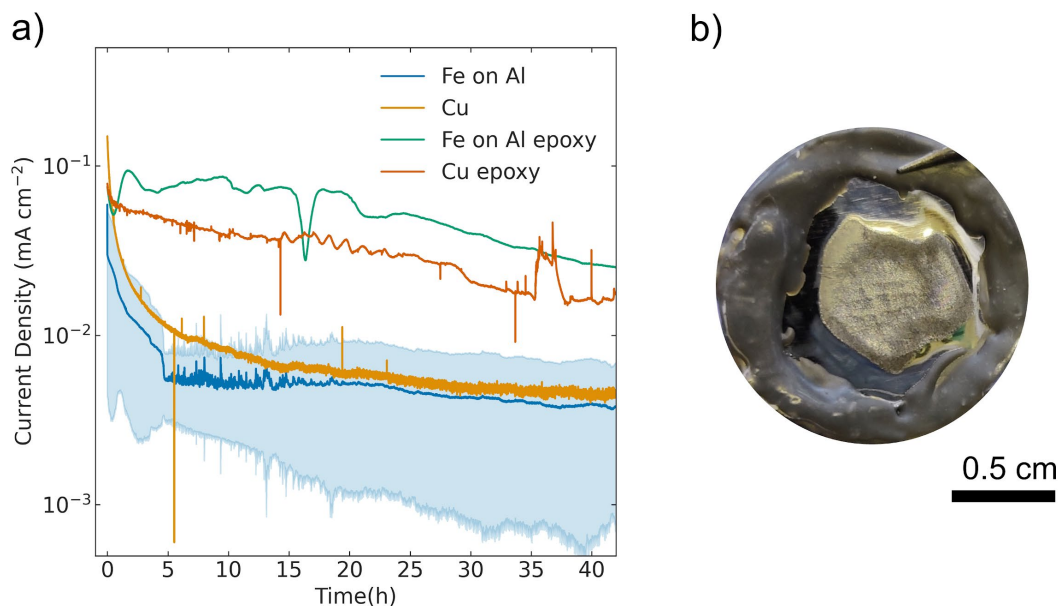


Figure 5.5. Effect of epoxy on current density evolution. **a)** Current density evolution of various coin cells with and without epoxy. **b)** Photograph of an Fe-protected foil sealed with epoxy after 120 h of potentiostatic hold at 10 mV showing a thick, grey SEI in the central area of the foil.

An important consideration in the analysis of flooded cells is the role of the epoxy used to seal them. The epoxy was in direct contact with the Fe protective layer and the liquid electrolyte, which means that it was subjected to the same electrochemical environment and prone to decomposition. To explore this possibility, we build coin cells with and without epoxy and compared them in Figure 5.5. It is clear from Figure 5.5a that Cu cells with epoxy evolve current densities about an order of magnitude higher than those without epoxy. This result translates to Fe-protected Al. Additionally, the Fe-protected Al cells with epoxy develop an SEI layer that is several microns in thickness. Such thick SEI is not visible in cells without epoxy, which suggests that the epoxy molecules are being reduced to form SEI. This observation indicates that the current density values obtained in flooded cells are inflated. Additionally, the fact that we observed failure in the flooded

cells suggests that the decomposition of the epoxy is not playing a role in extending the stability of those cells. What these experiments highlight is the importance of careful selection of materials and strategies to protect the edges and back of the Fe-protected Al current collectors in real-life applications.

5.4: Conclusions

This study demonstrates that Fe is a suitable material to prevent lithiation of Al foils at low potentials vs Li/Li⁺. Potentiostatic holds at 10 mV vs Li/Li⁺ show that Fe protected Al foils produce current densities comparable to Cu current collectors and can remain stable for more than 1000 h. No obvious morphological changes were observed after more than 100 h of potentiostatic holds. When failure occurs, the current density increases suddenly, suggesting that the failure process is rapid once it sets off. We propose that failure is due to the presence of defects in the Fe film. Further work is needed in order to establish the role of film thickness as well as to measure the distribution of Li across the Fe film. The results presented here could enable the use of Al anode current collectors as a replacement of Cu in Li-ion batteries.

5.5: References

1. Li, M., Lu, J., Chen, Z. & Amine, K. 30 Years of Lithium-Ion Batteries. *Adv. Mater.* e1800561 (2018).
2. Yoshio, M., Brodd, R. J. & Kozawa, A. *Lithium-Ion Batteries: Science and Technologies*. (Springer Science & Business Media, 2010).
3. Nitta, N., Wu, F., Lee, J. T. & Yushin, G. Li-ion battery materials: present and future. *Materials Today* vol. 18 252–264 (2015).
4. Li, Q., Chen, J., Fan, L., Kong, X. & Lu, Y. Progress in electrolytes for rechargeable Li-based batteries and beyond. *Green Energy & Environment* vol. 1 18–42 (2016).
5. Yoshino, A., Sanekata, K. & Nakajima, T. Secondary Battery. *Patent* (1987).

6. Nelson, P. A., Ahmed, S., Gallagher, K. G. & Dees, D. W. Modeling the Performance and Cost of Lithium-Ion Batteries for Electric-Drive Vehicles, Third Edition. (2019) doi:10.2172/1503280.
7. Son, B. *et al.* Measurement and analysis of adhesion property of lithium-ion battery electrodes with SAICAS. *ACS Appl. Mater. Interfaces* **6**, 526–531 (2014).
8. Song, Y., Shao, X., Guo, Z. & Zhang, J. Role of material properties and mechanical constraint on stress-assisted diffusion in plate electrodes of lithium ion batteries. *Journal of Physics D: Applied Physics* vol. 46 105307 (2013).
9. Zhu, J., Feng, J. & Guo, Z. Mechanical properties of commercial copper current-collector foils. *RSC Adv.* vol. 4 57671–57678 (2014).
10. Shu, J. *et al.* Comparative study on surface behaviors of copper current collector in electrolyte for lithium-ion batteries. *Electrochimica Acta* vol. 56 3006–3014 (2011).
11. Myung, S.-T., Sasaki, Y., Sakurada, S., Sun, Y.-K. & Yashiro, H. Electrochemical behavior of current collectors for lithium batteries in non-aqueous alkyl carbonate solution and surface analysis by ToF-SIMS. *Electrochimica Acta* vol. 55 288–297 (2009).
12. Iwakura, C. *et al.* Electrochemical characterization of various metal foils as a current collector of positive electrode for rechargeable lithium batteries. *Journal of Power Sources* vol. 68 301–303 (1997).
13. McCloskey, B. D. Attainable Gravimetric and Volumetric Energy Density of Li–S and Li Ion Battery Cells with Solid Separator-Protected Li Metal Anodes. *The Journal of Physical Chemistry Letters* vol. 6 4581–4588 (2015).
14. Stewart, S. *et al.* Optimizing the Performance of Lithium Titanate Spinel Paired with Activated Carbon or Iron Phosphate. *Journal of The Electrochemical Society* vol. 155 A253 (2008).
15. Qin, B. *et al.* Revisiting the Electrochemical Lithiation Mechanism of Aluminum and the Role of Li-rich Phases (Li 1 x Al) on Capacity Fading. *ChemSusChem* vol. 12 2609–2619 (2019).
16. Li, H. *et al.* Circumventing huge volume strain in alloy anodes of lithium batteries. *Nat. Commun.* **11**, 1584 (2020).
17. Wu, L., He, G. & Ding, Y. Ultrathin Al foils to fabricate dendrite-free Li–Al anodes. *Journal of Materials Chemistry A* vol. 7 25415–25422 (2019).
18. Kuksenko, S. P. Aluminum foil as anode material of lithium-ion batteries: Effect of electrolyte compositions on cycling parameters. *Russian Journal of Electrochemistry* vol. 49 67–75 (2013).
19. Kim, H. *et al.* Enhancing performance of Li–S cells using a Li–Al alloy anode coating. *Electrochemistry Communications* vol. 36 38–41 (2013).

20. Kim, M. S. *et al.* Enabling reversible redox reactions in electrochemical cells using protected LiAl intermetallics as lithium metal anodes. *Sci Adv* **5**, eaax5587 (2019).
21. Kreder, K. J., Heligman, B. T. & Manthiram, A. Interdigitated Eutectic Alloy Foil Anodes for Rechargeable Batteries. *ACS Energy Letters* vol. 2 2422–2423 (2017).
22. Liu, D. X., Cao, L. R. & Co, A. C. Demonstrating the Feasibility of Al as Anode Current Collector in Li-Ion Batteries via In Situ Neutron Depth Profiling. *Chemistry of Materials* vol. 28 556–563 (2016).
23. Nagpure, S. C., Gregory Downing, R., Bhushan, B. & Babu, S. S. Discovery of lithium in copper current collectors used in batteries. *Scripta Materialia* vol. 67 669–672 (2012).
24. Rehnlund, D. *et al.* Lithium trapping in alloy forming electrodes and current collectors for lithium based batteries. *Energy & Environmental Science* vol. 10 1350–1357 (2017).
25. Janski, R. *et al.* Lithium barrier materials for on-chip Si-based microbatteries. *Journal of Materials Science: Materials in Electronics* vol. 28 14605–14614 (2017).
26. Freixas, J. *et al.* Sputtered Titanium Nitride: A Bifunctional Material for Li-Ion Microbatteries. *Journal of The Electrochemical Society* vol. 162 A493–A500 (2015).
27. Baggetto, L. *et al.* On the electrochemistry of an anode stack for all-solid-state 3D-integrated batteries. *Journal of Power Sources* vol. 189 402–410 (2009).
28. Fink, D., Tjan, K. & Wang, L. On the thermal mobility of lithium in metals and semiconductors. *Radiation Effects and Defects in Solids* vol. 114 21–50 (1990).
29. Venkatraman, M. & Neumann, J. P. The Cr-Li (Chromium-Lithium) system. *Bulletin of Alloy Phase Diagrams* **5**, 399–400 (1984).
30. Predel, B. Li-Ni (Lithium-Nickel). in *Li-Mg – Nd-Zr* (ed. Madelung, O.) vol. H 1–1 (Springer-Verlag, 1997).
31. Predel, B. Li-Nb (Lithium-Niobium). in *Li-Mg – Nd-Zr* (ed. Madelung, O.) vol. H 1–2 (Springer-Verlag, 1997).
32. Predel, B. Li-Ti (Lithium-Titanium). in *Li-Mg – Nd-Zr* (ed. Madelung, O.) vol. H 1–2 (Springer-Verlag, 1997).
33. Predel, B. Li-Mo (Lithium-Molybdenum). in *Li-Mg – Nd-Zr* (ed. Madelung, O.) vol. H 1–1 (Springer-Verlag, 1997).
34. Predel, B. Fe-Li (Iron-Lithium). in *Dy-Er – Fr-Mo* (ed. Madelung, O.) vol. e 1–3 (Springer-Verlag, 1995).
35. Stiaszny, B. *et al.* Electrochemical characterization and post-mortem analysis of aged LiMn₂O₄–NMC/graphite lithium ion batteries part II: Calendar aging. *J. Power Sources* **258**, 61–75 (2014).

36. Hahn, S. L. *et al.* Quantitative validation of calendar aging models for lithium-ion batteries. *J. Power Sources* **400**, 402–414 (2018).
37. Keil, P. *et al.* Calendar Aging of Lithium-Ion Batteries: I. Impact of the Graphite Anode on Capacity Fade. *J. Electrochem. Soc.* **163**, A1872–A1880 (2016).
38. Lin, D. *et al.* Fast galvanic lithium corrosion involving a Kirkendall-type mechanism. *Nat. Chem.* **11**, 382–389 (2019).

CHAPTER 6: CONCLUSIONS AND RECOMMENDATIONS

In this thesis, we developed protection layers to extend the stability of solid electrolytes and current collectors, and we used *operando* synchrotron X-ray techniques to reveal interfacial phenomena in anode materials.

From chapter 2, we learned that it is possible to extend the interfacial stability of solid electrolytes using a conformal protection layer made of a metallic material that does not alloy with lithium. This finding contrasted with the more accepted approach of increasing lithium ‘wettability’ using alloying or insulating protection layers. The extended stability we observed with this protection layer prompted the hypothesis that the uniformity of the electric field at the interface played a role in the failure mechanisms of solid electrolytes. Following this hypothesis, and the generally accepted scientific notion that interfacial void formation governed the growth of filaments through the solid electrolyte, we studied the lithium-solid electrolyte interface using *operando* synchrotron X-ray tomography. Our tomographic data revealed a dynamic interface with smaller contacting regions formed when lithium was stripped from it. We created contact area maps and implemented a simple model to estimate the current density at each point in the interface. The results, presented in chapter 3, show current density concentrations orders of magnitude higher than the nominal current density, as well as a very broad distribution of current densities throughout the interface. Detailed current density maps, like the ones we created, can be used to test hypotheses about dendrite formation in stable solid electrolytes. One way to do this is to replicate our experiments using a stable solid electrolyte through which lithium dendrites are known to form. With the X-ray tomography data, it will be possible to map the locations where dendrites begin to form and overlay

these maps with current density maps generated with an algorithm similar to what we show in chapter 3. This might allow one to correlate dendrite formation to a local current density threshold, which would provide a more quantitative understanding of the process. More generally, the information extracted from current density maps can be used as the input for electrochemical models to predict overpotentials in electrochemical systems such as fuel cells and batteries.

In chapter 4, we used *operando* synchrotron X-ray Bragg diffraction to study the evolution of strain in the crystalline core of a germanium microparticle during its electrochemical lithiation. Our results provided the first single-particle measurements of strain evolution within an ensemble electrode of an alloying material. While the information we collected is valuable to design anode materials with optimal shape, size and structure to accommodate the large compressive strain and stress, it is possible to take this technique one step further. The same technique can be used to create detailed, direct-space maps of localized strain throughout the volume of a single particle. In our experiments, we were limited by the intensity of the X-ray beam. This intensity can be slightly improved using a different cell design, but it would be necessary to use a brighter X-ray source. One of the reasons why a brighter source will be needed is because the intensity of the diffracted X-rays is also a function of the size of the crystalline core, which shrinks as it is lithiated. It will be possible to get the necessary intensity in the coming years after the upgrade of the Advanced Photon Source is complete. With a higher intensity, it would also be possible to study lighter alloying anodes, such as silicon, which is more technologically relevant than germanium.

Lastly, in chapter 5, we used fundamental materials science thermodynamics and kinetics to identify a protection layer to prevent the lithiation of anode current collectors made of aluminum. The goal was to replace copper with aluminum as the material for anode current collectors to reduce the overall cost and weight of lithium-ion batteries.

Aluminum readily forms an alloy with lithium in the electrochemical environment of the anode current collector, so it was necessary to engineer a protection layer that prevented the reaction. This protective layer should not react with lithium in that electrochemical environment, block lithium diffusion, be electrically conductive and be made of abundant materials. We reviewed the literature in search of phase diagrams and diffusivity data of conducting materials, and found one material that met all the criteria. This strategy saved time and unnecessary experiments and provided a solid background for experimentation. The material we found from the literature search effectively prevented the lithiation of aluminum for hundreds of hours. Some of the experiments are still running with no sign of failure after hundreds of hours. More work is needed to fully understand the diffusion of lithium through this material, as well as the role of defects in large area current collectors. Similarly, it will be necessary to demonstrate the performance of this protection layer in full cells and in direct contact with lithium metal. The work presented in chapter 5 is a solid foundation for future development of anode current collectors made of aluminum or other electrochemically unstable materials.

This thesis pushes the edge of our knowledge and understanding of electrochemical interfaces a little further in different realms of application in the world of lithium-based batteries.

APPENDIX

Python Code to Calculate Current Density Maps

This code takes contact area maps as inputs and produces current density maps as outputs as described in chapter 3. This version of the code can be used when the potential at the contacts is unknown but the total current is known. The input for this code is a folder with images that represent contact area maps, and the output is a csv file for each scan with the information of location and current density of each pixel. A version of this code that can be run online is available in the link below:

https://colab.research.google.com/drive/1_C2StarSn-IxOMYP6_xPcFp1gZonHrih?usp=sharing

```
import numpy as np #Can be used without GPU, but consumes large amounts
of RAM
import cupy as cp #Necessary when using GPU
import pandas as pd
from PIL import Image
import os

## Physical constants
resizing_factor=5 #Specify the factor by which the images need to be
compressed
applied_current=0.314 #Total applied current in mA
radius=(1.7*1e-4)*resizing_factor/1.77 # Corrects pixel dimensions |
Units must be cm
```

```

area=((1.7*1e-4)*resizing_factor)**2 # Corrects pixel dimensions |
Units must be cm2
rho=500 # Resistivity based on 2e-3 S/cm -> 500 ohm cm

directory = "DIRECTORY PATH"

for file_name in os.listdir(directory):
    ## Import image
    image=Image.open(directory+"/"+file_name)
    # RESIZE image to 1/resizing_factor of original size
    (original=2448,1275)
    image.thumbnail((490,255))
    image3=np.asarray(image)

    ## Find contact spots

spot_list=np.zeros((image3.shape[0]*image3.shape[1],2),dtype='float1
6') #use np to use GPU, np to use CPU
k=0
for i in range(image3.shape[0]):
    for j in range(image3.shape[1]):
        if image3[i][j]>255*0.6: # Threshold: 60 % of max intensity
            (255)
            spot_list[k,0]=i
            spot_list[k,1]=j
            k=k+1
spot_list=spot_list[~np.all(spot_list == 0, axis=1)]

## Calculate coeff matrix

coef_mat=np.zeros((len(spot_list)+1,len(spot_list)+1)) #use np to
use GPU, np to use CPU
k=0
for a in spot_list:
    coef_mat[k,0:-1]=rho/2/3.14/radius/2/(((a[0]-
spot_list[:,0]))**2+((a[1]-spot_list[:,1]))**2)**0.5 # UNITS: (ohm
cm)/(cm)
    k=k+1

```

```

cp.fill_diagonal(coef_mat, rho/4/radius)

# Last column is -1 as the coefficient for the field
coef_mat[:, -1] = -1
# Last row is 1 as the coefficient for each of the currents that
add up to the total current (balance of currents)
coef_mat[-1, :] = 1
# The very last item of the last row is 0 since the balance of
currents does not include a voltage (mV) term
coef_mat[-1, -1] = 0

## Solve
b = cp.zeros(len(spot_list) + 1)
b[-1] = applied_current
currents = cp.linalg.solve(coef_mat, b)
#reset coef_mat
coef_mat = []

## Save DF as csv | last row is a voltage
cur_df = pd.DataFrame(currents)
positions_df = pd.DataFrame(spot_list)

current_dataframe = pd.concat([cur_df, positions_df], ignore_index=True,
                               axis=1)
current_dataframe.columns = ['Current (mA)', 'posY', 'posX']
current_dataframe['spot', 'current', 'density (mA/cm2)'] = current_dataframe['Current (mA)'].apply(lambda
x: x/area)
csv_file = "DESTINATION DIRECTORY" + file_name.replace("png", "csv")
current_dataframe.to_csv(csv_file, index=False)

```

VITA

Francisco Quintero was born in Belalcázar-Páez, Cauca, a rural town in the mountains of the south west of Colombia. There, he received his elementary and secondary education at Institución Educativa Normal Superior de Tierradentro "Enrique Vallejo". After completing his secondary education, he pursued a bachelor's degree in Chemical Engineering at Universidad Nacional de Colombia, in Bogotá. He wrote his undergraduate thesis on the synthesis and use of titania nanotube arrays for wastewater treatment. Following this research, he completed a master's degree in Chemical Engineering at the same university. His master's thesis was focused on the effect of synthesis conditions on the morphology of titania nanotubes and their application in super dielectric capacitors. With a new interest in energy storage, Francisco Quintero obtained a Minciencias-Fulbright scholarship to complete a Ph. D. program at Georgia Tech. During his Ph. D., Francisco Quintero participated in the creation and organization of a number of initiatives to improve the graduate student experience at Georgia Tech including Fulbright Open Talks, CRIDC 2020, and GradChats. Since his first publication in 2015, he has co-authored over a dozen scientific articles and a book chapter.